Hardware-Efficient Quantum Error Correction With Nitrogen-Vacancy Centers

by
Mo Chen
B.S., Fudan University (2012)
S.M., Massachusetts Institute of Technology (2015)

Submitted to the Department of Mechanical Engineering
in partial fulfillment of the requirements for the degree of
Doctor of Philosophy
at the
MASSACHUSETTS INSTITUTE OF TECHNOLOGY
February 2020

Signature redacted

Author .....
Department of Mechanical Engineering
December 15, 2019

Certified by..... Signature redacted .....
Paola Cappellaro
Associate Professor of Nuclear Science and Engineering
Thesis Supervisor

Signature redacted

Certified by.....
Nicholas Xuanlai Fang
Professor of Mechanical Engineering
Signature redacted Chairman, Thesis Committee

Certified by...
Seth Lloyd
Professor of Mechanical Engineering
Signature redacted Thesis Committee

Accepted by .....
Nicolas G. Hadjiconstantinou
Chairman, Department Committee on Graduate Theses

Hardware-Efficient Quantum Error Correction With Nitrogen-Vacancy Centers

by

Mo Chen

Submitted to the Department of Mechanical Engineering
on December 15, 2019, in partial fulfillment of the
requirements for the degree of
Doctor of Philosophy

Abstract

Quantum technologies promise to revolutionize many fields, ranging from precise sensing to fast computation. The success of novel technologies based on quantum effects rests on engineering quantum systems robust to decoherence–the uncontrollable decay of quantum coherence, one of the very features that empowers quantum computation. To date, performance of quantum devices in the noisy intermediate-scale quantum (NISQ) era is still limited by decoherence. The long term solution is universal quantum computers that run on fault-tolerant quantum error corrected logical qubits which are immune to decoherence. However, the substantial overhead of qubits and quantum gates quantum error correction (QEC) imposes is thought to greatly limit its utility in NISQ devices.

In this thesis, we address this challenge through a hardware-efficient approach–leveraging understanding of the quantum system towards more efficient and robust QEC protocols, which opens a potential avenue for useful QEC in near-term, pre-fault-tolerant devices. We are interested in the solid-state quantum register comprising the nitrogen-vacancy (NV) electronic spin and neighboring nitrogen and carbon nuclear spins. First, we developed techniques that provided us with precise knowledge of the system Hamiltonian and in turn high-fidelity and fast control. Next, we investigated and identified the decoherence mechanism of nuclear spins in the quantum register. The dominant noise turns out to be the thermal fluctuation of the NV electron. We demonstrated a dynamical decoupling approach to suppress the fluctuator noise and extended the nuclear spin coherence time. Furthermore, based on the precise knowledge of the system Hamiltonian and decoherence model, we customized a hardware-efficient QEC code for dephasing induced by a common fluctuator. This QEC code requires exponentially less overhead compared to the usual repetition code, and is robust to model imperfections. Finally, we developed experimental building blocks for near-term applications of the hardware-efficient QEC.

Thesis Supervisor: Paola Cappellaro

Title: Associate Professor of Nuclear Science and Engineering

Acknowledgments

My journey towards my Ph.D. at MIT over the past seven years has been exciting, rewarding and challenging. It is not a smooth ride, and would have been more difficult without the support and help of many people. I would like to give my special thanks to all of you!

First and foremost, I am extremely fortunate to have worked with Paola for the past five years. It is such a humbling and rewarding experience. When I first joined the quantum engineering group (QEG), I was a mechanical engineer with experience in microfluidics and 3D printing. Paola not only trusted me and gave me the chance to embrace a whole new research area, but also patiently guided me. She offered me freedom to explore, and allowed me the time to truly understand the underlying laws of physics at my own pace. Paola is committed to caring and very generous to students with her time. When I have confusions in research or life, I can always knock on her door and she will stop her work and talk with me. Last but not least, Paola is very sharp and insightful. She always catches the tiniest ungrounded claims, through which I have grown tremendously.

I am very grateful to Nick. He supervised me for my Master's thesis, and has inspired me with his bold and ambitious ideas, passion for science, and at the same time practical suggestions for the nitty-gritty in experiments. He is a role model being both a physicist and engineer, effectively communicating to both communities and combining the interesting part of both worlds.

I would like to thank Seth for fun, insightful and valuable discussions during the committee meetings. Seth is very down-to-earth, and is a constant inspiration for me with his curiosity and eagerness to learn everything.

Next I would like to thank all the QEG members. In particular, my senpai, Masashi who taught me all the fundamentals of NV experiments and handed me (arguably) the best setup. My fantastic theoretical collaborator David, without whom many of the works here would not be possible. David's self-discipline is also awe-inspiring. My officemates Calvin and Yixiang, with whom I had a lot of interesting

discussions and our friendship goes beyond science. Yixiang is also my snowboarding buddy. I am grateful to former postdocs JC, Kasturi, Luca and Ulf for experimental skills and theoretical concepts they taught me. I would like to thank senior students Alex, Ashok, Ken and Akira, who helped me grow as a quantum engineer, and also bright young minds: Changhao, Pai, Scott, Guoqing, Yuan for their passion and diligence that inspire me. I would also like to thank my hard-working UROP student Genyue Liu, who made the machine learning project possible.

I am sincerely grateful to my friends in CUA both at MIT and Harvard for valuable discussions. I have learned a lot (and borrowed tons of experimental tools) from them (from Nick's lab as well). I would like to thank research staff Kurt from MTL and Mark from Edgerton machine shop for going above and beyond to help, and our efficient and responsive administrative assistant Dianne.

Finally I would like to thank my parents and my wife for their unconditional love and support.

Thank you all!

Contents

List of Figures

THIS PAGE INTENTIONALLY LEFT BLANK

List of Tables

THIS PAGE INTENTIONALLY LEFT BLANK

Chapter 1

Introduction

1.1 Quantum Information and Science

The prosperity of the Information Age is deeply rooted in Moore's law–"the number of transistors doubles every year per integrated circuit" (later modified by Moore himself to every two years) [221]. Gorden Moore initially predicted the trend would go on for another decade. It has now been more than five decades since his initial observation, and the scaling has finally come to stagnation–it is physically impossible to further reduce the size while maintaining the classical properties of transistors [66].

On the other hand, quantum computers, though in their infancy, promise exponential speedup in tasks like factoring large numbers using Shor's algorithm [190, 193, 157]. Unicorns and startups are developing various hardware platforms and chasing after the quantum version of Moore's law–which translates into either increasing the coherence time by 10X every 3 years [222], increasing the computational power over classical ones at a double exponential rate [97], or doubling the "quantum volume" every year [57].

Remarkably, google has recently achieved "quantum supremacy" [166], where noisy, intermediate-scale quantum (NISQ) computers [167] outperform the most powerful classical computer in *some* task(s)–sampling random quantum circuits in this case [14]. Although in its current form, the task is of little practical use, the realization of "quantum supremacy" serves as a milestone and reassurance of the computational

power a universal quantum computer would possess.

It is critical to realize the big gap between NISQ devices and a universal quantum computer. Most notably, the vulnerability to errors on the qubits, which are called decoherence–the unwanted and uncontrollable decay of quantum coherence, one of the very features that empowers quantum computation. Most NISQ devices are limited by decoherence, and could only mitigate part of the effect by open loop control like dynamical decoupling [214]. On the other side of the spectrum, a universal quantum computer is immune to decoherence. It runs on logical qubits, which are redundantly encoded by multiple physical qubits and protected against decoherence by quantum error correction (QEC) [157, 191]. On top of errors on the qubit, there are errors on the quantum control which can influence logical qubits and are not corrected by QEC. These errors could be tackled by applying quantum control in a fault-tolerant way, usually in the form of transversality [192, 157]. Fault-tolerancy requires extra redundancy in addition to those required by QEC, making the overhead prohibitively high for near-term devices. For the purpose of this thesis, I will focus my discussion on QEC for a single logical qubit, and leave fault-tolerance out.

1.2 Error Detection and Correction

1.2.1 Error Correction in the Classical World

Error detection and correction is a very powerful tool not only in quantum computation but also in classical computers. In fact it is arguably one of the major reasons digital computers prevailed over analog computers. The key idea is to add some *redundancy* to the information in such a way that the receiver can check and correct if an error has happened. One pedagogical example is to use a bitstring 000(111) to represent the classical bit 0(1). The receiver can do a majority vote to recover the original bit if at most one bit in the bitstring is corrupted. Before I make a connection to QEC, I will first introduce some basic quantum mechanical notation for convenience.

1.2.2 From Classical to Quantum

The counterpart of a classical bit is a quantum bit, or qubit for short, given by an effective quantum two-level system (TLS). To denote different qubit states we use the 'ket': $|0\rangle$ ($|1\rangle$) for the qubit in 0(1) state. The qubit is famously known for allowing superposition

$$|\psi\rangle = c_0 |0\rangle + c_1 |1\rangle = \cos\frac{\vartheta}{2} |0\rangle + e^{i\varphi} \sin\frac{\vartheta}{2} |1\rangle \tag{1.1}$$

where the parametrization $\{\vartheta, \varphi\}$ allows visualization of a qubit state on the Bloch sphere surface by spherical coordinate $\{\vartheta, \varphi\}$ (Fig. 1-1).

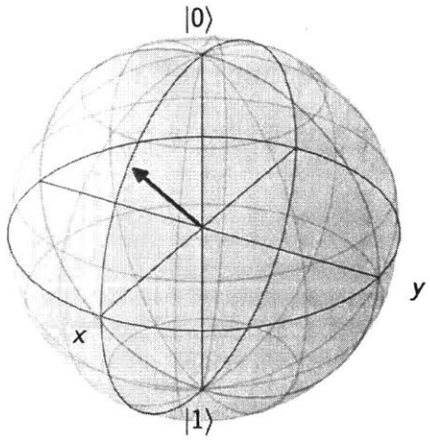

Figure 1-1: Bloch Sphere. The green arrow defined by $(\vartheta = \frac{\pi}{4}, \varphi = 0)$ represents state $\frac{\sqrt{2}}{2} |0\rangle + \frac{\sqrt{2}}{2} |1\rangle$.

We now introduce density operator

$$\rho = \sum_k p_k |\psi\rangle_k \langle\psi| = \frac{1}{2}(\mathbb{1} + r_x\sigma_x + r_y\sigma_y + r_z\sigma_z) \tag{1.2}$$

where the total probabilities of having state $|\psi\rangle_k$ is unity: $\sum_k p_k = 1$. The Bloch vector $\vec{r} = (r_x, r_y, r_z)$ represents the density operator on Bloch sphere. Note that $|\vec{r}| \leq 1$ means the Bloch vector can be either on or *inside* the Bloch sphere. The decay of a quantum state from $|\vec{r}| = 1$ to $|\vec{r}| < 1$ is related to decoherence, an unwanted effect caused by the interaction between physical qubits and their environment. The

ability to measure all the components in $\vec{r}$ in separate experiments and reconstruct the density operator is called quantum state tomography, which gives precise information of the qubit state.

1.2.3 The Need for Quantum Error Correction

Experimentally, all physical systems inevitably interact with their environment, and therefore decohere over time. In turn, the quantum information they carry is lost. Unfortunately, classical error correction schemes do not work in the quantum regime: Firstly, due to superposition (Eq. 1.1), information is stored in the analog form of parameters $\{\vartheta, \varphi\}$. This is incompatible with classical *digital* error correction. Secondly, the no-cloning theorem of quantum mechanics [157] prohibits us from creating an identical copy of an arbitrary unknown state. Finally, measurement collapses the quantum states [157].

In QEC, the key idea is still to use redundancy as in classical error correction, but one will have to detect and correct errors in a digital way. This is achieved by encoding and detecting errors from global properties like parity of the qubit states, which does not contain any quantum information carried by the qubits. The logical states form the eigen-basis of the error syndrome measurement operators, with degenerate eigenvalues. Errors will bring the logical states to the rest of the Hilbert space with different eigenvalues. This way, results of the error syndrome is digitized to within or outside of their $+1$ eigenvalue subspace, and the error syndrome measurements do not reveal any information about the logical qubit state, avoiding collapsing the quantum information. A pedagogical example is the simplest CSS code [191, 199, 200]–repetition code, where the logical states read

$$|\psi\rangle_{\mathrm{L}} = c_0 |0\rangle_{\mathrm{L}} + c_1 |1\rangle_{\mathrm{L}} = c_0 |000\rangle + c_1 |111\rangle . \tag{1.3}$$

A single bit flip error is detected by measuring $S_0 = \sigma_z^1 \sigma_z^2$, $S_1 = \sigma_z^1 \sigma_z^3$, where σ_z^i is the Pauli Z operator on qubit i. The logical states $|000\rangle$ and $|111\rangle$ are both the $+1$ eigenstate of S_0, S_1. The classical bitstring $S_0 S_1$ uniquely tells us if no error

($S_0S_1 = 00$), or a bit flip happened to qubit 1 ($S_0S_1 = 11$), qubit 2 ($S_0S_1 = 10$), or qubit 3 ($S_0S_1 = 01$). An operation based on feedback from S_0S_1 could correct the corresponding error. Error rates could consequently be suppressed to arbitrarily low levels by increasing the QEC frequency (not considering control errors) [191, 199, 200, 193, 157]. QEC is therefore believed to be one of the fundamental building blocks for scalable universal quantum computation [157, 65].

1.3 Quantum Error Correction: Current Status

1.3.1 Challenges in Experiments

Due to the importance of QEC, it has been an active area of research. For example, the repetition code mentioned above has been tested in various physical platforms, including NMR [55, 150], trapped ion [182], superconducting qubit [170], and color centers in diamond [203, 216, 56]. Other CSS codes and surface codes were explroed as well [118, 46, 112]. Unfortunately, in most cases, the overhead in QEC–state preparation, error syndrome measurement, feedback, recovery–makes the logical qubit perform worse than its constituent physical qubits. Therefore, a benchmark called "break-even point" was proposed, remarking logical qubit living as long as the best physical qubit consisting of the logical qubit. At this point, the gain from QEC balances the overhead. Before "break-even", QEC is of no practical use.

Reaching the break-even point proves challenging. As one can see from the simple example of repetition code, the logical state of any superposition is a highly entangled state of many physical qubits. Consequently, the logical qubit is subject to stronger noise and intrinsically decoheres faster. To make it worse, the state preparation, error detection and correction all require multi-qubit control, which are slow and therefore impose a heavy overhead compared to not doing QEC at all.

As an example, for room-temperature Nitrogen-Vacancy (NV) center with ^{13}C in diamond, the realization of repetition code requires 14 quantum gates for one round of state preparation, error correction and readout, among which 10 are nuclear spin

gates. These nuclear spin gates are slow, making the whole process ($\sim$ 1.8ms) on the same order of the coherence time of NV, yielding a total process fidelity of $\sim$ 43%, rejecting break-even [203].

There are two strategies to reach and surpass the break-even point. One is to improve the qubit itself–longer coherence time, higher-fidelity control, faster gates, to surpass the overhead of QEC. Another way is to come up with a more efficient QEC code to lower its overhead. Both methods have been successfully implemented in experiments, which led to break-even [56, 160, 102]. In this thesis, I mainly focus on the second approach, although I have improved the quantum control and qubit coherence as well along the way.

1.3.2 Success in Circuit QED

The possibility of an efficient QEC code has long been explored. Based on knowledge of the noise, efficient QEC codes were proposed that require less resources and are more robust. Examples include references [50, 90, 12, 124, 123, 173, 147]. In particular, bosonic error correction has experimentally reached the break-even point in circuit QED system [160, 102].

In this system, researchers used a transmon coupled to a 3D microwave cavity, where the dominant error is loss of microwave photons in the cavity. The encoding is achieved in the over-complete basis of coherent states of microwave photons, which are the eigenstates of photon loss, making the logical qubit insensitive to the noise. In this case, the large Hilbert space of the harmonic cavity modes provides the necessary redundancy for encoding. In experiment, researchers have shown longer coherence time of the logical qubit than the best physical qubit in the system [160]. A similar code, called the binomial code, has also shown to break-even [102]. Later, researchers have improved the protocol to demonstrate fault-tolerant error detection [177] and two-qubit gates between logical qubits [176, 49, 87].

1.4 Thesis Overview

We want to share the same philosophy underlying the success of hardware-efficient QEC in circuit QED: well-characterize our particular physical system, understand the decoherence mechanism, customize a hardware-efficient QEC code and then implement it in room-temperature NV-diamond system.

The thesis is organized accordingly: the second chapter first introduces the physical system–a quantum register in diamond comprising of an NV electronic spin and neighboring nuclear spins. We then review two categories of nuclear spin control techniques–direct RF control and indirect control using NV as an actuator. Based on these two approaches, we are able to characterize different aspects of our system and obtain precise knowledge of the system Hamiltonian. Part of this chapter was published as ref. [44].

The third chapter studies the dominant decoherence mechanism of nuclear spins. Using the native ^{14}N as an example, we propose a semi-classical model based on knowledge of the system Hamiltonian to quantitatively predict and experimentally verify that ^{14}N decoheres due to the thermal fluctuation of NV electron. This model is general and applies to other neighboring nuclear spins like ^{13}C 's as well. In addition we show that an open loop control on the fluctuator could help mitigate the decoherence effect. This chapter is published as ref. [43].

The fourth chapter proposes a hardware-efficient QEC code tailored for the decoherence model identified in the previous chapter. The QEC code requires exponentially less overhead and is more robust compared to the repetition code. In particular, one logical qubit consists of only two physical qubits, and the recovery operation avoids the expensive nuclear-nuclear spin gate. This hardware-efficient QEC code is therefore promising for experimental implementation. This chapter mainly consists of ref. [123]

In the fifth chapter, we develop all the experimental tools required by the hardware-efficient QEC code. As nuclear spins cannot be directly initialized and read out, we use sequences developed in the second chapter as building blocks to achieve higher-level

controls like nuclear spin state initialization, control and tomography measurement. We further construct quantum circuits out of these building blocks and demonstrate preparations of the logical state basis with high fidelity. The techniques developed here pave the way to implementing the QEC code in the near future.

The sixth chapter discusses remaining challenges and describes next steps to completely realize room-temperature QEC using the hardware-efficient approach, and possible directions beyond room-temperature QEC in diamond.

To enhance the readout fidelity of nuclear spins, we explored combining repetitive readout and machine learning. The results are presented in Appendix. A, published as ref. [131].

Chapter 2

Characterization and Control of Neighboring Nuclear Spins

Precise characterization of a system's Hamiltonian is crucial to its high-fidelity control that would enable many quantum technologies, ranging from hardware-efficient quantum error correction to communication and sensing. In particular, energy non-conserving off-diagonal parts of the Hamiltonian are usually more difficult to characterize, even if they can give rise to subtle but non-negligible effects. In this chapter we present two strategies for high-fidelity control and for the precise estimation of the off-diagonal hyperfine couplings between an electronic and a nuclear spin, focusing on the native ^{14}N and neighboring ^{13}C respectively. For ^{14}N , we apply the direct radiofrequency (RF) control technique to precisely determine the transverse hyperfine coupling between a Nitrogen-Vacancy (NV) center electronic spin and its native ^{14}N [44]. In addition, we show how this transverse hyperfine coupling, that has been often neglected in experiments, is crucial to achieving large enhancements of the nuclear Rabi nutation rate. For ^{13}C , we first apply the indirect control using NV as an actuator to individually address neighboring ^{13}C nuclear spins and precisely determine the $A_\perp$ component of their hyperfine couplings with NV electronic spin [204]. We then implement a direct control technique called DDRF, a modification to the aforementioned direct RF control for weakly coupled nuclear spins including most ^{13}C 's [34]. The combination of the direct and indirect control methods allows us to

individuall access and control all neighboring ^{13}C 's, and identify those suitable for hardware-efficient QEC in our system.

2.1 A Quantum Register Based on Spins in Diamond

Quantum technologies promise to revolutionize many fields, ranging from precision sensing to fast computation. The success of novel technologies based on quantum effects rests on engineering quantum systems robust to noise and decoherence and on controlling them with high precision. Solid-state systems comprising nuclear spins have emerged as promising candidates, since the nuclear spin qubits are only weakly coupled to external fields and thus exhibit long coherence times. The Nitrogen-Vacancy (NV) center [91], among others, is of particular research interest. The NV center is a naturally occurring point defect in diamond [80]. Thanks to its optical properties and long coherence times, it has emerged as a versatile system for quantum sensing [205, 70, 210], quantum information [225, 39] and photonics applications [6, 98].

The nuclear ^{14}N and ^{13}C spins often play important roles in these applications. Not only can they serve as qubits in small quantum algorithms [82, 215, 88, 216, 203], but they can also be used to enhance the readout fidelity of the NV electronic spin [156, 142, 74, 130] and achieve more sensitive detection of magnetic fields [114, 13, 16] and rotations [125, 9, 107]. The system consisting of one NV electronic spin, the native Nitrogen nuclear spin, and neighboring ^{13}C nuclear spins is often referred to as a quantum register.

In order for nuclear spins to be used as good qubits, there are two important requirements: their Hamiltonians need to be known with very high precision, as this would enable applying e.g. optimal control methods [115, 181], and high-fidelity individual nuclear spin addressing and control should be available, in order to perform quantum information processing. In the following sections, we focus on ^{14}N and ^{13}C respectively, and show how to meet these two requirements.

2.2 Characterization and Control of Nitrogen

The Nitrogen nuclear spin is native to NV center (without loss of generality, we will focus our discussion to ^{14}N), and the diagonal part of the NV-^{14}N Hamiltonian has been well-characterized before [201, 196, 195, 73, 189, 105, 168, 204]. The transverse hyperfine coupling is more difficult to measure [113] and published values do not match well [69, 79, 99]. The most precise characterization to date has been achieved by ensemble ESR techniques [79]. In that work, the ESR spectrum of an ensemble of NV centers was measured by induction methods while applying a magnetic field along the $\langle 110 \rangle$ direction to amplify nominally forbidden transitions. This method is not applicable to single NV centers, since the strong transverse field would quench the spin-dependent optical contrast.

Here we propose a different strategy based on second-order effects due to mixing of the electronic and nuclear spin states [5] in order to identify their coupling strength and to enhance the nuclear spin nutation rate [178], that can be carried out with optically detected magnetic resonance. Thanks to this method we can determine the value of the transverse coupling with a better precision than achieved previously. The method is not restricted to the NV spin system, but could be applied more generally to other electronic-nuclear spin systems, such as phosphorus [149] or antimony [224] donors in silicon, defects in silicon carbide [220, 78] or quantum dots [42]. Precise knowledge of the hyperfine interaction tensor would enable achieving more precise control, elucidating modulations of the NV echo dynamics or, as we show here, achieving faster Rabi nutation of the nuclear spin [44].

2.2.1 Direct RF Control of Nitrogen

Theoretical Model

The NV ground state is a two-spin system given by the electronic spin of the NV center ($S = 1$) and the nuclear spin ($I = 1$) of the substitutional ^{14}N adjacent to the vacancy that comprise the defect. In the experiments, we are only interested in two of the nuclear spin levels ($m_I = +1, 0$) that we drive on-resonance, while the third level

can be neglected. Then, the Hamiltonian of the reduced system (see Appendix. B) is given by $\mathcal{H} = \mathcal{H}_{\|} + \mathcal{H}_{\perp}$, where the secular, $\mathcal{H}_{\|}$, and nonsecular, $\mathcal{H}_{\perp}$, terms are:

$$\begin{aligned} \mathcal{H}_{\|} &= \Delta S_z^2 + (\gamma_e B_z + \frac{A_{\|}}{2}) S_z + (Q + \gamma_n B_z) I_z + A_{\|} S_z I_z, \\ \mathcal{H}_{\perp} &= \sqrt{2} A_{\perp} (S_x I_x + S_y I_y). \end{aligned} \tag{2.1}$$

Here S and I are the electron spin-1 and nuclear spin-1/2 operator respectively. $\Delta = 2.87$ GHz is the zero-field splitting and $Q = -4.945$ MHz [196] the nuclear quadrupolar interaction. The NV spin is coupled to the nuclear spin by a hyperfine interaction with a longitudinal component $A_{\|} = -2.162$ MHz [196] and a transverse component $A_{\perp}$ which we want to estimate. A magnetic field B_z is applied along the NV crystal axis [111] to lift the degeneracy of the $m_s = \pm 1$ level, yielding the electron and nuclear Zeeman frequencies $\gamma_e B_z$ and $\gamma_n B_z$ where $\gamma_e = 2.8$ MHz/G and $\gamma_n = -0.308$ kHz/G.

Let $|m_s, m_I\rangle$ be eigenstates of $\mathcal{H}_{\|}$. The transverse coupling $A_{\perp}$ mixes states connected via zero-quantum (ZQ) transitions, $|+1, 0\rangle \leftrightarrow |0, 1\rangle$ and $|0, 0\rangle \leftrightarrow |\text{-}1, 1\rangle$. Diagonalization of the total Hamiltonian can then be achieved by rotating the two ZQ subspaces with a unitary transformation $U_{\text{ZQ}} = e^{-i(\sigma_y^- \vartheta^- + \sigma_y^+ \vartheta^+)}$, where we defined $\sigma_y^+ = i(|+1, 0\rangle\langle 0, 1| - |0, 1\rangle\langle +1, 0|)$; $\sigma_y^- = i(|0, 0\rangle\langle \text{-}1, 1| - |\text{-}1, 1\rangle\langle 0, 0|)$ and the rotation angles are

$$\begin{aligned} \tan(2\vartheta^+) &= \frac{2A_{\perp}}{\Delta + \gamma_e B_z - \gamma_n B_z - Q}, \\ \tan(2\vartheta^-) &= \frac{-2A_{\perp}}{\Delta - \gamma_e B_z - A_{\|} + \gamma_n B_z + Q}. \end{aligned} \tag{2.2}$$

Because of this level mixing, a field on resonance with the nuclear spin transition also drives electronic transitions. Although the electronic spin state is unchanged to first order, as long as the mixing is small, the nominally forbidden transitions result in an enhancement of the nuclear state nutation frequency, as we explain below.

When applying a radio frequency (RF) field to drive the nuclear spin, the inter-

action Hamiltonian of the NV-^{14}N system with the RF field is:

$$\mathcal{H}_{\mathrm{rf}}(t) = 2B_1 \cos(\omega t)(\gamma_e S_x + \sqrt{2}\gamma_n I_x), \tag{2.3}$$

where B_1 is the RF field strength. The Hamiltonian can be simplified by going into a rotating picture at the RF frequency ω and applying the rotating wave approximation (RWA), to obtain $\mathcal{H}_{\mathrm{rf}} = B_1(\gamma_e S_x + \sqrt{2}\gamma_n I_x)$. We note that since we might have $\gamma_e B_1 \gg \omega$, effects from the counter-rotating fields, such as Bloch-Siegert shifts of the electronic energies, might be present. These effects were however negligible at the fields and Rabi strengths used in the experiments (see Appendix. B). Transforming $\mathcal{H}_{\mathrm{rf}}$ with the unitary U_{ZQ} and denoting states and operators in the new frame by a hat, we obtain $\hat{\mathcal{H}}_{\mathrm{rf}} = U_{\mathrm{ZQ}}\mathcal{H}_{\mathrm{rf}}(t)U_{\mathrm{ZQ}}^{\dagger} = \mathcal{H}_n + \mathcal{H}_e$, with

$$\mathcal{H}_n = \sqrt{2}\gamma_n B_1 \left(\alpha_1 |\hat{1}\rangle\langle\hat{1}|_e + \alpha_0 |\hat{0}\rangle\langle\hat{0}|_e + \alpha_{-1} |\hat{-1}\rangle\langle\hat{-1}|_e\right) \hat{I}_x \tag{2.4}$$

Here α_{m_s} denote the enhancement factors in each manifold of the NV spin:

$$\alpha_{+1} \approx 1 + \frac{\gamma_e}{\gamma_n}\frac{A_\perp}{\Delta + \gamma_e B_z - \gamma_n B_z - Q}, \tag{2.5}$$

$$\alpha_0 \approx 1 - \frac{\gamma_e}{\gamma_n}\left(\frac{A_\perp}{\Delta + \gamma_e B_z - \gamma_n B_z - Q} + \frac{A_\perp}{\Delta - \gamma_e B_z - A_\parallel + \gamma_n B_z + Q}\right), \tag{2.6}$$

$$\alpha_{-1} \approx 1 + \frac{\gamma_e}{\gamma_n}\frac{A_\perp}{\Delta - \gamma_e B_z - A_\parallel + \gamma_n B_z + Q}, \tag{2.7}$$

where we show expressions exact up to the first order in $\vartheta^{\pm}$ (see Appendix. B for the exact expressions). The Hamiltonian $\mathcal{H}_e$ can be neglected since electronic spin transitions are far off-resonance.

Thanks to the strong dependence of the enhancement factors on the transverse hyperfine coupling, we can determine $A_\perp$ with high precision from measurement of the ^{14}N Rabi oscillations.

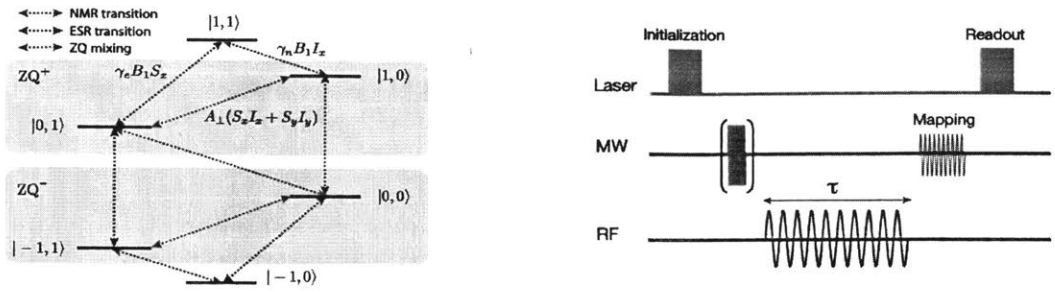

Figure 2-1: Left: energy levels of the reduced NV-^{14}N spin system, showing the transitions that are mixed by the transverse hyperfine coupling. Right: Experimental sequence used to measure the nuclear ^{14}N Rabi frequency in the three NV manifolds.

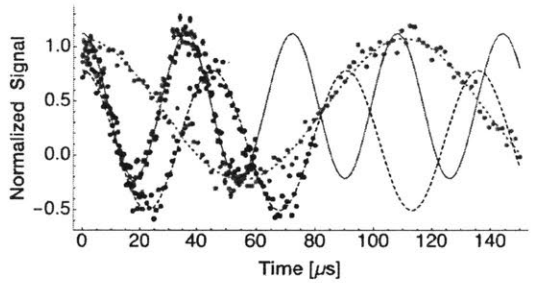

Figure 2-2: ^{14}N Rabi oscillations at $B = 450$G, $B_1 \approx 3.3$G in the three NV manifold (Red, solid line $m_s = 0$. Black, dashed line, $m_s = -1$. Gray, dotted line $m_s = +1$). Here the dots are the experimental results, while the lines are fits to cosine oscillations. The different baseline of the $m_s = -1$ curve is due to small differences in the fluorescence emission of different nuclear manifolds [106].

Experiments

We used a home-built confocal microscope to measure the transverse hyperfine interaction of a single NV center in an electronic grade diamond sample (Element 6, ^{14}N concentration $n_N < 5$ ppb, natural abundance of ^{13}C). The NV center is chosen to be free from close-by ^{13}C . We worked at magnetic fields (300-500G) close to the excited state level anti-crossing so that during optical illumination at 532nm, polarization of the NV spin can be transferred to the nuclear spin by their strong hyperfine coupling in the excited state [106]. As a result, a $1\mu s$ laser excitation polarizes the NV-^{14}N system into the $|0,1\rangle$ state.

Then, the NV spin is prepared in the desired Zeeman state by a strong microwave (MW) pulse ($t_p \approx 50$ns) before coherently driving the nuclear spin by an RF field on resonance with the nuclear transition $|m_s,1\rangle \leftrightarrow |m_s,0\rangle$, for a duration τ (see

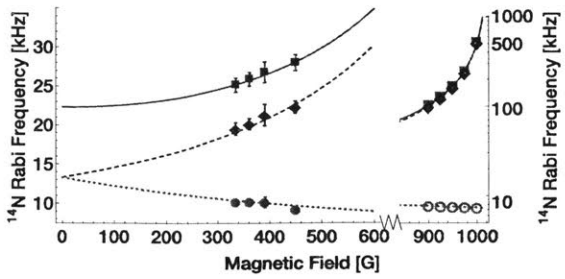

Figure 2-3: ^{14}N Rabi Frequency in the three NV manifold (Red, solid line $m_s = 0$. Black, dashed line, $m_s = -1$. Gray, dotted line $m_s = +1$) as a function of the magnetic field. Rabi frequency corresponds to $\frac{\gamma_n B_1}{2\pi}\alpha_{m_s}$. The filled symbols correspond to the experimental data, which matches closely the theoretical prediction. The effective Rabi frequencies increase rapidly with the field, exceeding 1 MHz when close to ground state level anti-crossing. The enhancement allows fast manipulation of the nuclear spin even when the bare Rabi field is only $B_1 \approx 3.3$G. The theoretical prediction is confirmed by simulations (open symbols) of the spin dynamics.

Fig. 2-1). Finally, the nuclear spin state is detected by employing a MW selective pulse ($t_p \approx 700$ ns) that maps the nuclear spin state onto the NV spin, which in turn can be read out optically due to spin-dependent fluorescence emission intensity. The nuclear Rabi oscillations in Fig. (2-2) clearly show that for a fixed driving strength, the effective Rabi frequency is quite different in the three electronic spin manifolds.

2.2.2 Measuring Transverse Hyperfine by Forbidden Transition

To confirm the expected dependence of the Rabi enhancement factors on the external magnetic field and the NV state, we measured the Rabi oscillations at the three electronic spin manifolds with varying magnetic field B_z. As shown in Fig. (2-3), the measured Rabi frequencies match well with the theoretical model. It is worth noting that contrary to the static pseudo-nuclear Zeeman effect [5], there is a large enhancement ($\alpha_0 \sim 16$, $\alpha_{\pm 1} \approx -9$) even at zero field. Also, close to the ground state avoided crossing ($B \approx 0.1$ T) the enhancement can become very large, exceeding 100. The validity of our approximation in this regime can be confirmed by numerical simulations (see Appendix. B).

While these experiments could be used to extract $A_\perp$, this is not a practical

method to obtain a good enough estimate. The range of magnetic field is restricted by the need to be close to the excited state level anti-crossing, to achieve a good polarization of the nuclear spin. The number of acquired points is limited by the time it takes to change and properly align the external magnetic field. In addition, there might be variations in the bare Rabi frequency in the three manifolds, because of different responses of the electronics used to drive the nuclear spins at the different frequencies.

In order to avoid these difficulties, we fixed the magnetic field to 509G and instead linearly swept the amplitude of the RF driving (B_1). With this procedure, we do not need an independent measure of the bare Rabi frequency in order to extract the transverse hyperfine coupling strength. The relative RF amplitudes B_1 obtained when varying the driving strength can be measured at each nuclear resonance frequency by monitoring the RF voltage with an oscilloscope, confirming its linear dependence with applied power.

We thus measure the effective nuclear Rabi frequency as a function of the normalized RF amplitude $B_1/|B_{1,max}|$ in all three electronic manifolds (Fig. 2-4). The measured Rabi frequency Ω_m is related to its on-resonance value by $\Omega_m = \sqrt{\Omega^2 + \delta^2}$, where δ is the detuning from the nuclear spin resonance frequency. We incorporate this unknown, small detuning in our model and fit the experimental data with the Rabi enhancement formulas (2.5-2.7). From the fit, we obtain an estimate of the transverse hyperfine coupling, $A_\perp = -2.62 \pm 0.05$ MHz, in good agreement with recently published values and with better precision than previously measured.

In order to achieve even better precision, we need to consider all the sources of uncertainty and errors. We find that small errors from imperfect MW π pulses and nuclear polarization only contribute to a reduced fluorescent contrast, but do not affect the estimate of the Rabi frequency under our experimental condition. The detuning of the selective MW and RF pulses from resonance and uncertainty in $A_\parallel$ contributes only linearly to the uncertainty. All these minor errors and uncertainties affect very little the final uncertainty in the estimate of $A_\perp$ (see Appendix. B). The major source of error arises instead from the uncertainty in the measured Rabi frequency, which is

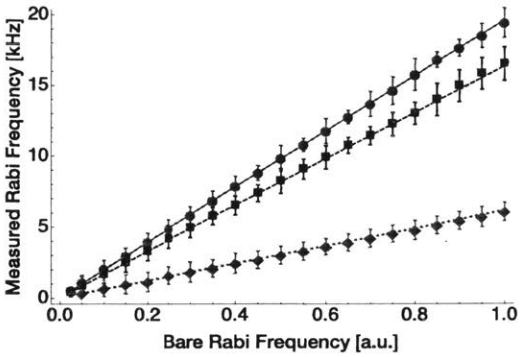

Figure 2-4: Measured enhanced ^{14}N Rabi Frequency in the three NV manifold (Red, solid line $m_s = 0$. Black, dashed line, $m_s = -1$. Gray, dotted line $m_s = +1$) as a function of the bare Rabi frequency at $B = 509$G.

limited by photon shot noise of the optical readout process. Therefore, the precision of the estimate could be improved with more averaging, at the expense of longer measurement time. Currently our total measurement time is limited by the stability of experimental setup, yielding $\delta A_\perp \sim 50$ kHz. Improving the stability of the setup by reducing thermal fluctuations and noise in the driving field (also using decoupling schemes [37, 8]) or employing small ensembles or more efficient optical readout methods such as solid-immersion lenses [141] and charge-state sensing [187] could provide higher precision. Then, the limit would come from uncertainties in γ_e and γ_n, with relative error of 10^{-4} [69, 155], yielding an uncertainty in $A_\perp$ of a few hundred Hz (see Appendix. B).

2.2.3 Discussion

In summary, we observed enhanced nuclear Rabi oscillation in the NV-^{14}N system due to level mixing between electronic and nuclear spin states. We harness the strong dependence of this enhancement on the transverse hyperfine coupling to determine its value with higher precision than previously published results. Theoretical analysis predicts an enhancement factor of almost 3 orders of magnitude when the magnetic field is close to the ground state level anti-crossing, promising fast manipulation of nuclear spin qubit at $\sim$ MHz rates, with only moderate driving strengths. More broadly, the method presented here can be applied to many other electron-nuclear

hybrid spin systems to similarly characterize their interaction Hamiltonian with high precisions. Our results indicate that taking into account non-secular parts of a system's Hamiltonian is crucial to achieving faster and more accurate control of the quantum system.

We remark that although the direct RF control of ^{14}N shown here is powerful in determining the transverse hyperfine interaction strength $A_\perp$, it relies on the optical polarization of ^{14}N for measurement, and NV stays in its eigenstate during the nuclear spin manipulation. For practical quantum information applications, it is convenient if the effect is observable without nuclear spin polarization, and it is mandatory NV stays in arbitrary (coherent) state during the nuclear spin operation. We will show in Sec. 2.3.2 an extension of this direct RF control technique called DDRF, which addresses both of these issues.

2.3 Characterization and Control of Carbon

Although the native ^{14}N nuclear spin is well understood and convenient to control, neighboring ^{13}C 's play an even more important role for scalability. The 1.1% natural abundance of ^{13}C ($I = 1/2$) guarantees each NV is surrounded by roughly $\sim$ 12 ^{13}C nuclear spins of hyperfine $A_\parallel > 20$kHz (Appendix. D), making the quantum register a good fully-connected quantum node [34]. Since the quantum register occurs naturally in the diamond substrate, our main focus is to control it with high fidelity.

Unfortunately, it is not straightforward to control the ^{13}C nuclear spins. For one thing, it does not have convenient polarization and readout at the single qubit level. For another, most ^{13}C 's are far from the NV, coupling to the NV through the magnetic dipole-dipole interaciton. This interaction falls off rapidly as r^{-3}, yielding an average coupling strength < 100 kHz. As a result, unlike the ^{14}N whose hyperfine splitting is strong compared to the coherence time of NV ($A_\parallel > 1/T_2^{*e}$), individual addressing of ^{13}C has an extra requirement–protecting the coherence of NV electron. In other words, dynamical decoupling (DD) of the NV should be built into the control of weakly coupled ^{13}C . This way, we will have access to all the $\sim$ 12 ^{13}C as long as

they satisfy $1/T_2^e < A_\parallel (\sim< 1/T_2^{*e})$.

Based on DD, we will describe two approaches to selectively control individual ^{13}C nuclear spin while maintaining the coherence of NV in arbitrary state. The first one uses NV electron as an actuator to indirectly control the nuclear spin. The control rests on intrinsic hyperfine interaction between NV-^{13}C , and is in turn sensitive in estimating the hyperfine coupling strength including the off-diagonal term, providing precise information of the system Hamiltonian. The second method applies RF pulses to directly control the nuclear spin. This method does not rely on the hyperfine coupling, therefore grants access to more ^{13}C 's in the quantum register, including those suitable for implementing our hardware-efficient QEC protocol.

2.3.1 Indirect Control and Characterization

We start with the first method which uses NV electron as an actuator to indirectly control the nuclear spins. It was first introduced in NV registers by Taminiau et al. in 2012 [204] and extended later by the same group in 2014 [203]. In this method, they simply applied Carr-Purcell-Meiboom-Gill (CPMG) type of DD [40] on the NV. By carefully choosing the interpulse delay, the DD sequence could selectively control individual ^{13}C via its intrinsic hyperfine interaction with NV, while decoupling NV from the rest of the spin bath. Based on this indirect control technique, we could extract the S_zI_z and S_zI_x hyperfine coupling strengths.

Theoretical Model

Here we introduce an intuitive model proposed by Yixiang Liu to describe the indirect control by CPMG (Fig. 2-5). For simplicity, we assume the magnetic field is aligned along the NV [111] axis, and we neglect ^{14}N related Hamiltonian. Due to the large electronic energy scale, we take the secular approximation and keep only terms commuting with S_z. After these simplifications, the Hamiltonian in the interaction picture between NV-^{13}C reads:

$$\mathcal{H} = \omega_L I_z + A_\parallel S_z I_z + A_\perp S_z I_x, \tag{2.8}$$

where ω_L is the nuclear Larmor frequency, $A_\parallel(A_\perp)$ are the transverse and perpendicular hyperfine interaction strength for components $S_zI_z(S_zI_x)$, respectively. Note that $A_\perp$ here is for ZX term, and not to be confused with that for the XX, YY terms used in the previous section for ^{14}N . The effect of XX, YY couplings is second-order and is neglected here.

Focusing on the nuclear spin, we obtain the following Hamiltonian:

$$\mathcal{H}_n = (\omega_L + A_\parallel \lambda(t))I_z + A_\perp \lambda(t) I_x \approx (\omega_L + \frac{A_\parallel}{2})I_z + A_\perp \lambda(t) I_x. \tag{2.9}$$

The last approximation assumes $\lambda(t)$ is balanced and toggles much faster than $A_\parallel$. $\lambda(t)$ depends on the NV state:

$$\lambda(t) = \begin{cases} 0, & \text{NV in } |m_s = 0\rangle \\ \pm 1, & \text{NV in } |m_s = \pm 1\rangle \end{cases}. \tag{2.10}$$

Without loss of generality, we assume NV is toggled back and forth under CPMG sequence between $|0\rangle$ and $|+1\rangle$ from now on. Then $\lambda(t)$ takes the form of a square wave, and its Fourier transform is:

$$\lambda_\pm(t) = \frac{1}{2} \pm \frac{2}{\pi} \sum_{k=1}^{\infty} \frac{(-1)^{k+1}}{2k-1} \cos(\frac{2\pi(2k-1)}{4\tau} t), \tag{2.11}$$

where 2τ is the interpulse delay in CPMG (Fig. 2-5). $\lambda_\pm$ denotes the nuclear spin evolution conditional on NV starting in $|+1\rangle$ or $|0\rangle$. Plugging Eq. 2.11 into Eq. 2.9, it is obvious that CPMG drives a generalized Rabi nutation of the nuclear spin at frequency $\omega = \pi(2k-1)/2\tau$, with amplitude $\frac{(-1)^{k+1}A_\perp}{(2k-1)\pi}$:

$$\mathcal{H}_n \approx (\omega_L + \frac{A_\parallel}{2})I_z \pm \frac{2}{\pi} \cdot (\cos\omega_0 t + \frac{1}{3}\cos 3\omega_0 t + \frac{1}{5}\cos 5\omega_0 t \ldots)I_x, \tag{2.12}$$

where $\omega_0 = \pi/2\tau$.

We see immediately, for $(2k-1)\omega_0 = \omega_L + A_\parallel/2$, or

$$\tau = \frac{(2k-1)\pi}{2\omega_L + A_\parallel} \tag{2.13}$$

the k^{th} order will resonantly drive the nuclear Rabi nutation, with a Rabi frequency of

$$\omega_{\text{rabi}} = \frac{A_\perp}{(2k-1)\pi} \tag{2.14}$$

along the $x(-x)$ axis if NV starts in $|+1\rangle$ ($|0\rangle$). Therefore, the equivalent operator of CPMG control when τ is on resonance (Eq. 2.13) can be written in a compact form

$$\mathrm{CR}_x(\vartheta) = |0\rangle\langle 0|\,\mathrm{R}_{-x}(\vartheta) + |1\rangle\langle 1|\,\mathrm{R}_x(\vartheta), \tag{2.15}$$

where $R_\varphi(\vartheta)$ means a rotation of angle ϑ along axis φ.

One advantage of this conditional rotation (CR) is that by adding a MW $\frac{\pi}{2}$ pulse on NV both at the beginning and end of the sequence, we can observe successful addressing of ^{13}C even when the nuclear spin is in a thermally mixed state. It is a convenient feature in experiment.

To see this effect, we explicitly analyze two conditions: $\vartheta = \{\frac{\pi}{2}, \pi\}$. The NV is first prepared in $\frac{1}{\sqrt{2}}(|0\rangle + |1\rangle)$ before subject to $\mathrm{CR}_x(\vartheta)$ and finally rotated back by a MW $\frac{\pi}{2}$ pulse followed by optical readout. In the former case $\mathrm{CR}_x(\frac{\pi}{2})\left|m_s = +, m_I = \pm\frac{1}{2}\right\rangle = \frac{1}{\sqrt{2}}(|0, \mp y\rangle + |1, \pm y\rangle)$ entangles the NV electron and selected individual ^{13}C nuclear spin. The final measurement of the subsystem (NV) of a bipartite entangled state yields loss of coherence and a mixed state of NV electron. In the latter case $\mathrm{CR}_x(\pi)\left|m_s = +, \pm\frac{1}{2}\right\rangle = \left|-, \pm\frac{1}{2}\right\rangle$, resulting in a separable state between NV and ^{13}C , and inducing a π phase shift to the NV, which is subsequently readout by the last $\frac{\pi}{2}$ pulse. Both cases yield a darker final state ($\rho = \frac{1}{2}\mathbb{1}$ or $|1\rangle$). In fact, as long as τ is on resonance with a ^{13}C , any $0 < \vartheta < 2\pi$ results in a darker final state. It is a convenient feature in identifying individual ^{13}C 's without the need to polarize them or fine-tune ϑ (Fig. 2-6).

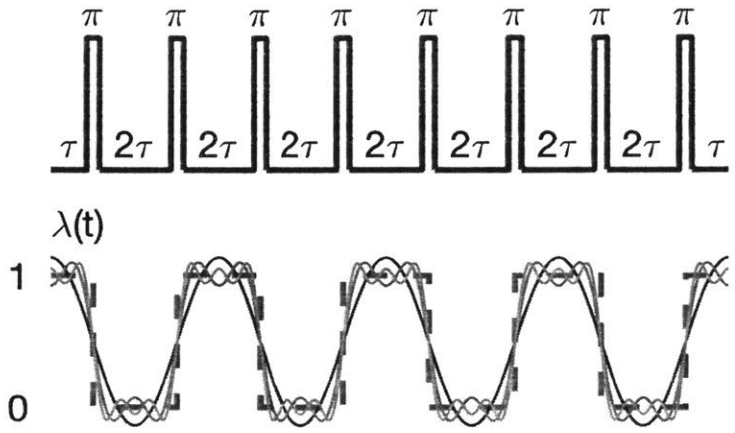

Figure 2-5: Top: Illustration of a CPMG-8 sequence. The unit block $(-\tau - \pi - \tau)$ is repeated 8 times. Bottom: $\lambda(t)$ (gray) and the Fourier decomposition up to the 1st, 2nd and 3rd orders.

Experiment

The experimental setup is the same as described in Sec. 2.2.1. For results shown in this section, we work under a magnetic field of 405 G where the 532 nm laser polarizes both the NV and the ^{14}N to $|0,1\rangle$ state.

To demonstrate our ability to selectively address and control individual nuclear spins, the NV is first prepared in the superposition state $\frac{1}{\sqrt{2}}(|0\rangle + |1\rangle)$ by an on-resonant MW $\frac{\pi}{2}$ pulse. We then apply CPMG sequence of the form $(-\tau - \pi - \tau -)^N$ on the NV. Each block consists of two free precession periods of duration τ, separated by a MW π pulse. The whole block is repeated N times (N is also the total number of π pulses), and constitutes the conditional rotation (CR) gate. Finally, another $\frac{\pi}{2}$ pulse brings the NV state back to its eigen-basis and subsequently read out. In the first experiment, we probe the environment of the NV and identify nearby ^{13}C 's. We fixed the number of pulses to $N = 32$ and swept τ, as shown in Fig. 2-6. The dips in the spectrum indicate successful two-qubit operations between NV and ^{13}C (CR gate, Eq. 2.15).

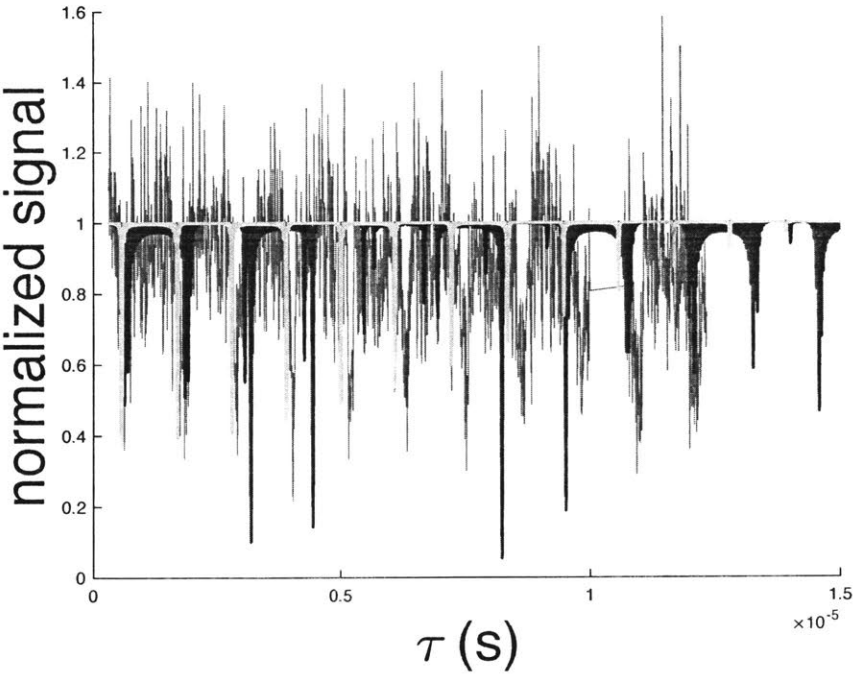

Figure 2-6: CPMG spectrum of one NV at 405 G. The red, blue and green curves are fit to three ^{13}C 's, whose hyperfine strengths are listed in Table. 2.1.

Once we identified the resonance conditions for individual ^{13}C 's from the spectrum, we moved on to demonstrate our ability to control the nuclear spins. The same sequence was used, with τ fixed at the dip positions, and N swept. This results in nuclear Rabi nutations, as shown in Fig. 2-7.

Characterizing $A_{\parallel}$ and $A_{\perp}$ Hyperfine Components

From a CPMG spectrum scan as shown in Fig. 2-6, one can identify a family of dips belonging to the same ^{13}C corresponding to higher harmonics of the effective driving. Following Eq. 2.13, a linear fit to the position of these dips gives an initial estimate of $A_{\parallel}$ (Fig. 2-7). In addition, we gain the knowledge of the corresponding harmonic order k for each dip from the fitting.

We then extract $A_{\perp}$ from the nuclear Rabi oscillation as shown in Fig. 2-7. According to Eq. 2.14, we can estimate $A_{\perp}$ from the nuclear Rabi frequency.

So far we have obtained an estimate for the hyperfine coupling components $A_{\parallel}$, $A_{\perp}$ separately. The precision is less than ideal due to various approximations we have made that lead to the simple form of Eq. 2.13, 2.14. To better characterize the hyperfine components, we numerically fit to the system evolution under Hamiltonian

$$\mathcal{U}(N,\tau) = \Big(\exp[-i\mathcal{H}\tau]\ (\mathrm{R}_x(\pi)\otimes \mathbb{1})\ \exp[-i\mathcal{H}\tau] \Big)^N \tag{2.16}$$

using all the data available to avoid inaccuracies introduced by the approximations. This includes both the CPMG spectrum and the nuclear Rabi nutations relavent to the ^{13}C of interest. Such fits are shown as solid colored curves in Fig. 2-6, 2-7. The fitted values for the three ^{13}C 's are listed in Table. 2.1.

^{13}C	$A_{\parallel}$	$A_{\perp}$
1	-85.6(4)	59.8(5)
2	-43(5)	19.4(4)
3	30(4)	26(1)

Table 2.1: Fit of the hyperfine interaction strengths of the three ^{13}C 's as shown in Fig. 2-6.

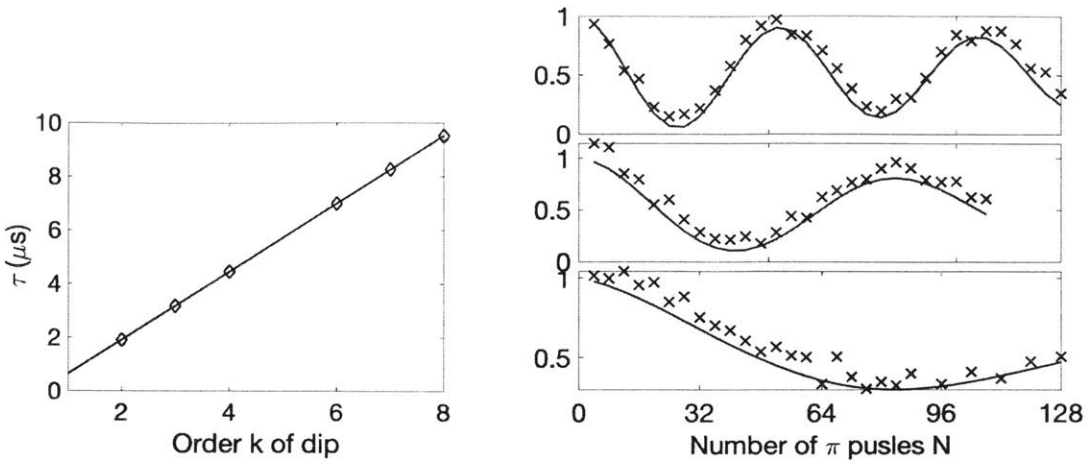

Figure 2-7: Left: Dip positions of different orders k. The linear fit according to Eq. 2.13 gives an estimate of $A_{\|}$. Right: Keep τ fixed, changing the number of π pulses in CPMG is equivalent to driving a Rabi nutation. From top to bottom: $\tau = 3.173\ \mu s, 4.438\ \mu s, 6.697\ \mu s$, corresponding to $k = 3, 4, 6$ th order.

Discussion

In summary, the CPMG method provides a convenient way to decouple NV from all spins in the environment but a particular ^{13}C on resonance. It achieves both protection of the NV from the rest of the spin bath and control of ^{13}C using a simple CPMG sequence. Moreover, it allows observation of successful individual nuclear spin addressing through NV, without the need to polarize ^{13}C or fine-tune control parameters like the number of pulses. This is a big experimental advantage to quickly and thoroughly probe the unknown ^{13}C environment neighboring an NV.

The nuclear spin control by CPMG is not limited to the CR gate discussed above. A more detailed discussion can be found in [203]. In short, for $\tau = \frac{(2k-1)\pi}{2\omega_L + A_{\|}}$, the nuclear spin conditionally rotates along $\pm x$ axes as controlled by NV; for $\tau = \frac{2k\pi}{2\omega_L + A_{\|}}$, the nuclear spin unconditionally oscillates around x axis independent of the NV state; for other τ, the nuclear spin undergoes a rotation along the z axis. Therefore, by appropriate choice of τ and total pulse number N, one can realize universal control of ^{13}C by this indirect control technique [203].

However, as one might have noticed, there are a few potential drawbacks in this method: firstly, it heavily relies on the intrinsic $A_{\perp}$ to drive the nuclear spin, limiting our choices of ^{13}C 's. In particular, all ^{13}C 's aligned close to the NV direction or

^{13}C 's distant from the NV have small $A_\perp$ terms in their hyperfine interaction matrix, preventing efficient control by CPMG. Secondly, the number of pulses required to achieve any operation scales linearly with ω_L, in other words with the magnetic field. Therefore, as the magnetic field increases, pulse errors start to dominate, preventing high-fidelity nuclear spin control at high field. This can be seen from a combination of Eq. 2.13, 2.14: as the field increases, the Rabi frequency remains unchanged, but the interpulse interval τ goes down inversely proportional to ω_L, resulting in the total number of pulses proportional to ω_L. Last but not least, at high field, τ is generally small, posing a challenge to the hardware time resolution (typically 1 ns) [10, 232].

As we will see later in Chapter 5, faithful realization of our decoherence model requires minimizing effects from $A_\perp$. Therefore we introduce another nuclear spin control method in the following section, which is independent of $A_\perp$. The CPMG method introduced here is still useful, as it conveniently and accurately characterizes the Hamiltonian of weakly-coupled ^{13}C .

2.3.2 Direct Control via DDRF

Similar to the direct control of ^{14}N , RF could also drive the ^{13}C 's given their unique hyperfine coupling strength (therefore unique RF frequency). However, unlike the previous case with ^{14}N , most ^{13}C nuclear spins remain unpolarized under laser illumination. In addition, the hyperfine coupling of ^{13}C is generally weak, resulting in very different timescales of the dynamics of NV electron and ^{13}C nuclear spins. It is critical the coherence of NV is protected during manipulation of the nuclear spin.

On the other hand, the CR gate achieved by the indirect control technique discussed above allows convenient readout signal for successfully addressing individual nuclear spins even when they are unpolarized. Besides, the NV electronic spin is protected from the spin bath by DD built intrinsic to the gate.

To this end, a technique combining both the DD on NV and direct RF drive on the nuclear spin is highly needed. Early works are restricted to strongly-coupled nuclear spins [39, 198, 211, 101], and more recently a sequence called "DDRF" was introduced by Bradley et al. [34], circumventing previous restricitons and allowing

control for weakly-coupled nuclear spins. We will briefly review the working principles of DDRF next. Modifications are then introduced to the original sequence to sidestep a technical challenge and realize faster control in experiment. Finally we show how the combination of direct DDRF control and the indirect control approach enables us to identify ^{13}C 's with small $A_\perp$ terms, and DDRF grants us access to these ^{13}C 's that are suitable for hardware-efficient QEC experiments.

DDRF Sequence: Theory

The Hamiltonian between NV-^{13}C is the same as Eq. 2.8:

$$\mathcal{H} = \omega_L I_z + A_\parallel S_z I_z + A_\perp S_z I_x. \tag{2.17}$$

A direct RF field at frequency $\omega_1 = \sqrt{(\omega_L \pm A_\parallel)^2 + A_\perp^2}$ selectively addresses a specific ^{13}C when the electron is in $|m_s = \pm 1\rangle$ state. Without loss of generality, we consider the effective spin-1/2 subspace of NV spanned by $|m_s = 0, +1\rangle$, and ignore $A_\perp$ [1]. The corresponding nuclear spin Hamiltonian conditional on NV in state $|0\rangle$ ($|+1\rangle$) in the rotating frame of RF field takes the form

$$\begin{aligned} \mathcal{H}_0 &= -(A_\parallel + \delta) I_z + \Omega(\cos\varphi I_x + \sin\varphi I_y), \\ \mathcal{H}_1 &= -\delta I_z + \Omega(\cos\varphi I_x + \sin\varphi I_y), \end{aligned} \tag{2.18}$$

where δ is the detuning of RF driving field from the resonance frequency $\tilde{\omega}_1 = \omega_1 + \delta$, Ω the nuclear Rabi frequency and φ the phase of RF field. To present a clean physical picture, we assume $A_\parallel \gg \Omega$ in the following, and ignore the off-resonant driving term in $\mathcal{H}_0$ [2]. Conditional on the NV electronic spin state, the nuclear spin either precesses around the z axis at a rate $-(A_\parallel + \delta)$ ($|m_s = 0\rangle$), or undergoes generalized Rabi oscillation around axis $\vec{n} \propto (\Omega\cos\varphi, \Omega\sin\varphi, -\delta)$ at frequency $\sqrt{\delta^2 + \Omega^2}$ ($|m_s = +1\rangle$).

The analysis above concerns RF control of nuclear spins. We now look at DD that

[1] For a complete treatment, see the supplementary material of [34]

[2] In most experiments, $A_\parallel \sim 10 - 100$ kHz, while $\Omega \sim 1 - 3$ kHz, satisfying $A_\parallel \gg \Omega$. However, the off-resonant driving from Ω in $\mathcal{H}_0$ poses significant issues when RF pulse is divided into very short segments. In experiments, we always numerically check our sequence to avoid large influence.

protects the NV electron, and combine DD and RF to realize desired nuclear spin control.

Similar to the indirect control technique, we use CPMG type of DD of the form $(-\tau-\pi-\tau-)^N$ to decouple NV from the environment. The RF field is interleaved into $N+1$ segments to fit into the free precession periods of CPMG, and are labelled by $k = 1, \ldots, N+1$ (Fig. 2-8). Depending on the initial NV state $|0\rangle$ ($|1\rangle$), the even(odd)-k RF segments are resonantly driving the nuclear spin, while in the other segments the nuclear spin undergoes free precession along z axis for an angle $\varphi_\tau = -\tau(A_\parallel - \delta)$. To constructively build up the RF driving of the nuclear spins, we have to counteract the effects of free precession via the phase of RF field. As shown in [34], by choosing the appropriate RF pulse phases[3]

$$\varphi_k = \varphi_0 + \begin{cases} (k-1)\varphi_\tau & k \text{ odd} \\ (k-1)\varphi_\tau(+\pi) & k \text{ even} \end{cases} \tag{2.19}$$

one drives the nuclear spin coherently in alternating DD interval blocks (Fig. 2-8). The optional π phase in even-k segments switches the DDRF control between an unconditional (π phase off) and a conditional (π phase on) nuclear spin gate on the NV electron. The phase offset φ_0 helps set the nuclear spin driving axis. The conditional gate is of similar form as the CR gate achieved by CPMG (Eq. 2.15)

$$\mathrm{CR}_\varphi(\vartheta) = |0\rangle\langle 0| R_{-\varphi}(\vartheta) + |1\rangle\langle 1| R_\varphi(\vartheta). \tag{2.20}$$

Therefore, a similar advantage immediately manifests: signal from successful individual nuclear spin addressing is present even when the nuclear spin is unpolarized.

The DDRF gate has one significant advantage over indirect control: it does not rely on $A_\perp$ to drive the nuclear spin, allowing control of ^{13}C 's with small $A_\perp$. These ^{13}C 's widely exist (Appendix. D), and match well with our hardware-efficient QEC model to be discussed in the following chapters. DDRF therefore is an enabling technique that grants us access to the very nuclear spins suitable for hardware-efficient QEC

[3]Note there is an overall π phase shift from [34], for convenient definition of x axis.

implementation. As shown later in Sec. 2.3.2, we identify two new ^{13}C 's with DDRF which are invisible in the CPMG spectrum

In addition, DDRF is convenient in several other ways: first, the freedom in choosing δ allows nuclear spin rotation along any arbitrary axis, therefore any $SU(2)$ control in one gate operation. In contrast, the indirect control via CPMG practically only accepts rotations along x or z axes[4], making many useful gates prohibitively long. Second, the RF drive permits freedom in choosing τ to optimize the NV coherence. With the modifications detailed in the next section, DDRF serves as a convenient building block for larger scale quantum information applications like QEC (Sec. 5).

DDRF Sequence: Improvement

Experimentally, there is one inconvenience of DDRF in its pristine form: NV is a sensitive magnetometer, and picks up a phase induced by the z component of the RF driving field. Consequently, a phase shift is required for all the MW pulses to apply correct control and for accurate interpretation of the results. In principle, the required phase shift could be calculated and compensated in the sequence if the precise waveforms of RF pulses are known. In reality, it poses a hurdle to the usage of DDRF as a single building block for larger quantum circuits. Furthermore, RF amplifiers introduce nonlinear response, making the RF induced phase shift unpredictable. As a result, the original work [34] does not use an RF amplifier for the most part to avoid this issue, making the DDRF gate too slow to keep NV coherent at room temperature. To make the nuclear spin control fast enough to be compatible with NV's coherence time at room temperature, we have to incorporate the RF amplifier. This requires an improved DDRF sequence that builds in cancellation of the phase on NV induced by RF, in the absence of perfect knowledge of the waveform.

Here we improve the original DDRF sequence to build-in this phase cancellation by introducing symmetry into the sequence. This combines two experimental tricks. We start by theoretical analysis of the phase induced by RF on NV.

[4]Limited by the hardware time resolution, it is experimentally prohibitive to achieve high-fidelity control along arbitrary axis using CPMG.

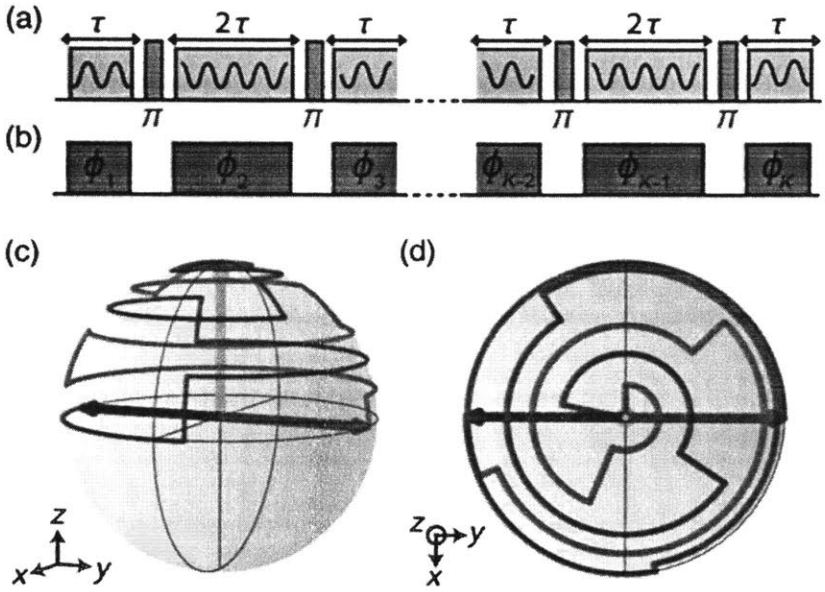

Figure 2-8: (a) Illustration of the pulse sequence employed to realize a DDRF gate. Dynamical decoupling pulses on the electron spin (purple) are interleaved with rf pulses (yellow), which selectively drive a single nuclear spin. (b) Illustration showing that the initial state of the electron spin determines which RF pulses are resonant with the nuclear spin. If the electron spin starts in $|1\rangle$, the odd RF pulses (red) are resonant. For initial electron state $|0\rangle$, the even (blue) RF pulses are resonant. The phase of each RF pulse is adapted to create the desired nuclear spin evolution, accounting for periods of free precession according to Eq. 2.19. (c) Nuclear spin trajectory on the Bloch sphere for a conditional rotation with $N = 8$ electron decoupling pulses. Starting from the initial nuclear state $|\uparrow\rangle$ (yellow), the red (blue) path shows the nuclear spin evolution for the case where the electron starts in the state $|1\rangle$ ($|0\rangle$). The final state vectors are antiparallel along the equator; therefore, the gate is a maximally entangling two-qubit gate. (d) Top-down view of (c). The figure is reprinted from ref. [34].

The RF field along z axis takes the form $B_z \sin(\omega_1 t + \varphi)$. The phase on NV due to an RF pulse of duration t_{RF} is therefore [100, 101]

$$\Phi(t_{RF}, \varphi) = \int_0^{t_{RF}} \Omega_z \sin(\omega_1 t + \varphi), \tag{2.21}$$

where $\Omega_z = \gamma_e B_z$ is the energy splitting of NV due to the z component B_z of the RF driving field. If Ω_z is constant, we see immediately by enforcing each RF pulse length to be an integer number of RF periods $\omega_1 t_{RF} = 2m\pi, m \in \mathbb{Z}$, the phase on NV $\Phi(t_{RF}, \varphi)$ cancels out independently of the RF pulse phase φ. This is convenient because it leaves the freedom of choosing φ to satisfy Eq. 2.19, and it works out nicely for the scheme of Bradley et al. [34] in the absence of an RF amplifier. Nevertheless, the nuclear spin control is slow due to the weak RF field. The gate time is comparable to NV's coherence time at room temperature, making coherent control of the quantum register at room temperature challenging. The control speed could be increased by an RF amplifier, however, the non-linear response of the amplifier during the pulse rise and fall causes deviation from theory. In particular, the amplitude Ω_z is no longer constant in time in Eq. 2.21. Consequently, when an RF amplifier is in use, the uncertainty in Φ requires the authors to sweep the phase of the readout MW $\frac{\pi}{2}$ pulse for every spectroscopy data point to distinguish loss of coherence (successful CR gate) from an NV phase shift due to RF pulses. This makes the whole experiment unnecessarily long, as shown in Fig. 3 of ref. [34]. The uncertainty in Φ therefore prohibits the sequence in its current form from being implemented as a single block for larger quantum circuits.

We remark that Φ is fully determined by the waveform of RF control field. This statement holds true even when the RF field is distorted from sinusoids due to the RF amplifier. Based on this, we come up with the second trick to refocus and cancel out the unknown Φ by introducing symmetry in the improved DDRF sequence, in the presence of unknown non-linear response of an RF amplifier.

Here we make a distinction between the length of RF pulse t_{RF} and half of the interpulse delay τ in DD, setting $t_{RF} < \tau$. We first slice all the $2t_{RF}$ RF pulses in

Fig. 2-8 into two pieces of length t_{RF}. We then look at each building block of DDRF $(-\tau - \pi - \tau-)$ (Fig. 2-9). When the RF phase relation is satisfied (Eq. 2.19), the freedom in placing RF pulse wherever inside τ allows us to enforce the same absolute initial phase of $\mathrm{RF_L}$ and $\mathrm{RF_R}$, which are the RF segments to the left and right of the $k-1$ th MW π pulse (Fig. 2-9)

$$\omega_1 t_{k-1}^L + \varphi_{k-1} = \omega_1 t_{k-1}^R + \varphi_k = 0, \tag{2.22}$$

where t_{k-1}^L, t_{k-1}^R are the starting time of the two RF pulses, to be solved for. The two RF pulses $\mathrm{RF_L}$ and $\mathrm{RF_R}$ have the same absolute initial phase, frequency and duration, therefore the same exact waveform. Their corresponding phase effects $\Phi_{\mathrm{L/R}}$ imposed on NV are the same. Although the values of $\Phi_{\mathrm{L/R}}$ are unknown, they will be cancelled by the MW π pulse between them.

So far, we have assumed the waveforms of distinct RF pulses are the same after RF amplification. This is supported by experimental results. We observed reproducible phase effects on NV induced by the RF in the original DDRF sequence, indicating that the response of RF amplifier during rise and fall is fixed and reproducible in experiments even though it is unknown[5]. Therefore, even with no knowledge of the exact form of the amplifier's transfer function, it is possible to introduce symmetry to the original DDRF sequence to refocus and cancel out the effects.

Furthermore, to avoid instability in the response of RF amplifier, we enforce an additional restriction: the absolute phase at the beginning of every pulse is 0, such that the amplitude of every RF pulse starts from and ends at 0 (Eq. 2.22).

Combining all these constraints together:

$$\begin{aligned} &\varphi_k = \varphi_0 + \begin{cases} (k-1)\varphi_\tau & k \text{ odd} \\ (k-1)\varphi_\tau(+\pi) & k \text{ even} \end{cases}, \\ &\omega_1 t_{RF} = 2m\pi, m \in \mathbb{Z} \\ &\omega_1 t_{k-1}^L + \varphi_{k-1} = \omega_1 t_{k-1}^R + \varphi_k = 0, \end{aligned} \tag{2.23}$$

[5]This is also indicated by results in Fig. 3 of [34]

we have a DDRF sequence with built-in symmetry that cancels out any unwanted phase effects on NV due to RF waveform distortion. This allows usage of an RF amplifier, enabling faster nuclear spin control than NV decoherence at room temperature. This sequence is in turn a suitable building block for room-temperature applications.

DDRF Sequence: Experiment

In the DDRF experiment, we follow the same steps as with indirect control: we first prepare the NV in $\frac{1}{\sqrt{2}}(|0\rangle + |1\rangle)$, then apply the conditional DDRF sequence. A final MW $\frac{\pi}{2}$ pulse brings the NV back to its eigenbasis before optical readout. We used an RF amplifier, and the modifications to the original DDRF sequence allowed us to cancel out the phases on NV induced by RF.

As a first demonstration, we fixed $N = 32$ and swept the RF frequency to obtain the spectrum of neighboring ^{13}C of the NV, shown in Fig. 2-10(a). Note that to maximize the contrast of spectroscopy, we chose $\varphi = x, \vartheta = \pi$ in Eq. 2.20, which is not an entangling gate. At the end of the gate, the NV is decoupled from the ^{13}C , and picks up a π phase shift if the RF pulse is resonant with a specific ^{13}C , manifesting itself as a dip in the spectrum. For better spectral resolution and to avoid crosstalk between nearby ^{13}C 's, a total gate time of ~ 1 ms was used. From the spectrum, we can clearly identify 8 distinct ^{13}C dips, which are labelled by their index in Fig. 2-10(a).

Care has to be taken in mapping dips to individual ^{13}C 's. Constructive build-up of RF driving field is possible when

$$(\omega_L - \tilde{\omega}_1)\tau = \varphi_\tau + 2m\pi, m \in \mathbb{Z}. \tag{2.24}$$

In other words, for $\tilde{\omega}_1 = \omega_1 + \frac{2m\pi}{\tau}$, one might expect dips due to off-resonant driving. The corresponding amplitude has to be determined numerically. In DDRF spectrum experiment, $\tau = 17.141\ \mu s$ gives an off-resonant dip every 58.34 kHz. We find dips $\#3, 5, 6$ correspond to the first order off-resonant driving of ^{13}C 's D, E, A located

at dips #7, 8, 1. This is further confirmed by a different DDRF spectrum using $\tau = 15.237\ \mu s$, shown as crimson dashed line in Fig. 2-10(a). The dips #5, 6 disappeared, while the dip at position #3 is now off-resonantly driving the ^{13}C E (previously D). In total there are 5 ^{13}C 's [6], and we label them ^{13}C A (dip #1), B (dip #2), C (dip #4), D (dip #7), E (dip #8), as shown in Fig. 2-10(a).

After we have identified and isolated individual ^{13}C 's, we show selective nuclear spin Rabi nutation. We use ^{13}C A as an example. Fixing $\tau = 15.231\ \mu s = 8\frac{2\pi}{\omega_L}$, $t_{RF} = 12.380\ \mu s = 6\frac{2\pi}{\omega_1}$, we swept the number of π pulses N and observed the nuclear Rabi oscillation of a weakly coupled ^{13}C (Fig. 2-10(b)). We attribute the decoherence to a combination of inaccurate RF frequency, T_2^e of NV electron, T_2^{*n} of ^{13}C , and pulse errors. Note that as mentioned earlier, the off resonant RF driving effect becomes significant when we decrease both t_{RF}, τ. Checked by both numerical simulation and experiment, this happens when $t_{RF}, \tau \sim< 10\ \mu s$ for this ^{13}C . Therefore, we avoid sweeping t_{RF} directly and instead sweep N. Note that in addition to the decay, the contrast is limited by crosstalk from nearby ^{13}C as well. The detuning from driving a nearby ^{13}C is roughly on the same order of the nuclear Rabi frequency, causing the DDRF sequence to drive simultaneously multiple ^{13}C 's. In this case, from simulation we estimate $\sim 5\%$ infidelity due to the nearest neighbor ^{13}C B. This can easily improve by increasing the total gate time and using weaker RF driving power, as done in the spectrum measurement (Fig. 2-10(a)).

Finally, we compare the CPMG spectrum (Fig. 2-10(c)) and DDRF spectrum (Fig. 2-10(a)) of the same NV. As discussed before, DDRF does not rely on $A_\perp$ to drive the nuclar spin. In turn, all ^{13}C 's with sufficient hyperfine coupling should appear in the DDRF spectrum, regardless of the strength of $A_\perp$. On the other hand, the CPMG control rests exclusively on $A_\perp$, and only ^{13}C 's with large enough $A_\perp$ will appear in the CPMG spectrum. Therefore, dips that appear in DDRF spectrum but not correspondingly in the CPMG spectrum suggest small $A_\perp$ hyperfine interaction strength. We have examined all 5 ^{13}C 's, and found corresponding dips in the CPMG

[6]This number is significantly lower than the average of 12 ^{13}C 's in a quantum register (Appendix. D), because we select NVs with long coherence time T_2^* with ramsey experiment, which indicates a smaller nuclear spin bath that causes dephasing.

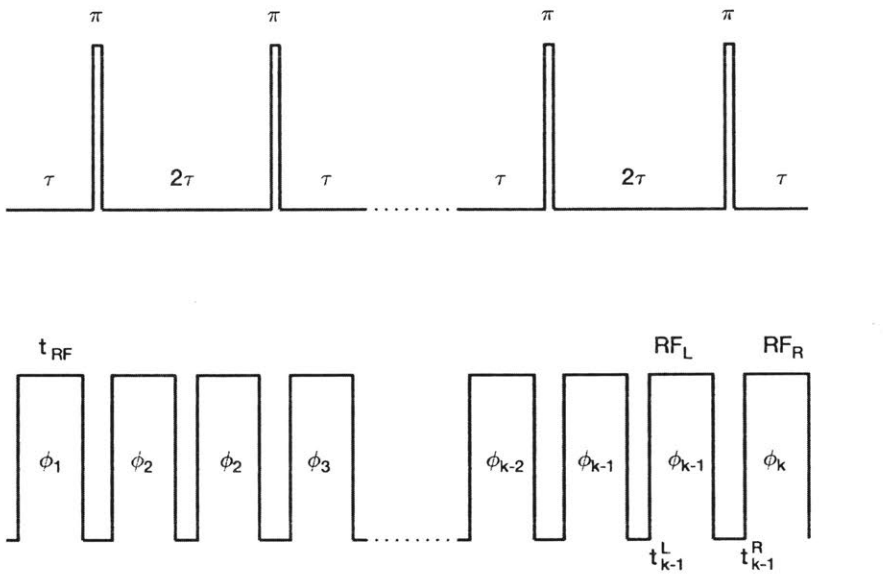

Figure 2-9: Improved DDRF sequence. Firstly we split the continuous 2τ RF pulses in Fig. 2-8 into two separate t_{RF} segments. Phase of each RF segments φ_k still follows Eq. 2.19. In additional to enforcing $\omega_1 t_{RF} = 2m\pi$, we dynamically adjust the starting positions t^L_{k-1}, t^R_{k-1} of each RF pairs to the left and right of the $k-1$th π pulse, such that the absolute phase for $\mathrm{RF_L}$ and $\mathrm{RF_R}$ is $\omega_1 t^L_{k-1} + \varphi_{k-1} = \omega_1 t^R_{k-1} + \varphi_k = 0$. Then the amplifier response is stable and the phase on NV induced by $\mathrm{RF_{L(R)}}$ cancels out each other by the refocus of the $k-1$th π pulse.

spectrum for ^{13}C B, C, E, which are labelled by red circles in Fig. 2-10. There are no significant dips for ^{13}C A, D, which should appear at positions indicated by the crimson dashed line and black dash-dotted line in Fig. 2-10(c). This indicates $A_\perp \sim <$ 12 kHz for ^{13}C A, D. Going to high N of CPMG spectrum, one can set a better upper bound for $A_\perp$. As we will show in the next two chapters, these ^{13}C 's share the same decoherence model as the native ^{14}N , which is pure dephasing induced by a common fluctuator, and are suitable for hardware-efficient QEC.

2.3.3 Conclusion

In this chapter, we have introduced the naturally occuring quantum register of NV-^{14}N -^{13}C . In a natural abundance diamond chip, centered around each NV, the quantum register consists on average of 12 ^{13}C nuclear spins that has sufficient hyperfine interaction strengths suitable for selective addressing and control on the single

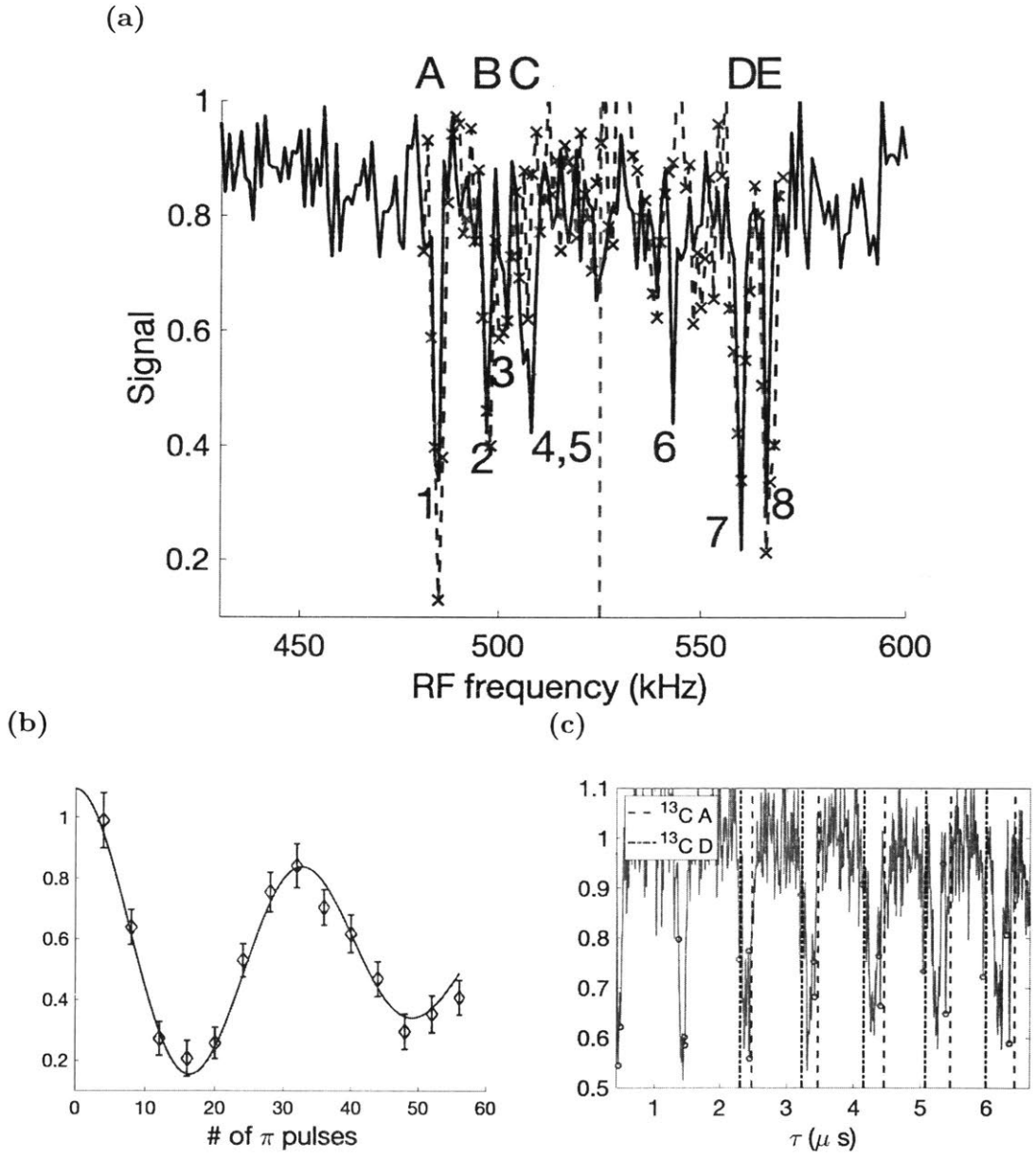

Figure 2-10: (a): DDRF spectrum of one NV at 490 G. Each of the 8 dips addresses an individual ^{13}C . The gray dashed line indicates the Larmor frequency of ^{13}C . (b): DDRF Rabi oscillation. (c) CPMG-32 spectrum of the same NV. 3 out of the 5 ^{13}C 's identified in DDRF spectrum manifest themselves via dips in CPMG spectrum, shown by red circles. We do not observe dips due to ^{13}C A, D, which should appears at positions indicated by the crimson dashed line and black dash-dotted line, indicating $A_\perp \sim< 12$ kHz.

spin level. We have shown single nuclear spin control of both ^{14}N and ^{13}C .

Since precise quantum control relies on accurate knowledge of the system, we in turn use quantum control to deduce with high precision the hyperfine interaction strength between the nuclear spin under control and the NV electron. Using two different nuclear spin control techniques, we could extract different components of the hyperfine interaction matrix. In particular, for direct RF drive, as demonstrated with ^{14}N , we observed enhanced nuclear Rabi oscillation due to forbidden transition. We harnessed the strong dependence of this enhancement on the transverse hyperfine coupling to determine its value with higher precision than previously published results. For indirect control using NV as an actuator, as demonstrated with ^{13}C via CPMG sequence, we achieved universal control of the nuclear spins. Through the resonance condition and nuclear Rabi frequency, we extracted the $S_z I_x$ component of the hyperfine coupling matrix.

Furthermore, we demonstrated an improved DDRF sequence, which combines the advantages of both indirect and direct control techniques. In particular, it drives the nuclear spins independent of the transverse hyperfine coupling strength. Our modification improves the original DDRF sequence and cancels out any effect from the RF driving field on NV electron. This allows the use of an RF amplifier, and enables more than 4X faster nuclear spin control, making the sequence suitable as a single gate to be implemented in larger quantum circuits, as shown in our QEC experiments in Chapter. 5.

Last but not least, the combination of CPMG spectrum and DDRF spectrum uniquely identifies ^{13}C 's whose $A_\perp$ hyperfine terms are small. This provides us a convenient way to isolate ^{13}C 's whose decoherence is predominantly pure dephasing induced by the thermal fluctuation of NV (see Chapter. 3), suitable to form the logical qubits in our hardware-efficient QEC code (see Chapter. 4, 5).

THIS PAGE INTENTIONALLY LEFT BLANK

Chapter 3

Study of Nuclear Spin Dephasing Mechanism

Equipped with experimental tools to individually address, characterize and control the nuclear spins (see Chapter. 2), the quantum register in diamond proves a promising platform, where the nuclear spins serve as physical qubits and the NV electronic spin as the ancillae. Following the philosophy of hardware-efficient QEC, we want to understand the decoherence of these qubits better and develop a hardware-efficient QEC code that requires less resources and is more robust.

In this chapter, we focus on the intrinsic strongly-coupled ^{14}N nuclear spin as an example. We first quantitatively understand its decoherence mechanism, identifying as its source the electronic spin that acts as a quantum fluctuator. We then propose a scheme to protect the quantum memory from the fluctuating noise by applying dynamical decoupling on the environment itself. We demonstrate a factor of 3 enhancement of the storage time in a proof-of-principle experiment, showing the potential for a physical qubit that combines fast operation with long coherence time.

We remark that this dephasing model generalizes to all ^{13}C 's in the quantum register–they are strongly coupled to NV[1], and one single T_1 flip of NV fully decoheres the ^{13}C 's. In other words, the dephasing noise for different nuclear spins is correlated.

[1]Here by "strongly coupled" we compare the hyperfine interaction strength to the fluctuator's flip rate ($1/T_1^e$). This is not to be confused when we refer to "weakly-coupled" ^{13}C , meaning $A_{\|} < 1/T_2^{*e}$. The meaning should be clear in the context.

This lays the foundation of our hardware-efficient QEC code induced by a common fluctuator, as detailed in the next Chapter. 4.

3.1 Introduction

Quantum technologies, especially those based on solid-state systems such as superconducting qubits [65], Nitrogen-Vacancy (NV) centers in diamond [69, 63], and dopant spins in silicon [233], have seen significant progress over the past few decades. Qubits embedded in solid-state systems are advantageous because of their compatibility with existing semiconductor fabrication techniques that can offer avenues for scalability. The drawback, however, is their intrinsic noisy environment due to strong couplings to their solid-state host. The fluctuating environment renders qubits fragile, leaving demonstrations of even small scale quantum computing devices (20-50 qubits) challenging [25].

While further improvements can come from more carefully engineering the qubit systems to remove undesired noise sources and reduce the number of decoherence channels, achieving fault tolerance will still require some form of quantum error correction (QEC). Recent developments include both theoretical proposals for more powerful QEC protocols [206] and experimental attempts at correcting or detecting quantum errors [216, 203, 129]. Despite these advances, we have only seen few experiments yielding better error rate of the error-corrected qubit than the best single qubit in the same system [160, 102]. This is because the recovery operation needed for QEC most likely introduced more error than it corrected. A simpler QEC strategy, avoiding measurement and recovery operations, is to decouple qubits from the environment using dynamical decoupling (DD). This technique, going back to NMR's spin echo [95], enjoys great success thanks to its ease of implementation. In addition, it is compatible with many quantum information processing protocols [116, 39, 230] and can be concatenated with active QEC [163, 36, 33]. Still, DD has traditionally been applied to refocus slow-varying, weakly coupled environments that can often be modeled as classical bath [28], while its usefulness to decouple from strongly interacting

quantum environments is less clear [19].

Here, we explore the effectiveness of DD to increase the coherence time of a spin qubit in the presence of a strongly interacting quantum fluctuator. We first introduce and verify a quantitive model of the decoherence process of a qubit (the ^{14}N nuclear spin of a Nitrogen-Vacancy center) subject to random telegraph noise (RTN) arising from the fluctuation of either a spin-1/2 or spin-1. Then, based on the model, we find the requirement on the DD control sequence that achieves qubit protection from the RTN. It turns out that, due to the slow control on nuclear spin compared to the hyperfine interaction A, any DD sequence applied to the nuclear spin would not meet the requirement and still yield the same coherence time, T_2^{*n}. However, we find that by modulating the noise source itself we can efficiently refocus its effects: control on the NV electronic spin is fast enough to satisfy the DD requirement, and can extend the qubit coherence time beyond the limit imposed by the fluctuator noise. Finally, we realize a proof-of-principle demonstration of these ideas, by protecting the ^{14}N nuclear spin from RTN of a short-lived effective electronic spin-1/2.

3.2 Fluctuator Model & Experiment

Random telegraph noise (RTN), often responsible for $1/f$ noise, is ubiquitous in solid-state nanodevices [161] and is often the main source of decoherence for quantum dots [23] and most notably for superconducting qubits [35, 23, 61]. Here we focus on another exemplary system, nuclear spin qubits in the presence of a fluctuating electronic spin. Specifically, we consider a quantum register consisting of the electronic spin-1 of NV (in the following, we will refer to this simply as NV), its native ^{14}N nuclear spin-1, and possibly a few close-by ^{13}C nuclear spins. With this system, researchers have demonstrated quantum information storage [142, 72], quantum error correction [216, 203], quantum feedback control [101] and high-sensitivity magnetometry [16, 229], taking advantage of the long dephasing time T_2^{*n} of the nuclear spin, which is usually one to two orders or magnitude longer than that of the NV. Long though it is, T_2^{*n} is limited by the NV relaxation time T_1^e ($\sim$ few ms) [142, 229, 188].

Random NV flips due to T_1^e process result in a 3-level RTN; the nuclear spin picks up a random phase from the RTN and decoheres. As explained below, when the hyperfine interaction strength is larger than the T_1^e flip rate, T_2^{*n} is strictly limited by T_1^e. To extend T_2^{*n} beyond this limit, previous efforts have focused on weakly coupled nuclear spins, employing motional narrowing [142, 109], or decoherence-free subspace [172, 218]. On the other hand, strongly coupled nuclear spins are favorable because they provide fast [44, 179, 188], and direct control. Here, we look into the regime of strongly coupled nuclear spins, where previous methods do not work well. In particular, we work with the native ^{14}N nuclear spin, because it is ubiquitous and has proven useful in the NV-^{14}N quantum register [72, 156, 16, 229, 101]. For this system, the previous approaches do not work well, nor does implementing a simple spin echo [188]. After gaining a deeper insight into the fluctuator model, we will show how to overcome this challenge.

3.2.1 Spin-Fluctuator modeled as a random walker

We consider a system of two spins interacting via an hyperfine coupling A that we describe semi-classically using a spin-fluctuator model [22].

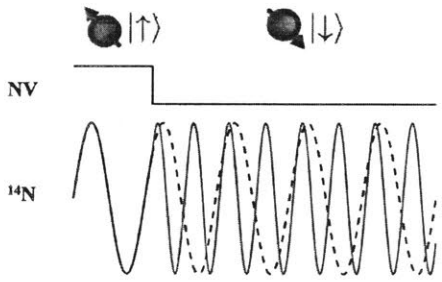

Figure 3-1: Qubit decoherence under random telegraph noise. The fluctuator (NV) randomly flips between its two eigenstates (here from $|\uparrow\rangle$ to $|\downarrow\rangle$) changing the rate at which the qubit (^{14}N) accumulates a phase. For a representative RTN trace, we show that in the absence of a fluctuator jump, the qubit population would continue to oscillate at the same rate (dashed line), while after a fluctuator jump, the oscillation rate accelerates (solid red line). As the jump timing is random, the observed average dynamics is decoherent.

We model the intrinsic ^{14}N nuclear spin I of the NV center as a random walker,

whose phase evolves subject to the state of its neighboring electronic spin S that acts as a strongly coupled fluctuator and generates RTN (Fig. 3-1). In such analogy, the velocity v of the random walker is linked to the phase accumulation rate of the qubit, and is set by the hyperfine interaction, $v = m_S A$. The fluctuator flips at a rate γ between any two m_S states due to spin-lattice relaxation, inducing a change in the value of the hyperfine coupling, $m_S A$, thus at each such event the walker's velocity v also changes. In between fluctuator jumps, the walker covers a distance representing the accumulated phase between qubit states.

For a 2-level fluctuator (2LF), the random walker has only two possible directions, left or right, and its motion can be described by the system of differential equations:

$$\begin{cases} \partial_t \hat{p}_l(\varphi,t) &= -\gamma[\hat{p}_l(\varphi,t) - \hat{p}_r(\varphi,t)] + v\partial_\varphi \hat{p}_l(\varphi,t) \\ \partial_t \hat{p}_r &= -\gamma(\hat{p}_r - \hat{p}_l) - v\partial_\varphi \hat{p}_r, \end{cases} \tag{3.1}$$

where $\hat{p}_l(\hat{p}_r)$ is the probability of reaching φ at time t from the left(right). The spin coherence is given by the average accumulated phase, $\langle e^{i\varphi}(t)\rangle = \int \hat{P}(\varphi,t)e^{i\varphi}d\varphi$, where $\hat{P}(\varphi,t) = \hat{p}_l + \hat{p}_r$ is the total probability of reaching φ at time t. Note that this is the Fourier transform of $\hat{P}$, $P(k,t)$, evaluated at $k=-1$. We can thus more compactly write the relevant equations of motion as $\partial_t \vec{P}(k,t) = M_k \vec{P}(k,t)$, that is

$$\frac{\partial}{\partial t}\begin{pmatrix} P \\ p \end{pmatrix} = \begin{pmatrix} 0 & -ikv \\ -ikv & -2\gamma \end{pmatrix}\begin{pmatrix} P \\ p \end{pmatrix}, \tag{3.2}$$

where $p(k,t) = p_r(k,t) - p_l(k,t)$.

We can similarly describe the spin dynamics in the presence of a three-level fluctuator (3LF), where one of the levels corresponds to a "rest" state $v=0$ (no phase accumulation), with corresponding probability p_0:

$$\frac{\partial}{\partial t}\begin{pmatrix} P \\ p^+ \\ p \end{pmatrix} = \begin{pmatrix} 0 & 0 & -ikv \\ 2\gamma & -3\gamma & -ikv \\ 0 & -ikv & -3\gamma \end{pmatrix}\begin{pmatrix} P \\ p^+ \\ p \end{pmatrix}, \tag{3.3}$$

where $p^+ = p_l + p_r$ and here $P = p_l + p_r + p_0$. The spin decay is then given by

$\langle e^{i\varphi}(t)\rangle = e^{M-1t}P(-1,0)$ and is characterized by a typical timescale T_2^{*n}. Note that since we consider the fluctuator to be either a spin-1/2 or a spin-1, we have $v = A/2(A)$ and $\gamma = 1/2T_1^e(1/3T_1^e)$ for the 2LF(3LF).

In the strong fluctuator regime that we focus on, intuitively a single fluctuator jump is enough to totally decohere the nuclear spin. Then, provided $v/\gamma \gg 1$, the spin decay rates doe not depend anymore on v but only on the jump rate. Indeed, we find $T_2^{*n} = 2T_1^e(1.5T_1^e)$ for the 2LF(3LF). This strict limit on T_2^{*n} for the strong fluctuator is in sharp contrast to the weak fluactuator case, where T_2^{*n} increases as the hyperfine interaction strength decreases (See Appendix. C.2.4).

3.2.2 Experimental results

To verify the validity of the spin-fluctuator model, we measure and compare T_1^e of the Nitrogen-Vacancy center electronic spin and T_2^{*n} of its native ^{14}N nuclear spin. All experiments are performed using a home-built confocal microscope, with single NV centers in an electronic grade diamond sample (Element 6, ^{14}N concentration $[^{14}N] < 5$ ppb, natural abundance of ^{13}C). We work at a magnetic field of 424G, close to the excited state level anti-crossing, to polarize the ^{14}N nuclear spin [106]. A 1.5mW laser of 2μs duration polarizes the hybrid NV-^{14}N system into $|m_S = 0, m_I = +1\rangle$ with high fidelity. Microwave (MW) and radiofrequency (RF) pulses are delivered through a 25μm wide copper wire to have precise control of the NV and ^{14}N spin states.

For T_1^e measurement, a laser pulse first initializes the system into $|0,+1\rangle$. Then we apply a strong MW pulse ($t_\pi = 44$ ns) to prepare it to the desired state $|-1,+1\rangle$. The NV is free to fluctuate due to T_1^e process before we measure the remaining population in $|-1,+1\rangle$ obtaining the signal S_{-1}^{-1} where the sub(super)script refers to the initial (final) electronic spin state. We also measure the population in the state $|0,+1\rangle$ obtaining the signal S_{-1}^{0}. T_1^e is extracted to be 4.3 ± 0.3 ms by fitting to the difference of the two measurements $S_{-1}^{-1} - S_{-1}^{0}$.

For T_2^{*n} measurement, we implement a nuclear Ramsey sequence in the electronic $m_s = -1$ manifold, where the larger nuclear spin energy splitting (due to the hyperfine coupling) allows faster driving. The system is first prepared to $|-1,+1\rangle$, as described

above, before being coherently driven to a nuclear superposition state $(|-1,+1\rangle + |-1,0\rangle)/\sqrt{2}$ using on-resonant RF field. After a free evolution period, we convert nuclear spin coherence to populations with a second RF $\pi/2$ pulse, $\alpha|-1,+1\rangle+\beta|-1,0\rangle$. Finally, the nuclear spin is read out by mapping its state to the NV electronic spin, using a selective MW pulse ($t_\pi = 1.1\mu$s). This pulse creates the entangled state $\alpha|0,+1\rangle+\beta|-1,0\rangle$ between the NV and ^{14}N , allowing optical readout of the nuclear spin state population $|\alpha|^2, |\beta|^2$ with high SNR.

Isolating the bare contribution of the nuclear spin dephasing in the fluorescence signal decay is nonetheless not straightforward as the consequences of NV random flips are three-fold. First, they induce the nuclear spin dephasing that we aim at measuring. Second, they modify the NV state, leading the second RF $\pi/2$ pulse to be off-resonance and preventing the transfer of the nuclear coherence into population difference. Finally, they also induces errors in the mapping between nuclear and electronic spin states as the NV state is not fully polarized anymore.

Fortunately, in the strong fluctuator regime, one flip of the fluctuator is enough to decohere our qubit, which allows us to neglect the two last errors. The bare contribution of the nuclear spin dephasing can be isolated by recording the signals obtained from nuclear Ramsey sequence with 1) no phase difference between the two RF $\pi/2$ pulses and 2) a π phase shift. The last two effects that cause imperfect readout of the nuclear spin have an equivalent contribution in both Ramsey sequences, just creating a common error that is suppressed when subtracting the two Ramsey signals (Appendix. C.1.1). We can then measure a dephasing time $T_2^{*n}= 5.6 \pm 1.7$ ms as shown in Fig. 3-2b. This verifies our prediction from spin-fluctuator model with 3 levels, $T_2^{*n} = 1.5T_1^e$.

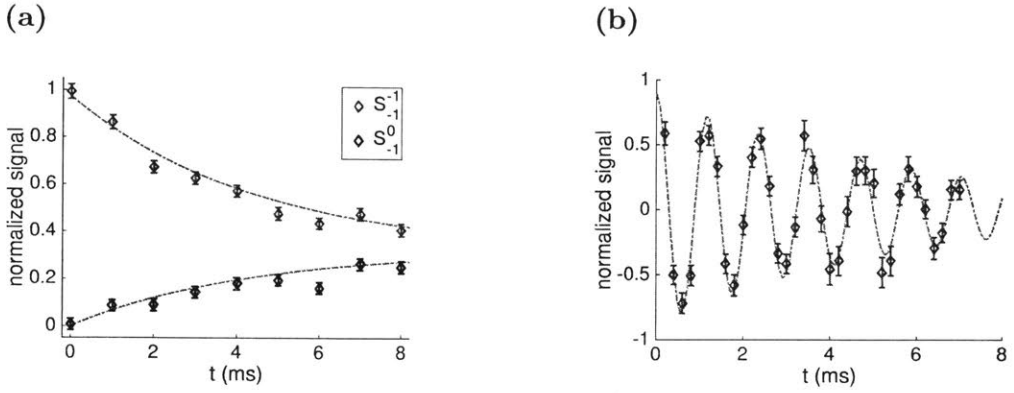

Figure 3-2: (a) Natural relaxation decay of a single NV population and (b) cohernce decay of its native ^{14}N under a Ramsey sequence. The dashed lines are fits to the expected dynamics, yielding T_1^e= 4.3(3) ms and T_2^{*n}= 5.6(1.7) ms. These values satisfy $T_2^{*n} = 1.5T_1^e$, as predicted by the spin fluctuator model.

3.3 Dynamical Decoupling in the strong coupling regime

3.3.1 Theory

To protect the nuclear spin qubit from RTN generated by the NV, we resort to dynamical decoupling (DD). Usual DD schemes are highly effective in protecting qubits from noise provided the pulses are applied at a higher repetition rate than the typical correlation time of the noise. Unfortunately, because of the Markovian nature of RTN, this condition does not apply here. Instead of being set by the fluctuator rate γ, in order for DD to be effective the π-pulse separation time τ must satisfy

$$A \cdot \tau \lesssim 1. \tag{3.4}$$

When applying DD following the well-known CPMG sequence [144] with time between pulses τ, the spin coherence after N pulses is given by

$$\langle e^{i\varphi}(N\tau)\rangle = \{[e^{M_{-1}\tau/2} \cdot U_\pi \cdot e^{M_{-1}\tau/2}]^N \vec{P}\}_1, \tag{3.5}$$

where U_π is the π-pulse operator. For a 2LF this is diag$(1,-1)$, while it is diag$(1,1,-1)$ for a 3LF. As discussed below, it might be possible, and even more convenient, to apply π-pulses on the fluctuator instead of the qubit. Indeed, the desired effect is

to invert the sign of the coupling between the two systems. For a 3LF, this can be achieved by driving the double quantum (DQ) transition $|+1\rangle \leftrightarrow |-1\rangle$. However, for a 3LF there is some freedom on the type of pulses applied. In addition to driving the DQ transition, one can also drive one of the single quantum (SQ) transitions, $|0\rangle \leftrightarrow |\pm 1\rangle$, resulting in

$$U_\pi = \begin{pmatrix} 1 & 0 & 0 \\ 1 & -1/2 & \mp 1/2 \\ 1 & \mp 3/2 & 1/2 \end{pmatrix}.$$

Since the qubit decay under DD is not necessarily purely exponential [Appendix. C.2.3], we define an effective coherence time $T_2^n(\tau)$ through:

$$\langle e^{i\varphi}(N\tau = T_2^n(\tau))\rangle = 1/e \tag{3.6}$$

The dependence of T_2^n on the DD interval τ is shown in Fig. 3-4a. As expected, smaller τ's are better at decoupling the qubit from RTN and at extending T_2^n. Interestingly, the behavior for the 2LF and 3LF is different. For 2LF, DD leaves the decay approximately exponential (see Appendix. C.2.2), with a decay rate

$$1/T_2^n = \gamma - \frac{1}{\tau} \ln \left[\frac{\gamma \sin(W\tau) + \sqrt{v^2 - \gamma^2 \cos^2(W\tau)}}{W} \right], \tag{3.7}$$

where $W = \sqrt{v^2 - \gamma^2}$. For a 3LF, however, the coherence decay is not exponential (See Appendix. C.2.3). Still, we see that, by using DQ pulses to refocus the fluctuator (or applying pulses directly to the qubit), one could in principle fully decouple the qubit from RTN noise when $\tau \to 0$, until nuclear-nuclear dipolar interactions become the dominant noise source [142]. With SQ drive, however, one only protects the qubit from RTN half of the time, therefore the decay rate can at most be reduced to half of its value without DD (Fig. 3-4a).

3.3.2 Experimental results

We now apply these ideas to protect the nuclear spin from the NV RTN and extend its T_2^n beyond the limit of T_1^e.

Due to the strong hyperfine coupling $A = 2.16$ MHz between the electronic and nuclear spin of the NV, the condition (3.4) requires $\tau \lesssim 1\mu$s, which is not feasible given the slow control of the nuclear spin qubit (with typical π-pulse times 50μs). However, as the hyperfine interaction is symmetric with respect to the state of both spins, applying π-pulses on either the qubit or the fluctuator modulates the hyperfine interaction sign and will lead to an effectively weaker averaged hyperfine coupling and thus a slower rate at which nuclear states acquire a random phase. It is consequently possible to take benefit from the electronic driving strength that are typically a few tens to a few hundreds of MHz [83, 62, 181], yielding π-pulses fast enough to meet the requirement of Eq. (3.4).

Another challenge in the experiment is due to the nuclear spin readout, which is indirectly obtained by measuring the NV spin. As mentioned in Sec. 3.2.2, as the NV center state is unknown at the end of the evolution due to T_1^e processes, the nuclear spin mapping from coherence to population states and its readout via the NV electronic spin might fail. This problem is exacerbated when DD is applied, as we expect some qubit coherence to be stored in all NV manifolds. Thus, the differential measurement scheme applied above no longer provides an accurate picture of the nuclear spin coherence decay. In particular, it is no longer possible to fully measure gains in T_2^n beyond T_2^{*n} (see Appendix. C.1.1).

To remove this undesired effect and more precisely verify the protection of the nuclear spin afforded by DD, we engineer a short-lived 2LF, decoupling its evolution (and final state) from the state needed for the correct readout of the nuclear spin. The engineered noise also allows shorter experiments, further avoiding slow external experimental drifts that could hide the gains in coherence time. The artificial 2LF is engineered by applying fast, on-resonant MW pulses to flip the NV electronic spin state between $|0\rangle$ and $|-1\rangle$ (engineered T_1^e flip) at random times following a Poisson

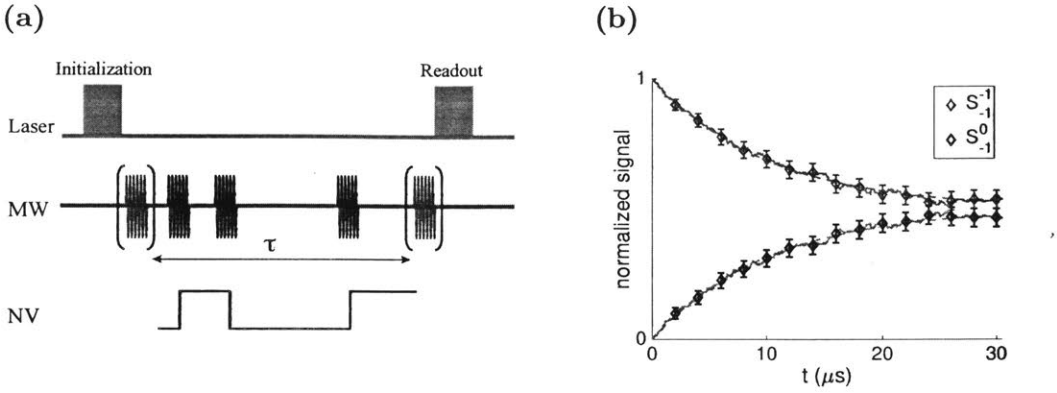

Figure 3-3: (a) Pulse sequence for one engineered T_1^e trace with three fluctuator jumps. The red MW π-pulses prepare and readout the desired NV state. The black MW π-pulses mimic engineered T_1^e flips. (b) Decay of a single NV under engineered T_1^e relaxation noise, simulated by 200 traces of engineered T_1^e flips as described in the main text. Red and black diamonds: S_{-1}^{-1} and S_{-1}^{0} experimental decays. Solid gray line: simulation of T_1^e using the same traces. Gray dashed line: fit to an exponential decay, giving $T_1^e = 10.06(1)\mu$s.

distribution. Figure 3-3a displays one of the 200 engineered T_1^e traces that once averaged simulate an exponential T_1^e decay process. We set the flipping constant of the artificial 2LF in order to obtain a relaxation time $T_1^e = 10\mu$s. This time scale is much longer than the π-pulse length $t_p = 44$ns, and is two orders smaller than that of the natural T_1^e, guaranteeing the third level $|+1\rangle$ of the NV center is not involved in the dynamics and we indeed have an effective 2-level fluctuator.

Figure. 3-3b shows measurement of the engineered T_1^e decay, matching very well with the simulation of the applied 200 engineered T_1^e traces. An exponential fit gives a decay time of $10.06 \pm 0.01\mu$s, in good agreement with our 10μs design. We then use the same engineered T_1^e traces to perform a nuclear Ramsey experiment and measure the resulting coherence time, obtaining an engineered $T_2^{*n} = 22 \pm 4\mu\text{s} = 2T_1^e$ (Figure 3-4b), as expected from the 2LF theory. In order for the readout of nuclear spin state to be accurate, if the NV ends up in $|0\rangle$ due to the engineered flips we apply an extra π-pulse immediately before the readout process, which brings it back to $|-1\rangle$.

Finally, in addition to the engineered T_1^e traces, we apply the Knill-Dynamical Decoupling (KDD) sequence [197] with an interval of $\tau = 200$ns on the NV to decouple ^{14}N from the RTN. We apply ~ 100 DD pulses to measure the nuclear spin coherence

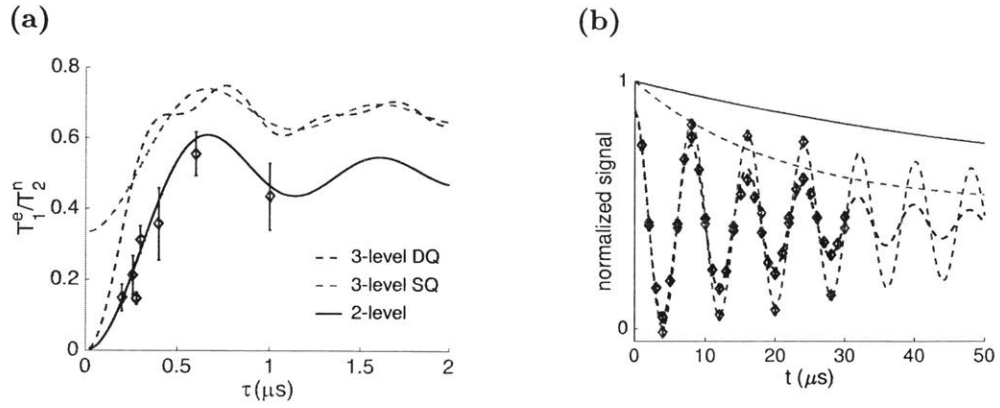

Figure 3-4: (a) Effective coherence time T_2^n for 2LF (black solid line: theory; red diamond: experiment), and 3LF for double quantum drive (red dashed line) and single quantum drive (gray dashed line). The experimental results (for τ = 200, 260, 280, 300, 400, 600, and 1000 ns) agree well with the theoretical prediction, including the somewhat counterintuitive result for τ = 600ns which indeed gives T_2^n<T_2^{*n}; (b) Corresponding T_2^{*n} (black diamond) and T_2^n (red diamond, τ = 200ns DD interval) decay. Dashed lines are fit by exponential decay. Gray dashed and solid lines are the theoretical T_2^{*n} and T_2^n decays calculated according to the spin-fluctuator model.

decay, which according to Eq. 3.7, is expected to follow an exponential behavior. In Fig. 3-4b we compare the experimental (and theoretical) decays with and without DD, clearly showing the improvement achieved by applying a decoupling scheme, proving the successful protection of nuclear spin from its RTN environment. This is confirmed by the measured T_2^n value, extracted from a fit to be T_2^n= 67±17μs, (Fig. 3-4b), clearly exceeding T_2^{*n}, and matching well with theoretical prediction of 71μs. We repeat this experiment with different DD intervals τ, to compare the trend in T_2^n with our theory. The results, shown in Fig. 3-4a, are in quantitative agreement with the predicted behavior, including the somewhat counterintuitive result for τ = 600ns, where the applied DD *accelerates* decoherence, giving T_2^n<T_2^{*n}.

While we demonstrated that dynamical decoupling can be effective in increasing the coherence time affected by a strong random fluctuator only for engineered noise, we remark that our experimental results show that it would be possible to refocus the natural noise as well. Indeed, using a direct readout of the nuclear spin [175, 156] or with a different protocol to map its state onto the electronic spin, it would be possible

to avoid seeing direct effects of the NV T_1^e on the measured nuclear spin coherence. We further performed DD experiments to show that it is practically feasible to implement the necessary number of pulses for decoupling (see Appendix C.1.4) without introducing additional noise due to pulse errors.

3.4 Conclusion

Protecting a qubit strongly coupled to a fluctuating quantum environment is often a challenging task. Here we studied an exemplary system comprising the electronic and ^{14}N nuclear spins associated with the NV center in diamond. While the nuclear spin can act as a long-lived qubit (or memory), the electronic spin, which is necessary for initialization and readout, is also the main source of noise for the qubit. We identified the decoherence mechanism of the nuclear spin qubit and introduced a simple model in terms of a random fluctuator to describe its decoherence. Measurements on the fluctuator and ^{14}N qubit verifies our spin-fluctuator model and show the limit on the qubit coherence. Based on this model, we proposed a method to decouple and protect the nuclear spin from its environment, and demonstrated a factor of 3 increase in coherence time in a proof-of-principle experiment.

Our results pave the way to using strongly coupled nuclear spins, including the ubiquitous native Nitrogen of the NV center, for demanding experiments requiring long quantum memory times, complementing existing techniques applicable only to weakly coupled nuclear spins [142, 172, 218]. In addition, the proposed technique based on DD is compatible with many quantum information processing protocols [116, 39, 230], allowing the full functionality of a quantum register, where the electronic spin performs local operations while the quantum memory is protected. This is in contrast to other protocols where the electronic spin is inaccessible during protection of nuclear spins [53, 142, 109]. Proposals concatenating DD with active QEC [163, 36, 33] also makes it potentially a first layer of protection before applying QEC, enabling scaling-up with less overhead. Finally, the proposed control technique is also applicable to other solid-state systems, for example, superconducting qubits, where single or

ensembles of fluctuators are believed to be the major noise source [22, 194, 161].

We emphasize that this decoherence model generalizes to all ^{13}C 's in the quantum register. They couple to the same NV electron and one single T_1 flip of NV fully decoheres all the nuclear spins in the quantum register. The nuclear spins' decoherence is therefore correlated and induced by a common fluctuator. Knowledge of the decoherence mechanism gained in this chapter, in particular the correlation in nuclear spin decoherence builds up the basis for our search for a hardware-efficient QEC code that is robust and efficient, which is discussed in more detail in the next Chapter.

Chapter 4

Hardware-Efficient Quantum Error Correction for Dephasing Induced by a Common Fluctuator: Theory

Quantum error correction is expected to be essential in large-scale quantum technologies. However, the substantial overhead of qubits it requires is thought to greatly limit its utility in smaller, near-term devices. Here we introduce a new family of special-purpose quantum error-correcting codes that offer an exponential reduction in overhead compared to the usual repetition code. They are tailored for a common and important source of decoherence in current experiments, whereby a register of qubits is subject to phase noise through coupling to a common fluctuator, such as a resonator or a spin defect. The smallest instance encodes one logical qubit into two physical qubits, and corrects decoherence to leading-order using a constant number of one- and two-qubit operations. More generally, while the repetition code on n qubits corrects errors to order $t^{O(n)}$ in the time t between recoveries, our codes correct to order $t^{O(2^n)}$. Moreover, they are robust to model imperfections in small- and intermediate-scale devices, where they already provide substantial gains in error suppression. As a result, these hardware-efficient codes open a potential avenue for useful quantum error correction in near-term, pre-fault tolerant devices.

4.1 Introduction

Decoherence, the uncontrolled decay of coherence in open quantum systems, is a central obstacle to developing coherent quantum technologies such as quantum sensors, networks, and computers. This obstacle is compounded by the destructive nature of quantum measurement: straightforward attempts to identify—and ultimately reverse—decoherence destroy the quantum coherence they seek to protect. Quantum error correction (QEC) is a technique for taming decoherence which sidesteps this issue. It encodes lower-dimensional quantum states into a higher-dimensional quantum system such that decoherence can be detected and approximately reversed without collapsing the encoded state. Specifically, the most common approach encodes k logical qubits into an n-qubit register ($k < n$) whose Hilbert space $\mathcal{H}$ is decomposed into orthogonal subspaces $\mathcal{C}_0, \mathcal{C}_1, \mathcal{C}_2, \ldots$ of dimension 2^k [1]. These subspaces are chosen by specifying operators $E_1, E_2, \ldots$ and demanding that the logical states, which reside in $\mathcal{C}_0$, be mapped to $\mathcal{C}_i$ by E_i without distortion [2]. By performing a partial measurement that reveals *only* which subspace contains the state, and feeding back appropriately, one can reverse the occurrence of any E_i—and more generally, any error in $\mathcal{E} = \text{span}\{I, E_1, E_2, \ldots\}$. The conventional strategy is to pick E_i's so that $\mathcal{E}$ encompasses a broad family of operators on $\mathcal{H}$. Using Pauli operators of weight up to w, for instance, produces a QEC code that corrects arbitrary errors on w qubits. This is a powerful approach, especially in large devices ($n \gg 1$), since it can reverse decoherence with little regard to its physical origins [157, 128]. For smaller devices, however, casting such a wide net requires an overhead of qubits ($n - k$) that is often prohibitive for near-term applications. A more economical strategy for small- and intermediate-scale devices is instead to use a QEC code with $\mathcal{E}$ tailored to include only the dominant, well-characterized decoherence modes. However, while this strategy is well-known (see [157] §10.6.4), few explicit such codes have been discovered; see, e.g., Refs. [126, 173, 124].

[1] In general, there could also be a "remainder" subspace $\mathcal{C}_R$ of arbitrary dimension so that $\mathcal{H} = (\bigoplus_i \mathcal{C}_i) \oplus \mathcal{C}_R$

[2] While it is possible for multiple E_i's to have the same effect on the logical states, thus reducing the number of subspaces required for QEC, we will not deal with such degenerate codes here.

4.2 Theoretical Model

In order to systematically find noise-tailored QEC codes, here we focus on dephasing, since it is the dominant type of decoherence in various experiments. In particular, we consider the common scenario where dephasing in a register of qubits arises primarily due to eigenstate-preserving coupling of each qubit to a common fluctuator, which in turn exchanges energy with an external environment. That is, we consider a Hamiltonian

$$H = H_f^0 + \frac{1}{2}\sum_{j=1}^{n} \omega_j Z_j + H_f^{\text{int}} \otimes \sum_{j=1}^{n} g_j Z_j \tag{4.1}$$

where $[H_f^0, H_f^{\text{int}}] = 0$, and a fluctuator that jumps incoherently between energy eigenstates $\{|\ell\rangle_f\}$ (reflected by a dissipative term in the overall master equation). Moving to the interaction picture, the Hamiltonian (4.1) becomes

$$\tilde{H} = \sum_{\ell} \lambda_\ell \, |\ell\rangle\langle\ell|_f \otimes H_E, \tag{4.2}$$

where $H_f^{\text{int}} = \sum_\ell \lambda_\ell \, |\ell\rangle\langle\ell|_f$ and $H_E := \sum_{j=1}^n g_j Z_j$. When the fluctuator is in state $|\ell\rangle_f$, qubit j has an effective Hamiltonian $\lambda_\ell \, g_j Z_j$ in the rotating frame. Jumps of the fluctuator therefore induce spatially-correlated random telegraph noise in the register, which causes dephasing [136, 153]. This model, which we call *common-fluctuator dephasing* (CFD), often describes the main decoherence mechanism in nuclear spins near spin defects (e.g., Nitrogen-Vacancy centers in diamond [43]) or quantum dots, and can also be significant in superconducting qubits dispersively coupled to a common resonator with non-zero effective temperature [2, 142, 188, 229, 43, 26, 27, 85, 138, 51, 184, 227, 228, 226, 219]. Often the register is read out and/or initialized via the fluctuator, imposing a lower limit on the desirable coupling strengths g_j, and making CFD a significant decoherence mode. Note that CFD does not generally produce a decoherence-free subspace (DFS).

The standard QEC approach to correct dephasing uses E_i's comprising Pauli Z operators on at most w qubits (and I on the rest). There are $\sum_{m=0}^{w} \binom{n}{m}$ such matrices; a simple counting argument (the quantum Hamming bound applied to

phase noise) therefore suggests that $n \geq 2w + 1$ physical qubits are required to protect $k = 1$ logical qubit from arbitrary phase errors of weight $\leq w$ [157]. Indeed, the repetition code saturates this bound: the smallest instance uses $n = 3$ for $w = 1$, has logical states $|0_{\mathrm{L}}\rangle = |{+}{+}{+}\rangle$ and $|1_{\mathrm{L}}\rangle = |{-}{-}{-}\rangle$ where $|\pm\rangle := \frac{1}{\sqrt{2}}(|0\rangle \pm |1\rangle)$, and corrects for $\mathcal{E} = \mathrm{span}\{I, Z_1, Z_2, Z_3\}$. It can correct CFD as follows: In any run of the experiment, the register evolves over time t as $U(\vartheta) = e^{-i\vartheta H_E}$ for some random variable $\vartheta \in [t\lambda_{\min}, t\lambda_{\max}]$ that depends on the fluctuator's trajectory. For short t (understood in units of $1/\max_{j\ell}|g_j\lambda_\ell|$, and often reducible through dynamical decoupling [213, 18, 29, 43]), $U(\vartheta)$ can be approximated as $U(\vartheta) = I - i\vartheta H_E + O(t^2)$. Since $\vartheta H_E \in \mathcal{E}$ regardless of ϑ, this 3-qubit code corrects dephasing at order $O(t)$. More generally, H_E^q contains Paulis of weight $\leq q$, so correcting to order $O(t^q)$ with the repetition code requires $n = 2q + 1$ qubits (for $k = 1$).

While the value of ϑ is unknown and varies from one run to the next, the coupling strengths g_j are often fixed and well characterized. This suggests designing a code that corrects expressly for $\mathcal{E} = \mathrm{span}\{I, H_E, H_E^2, \ldots, H_E^q\}$, and depends on the $\{g_j\}$ in a particular device. A similar counting argument as above suggests that such a code would require $q + 1$ subspaces to protect a logical qubit to order $O(t^q)$, and therefore require

$$n = \lceil 1 + \log_2(q + 1) \rceil \tag{4.3}$$

qubits—an exponentially smaller overhead. We give a family of such codes here for general q and arbitrary coupling strengths $\{g_j\}$. We focus in particular on the $q = 1$ case, where one logical qubit is encoded in two physical qubits rather than three. We construct recovery and logical operations for this code, which can be implemented using a constant number of one- and two-qubit operations.

4.3 Main Results

The decomposition $\mathcal{H}$ into subspaces $\mathcal{C}_i$ for QEC is equivalent to the Knill-Laflamme conditions [119, 21]. For $k = 1$ and $\mathcal{E} = \text{span}\{H_E^j\}_{j=0}^q$, these take the form

$$\langle 0_L | H_E^m | 0_L \rangle = \langle 1_L | H_E^m | 1_L \rangle \tag{4.4}$$

$$\langle 0_L | H_E^m | 1_L \rangle = 0 \tag{4.5}$$

for $0 \leq m \leq 2q$, where we consider values of q that saturate the ceiling in Eq. (4.3) (that is, $q = 2^{n-1} - 1$). Finding a QEC code that corrects this $\mathcal{E}$ therefore requires finding logical states $|0_L\rangle$ and $|1_L\rangle$ that satisfy Eqs. (4.4) and (4.5). We begin with the ansatz

$$|0_L\rangle = \sum_{j=0}^{2^n-1} r_j e^{i\vartheta_j} |j\rangle \qquad |1_L\rangle = \sum_{j=0}^{2^n-1} r_{(2^n-1-j)} e^{i\varphi_j} |j\rangle , \tag{4.6}$$

for $r_j, \vartheta_j, \varphi_j \in \mathbb{R}$, where we use $|j\rangle$ to denote the n-bit binary representation of the integer j. That is, we fix the amplitudes of $|1_L\rangle$ to be those of $|0_L\rangle$ in reverse order. Notice that Eq. (4.6) always satisfies (4.4) for even $m \geq 0$, since $X^{\otimes n} H_E^m X^{\otimes n} = (-1)^m H_E^m$. For odd m:

$$\langle 0_L | H_E^m | 0_L \rangle = - \langle 1_L | H_E^m | 1_L \rangle = \vec{z} \cdot \vec{v}_m, \tag{4.7}$$

where $\vec{z}$, $\vec{v}_m \in \mathbb{R}^{q+1}$ are defined as $z_i = \langle i | Z_L | i \rangle$, with $Z_L := |0_L\rangle\langle 0_L| - |1_L\rangle\langle 1_L|$, and $(\vec{v}_m)_i = \langle i | H_E^m | i \rangle$ for $i \in [0, q]$ and odd $m \in [0, 2q]$. Therefore, Eq. (4.4) is satisfied for all relevant m if $\vec{z} \perp \text{span}\{\vec{v}_m\}$. We can always find such a $\vec{z}$ ($\neq \vec{0}$) since the $\vec{v}_m$'s have dimension $q + 1$ but there are only q of them, so they cannot form a complete basis. One approach is to construct a matrix V with $\vec{v}_m$'s as columns; then, $I - VV^+$ projects onto $\text{span}\{\vec{v}_m\}^\perp$ (where $+$ and $\perp$ denote the pseudoinverse and orthogonal complement, respectively) and therefore has at least one real eigenvector $\vec{u}$ with unit eigenvalue [3]. Taking $\vec{z} = \vec{u}/||\vec{u}||_1$ satisfies Eq. (4.4) since $\vec{u} \cdot \vec{v}_m = 0$ automatically. Finally, building upon a technique developed in Ref. [124] for optimization, we pick

[3] Alternatively, the modified Gram-Schmidt procedure provides a less intuitive but more numerically stable method.

r_j's as

$$(r_j, r_{(2^n-1-j)}) = \begin{cases} (0, \sqrt{z_j}), & \text{if } z_j \geq 0 \\ (\sqrt{-z_j}, 0), & \text{if } z_j < 0. \end{cases} \tag{4.8}$$

This choice ensures that $\langle j|0_L\rangle$ or $\langle j|1_L\rangle$ vanishes for every j, thus satisfying Eq. (4.5). We now have normalized logical states that form a valid QEC code for all $q \geq 1$. Notice that the components of $|0_L\rangle$ and $|1_L\rangle$ generically have unequal amplitudes r_j by necessity, in marked contrast with classical error-correcting codes and most known QEC codes. The phases ϑ_j and φ_j can be chosen arbitrarily—we demonstrate a convenient choice below. The performance of these codes on $n \leq 5$ qubits is shown in Fig. 4-1 using an illustrative model of a normally-distributed ϑ. In addition, we give the pseudothresholds for $n = 2$ and 3 under the same model in the Supplemental Material [1].

4.4 An Example: Two-Qubit Code

To illustrate this QEC code, we consider explicitly the smallest case of $n = 2$ qubits coupled to a two-level fluctuator with $\lambda_{\pm 1} = \pm 1$ [cf. Eq. (4.2)], at high temperature. We will label the register qubits 1 and 2 such that $|g_1| \geq |g_2|$. Note that here—and in general—$H_E = g_1 Z_1 + g_2 Z_2$ is a combination of weight-1 Pauli operators, not a weight-2 Pauli. This H_E gives $\vec{v}_1 = (g_1 + g_2, g_1 - g_2)^\top$. The matrix $I - VV^+$ has only a 1-dimensional eigenspace with unit eigenvalue, spanned by $\vec{u} = (-g_1 + g_2, g_1 + g_2)^\top$, where $\vec{u} \cdot \vec{v}_1 = 0$. If $g_1 > 0$ we find $r_1 = r_3 = 0$ and

$$r_0 = c\sqrt{g_1 - g_2} \qquad r_2 = c\sqrt{g_1 + g_2}, \tag{4.9}$$

where $c = 1/\sqrt{||\vec{u}||_1}$. This gives logical states

$$|0_L\rangle = |\chi_0\rangle\,|0\rangle \qquad |1_L\rangle = |\chi_1\rangle\,|1\rangle \tag{4.10}$$

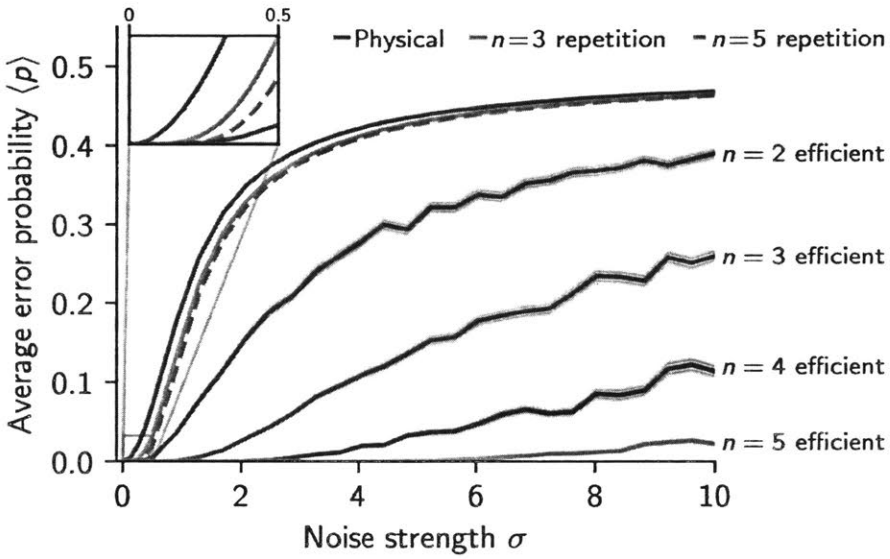

Figure 4-1: **Comparison of QEC codes performance.** We assume that the effect of the quantum fluctuator is to impart a random phase, ϑ, which follows a Gaussian distribution $\vartheta \sim \mathcal{N}(0, \sigma)$ with standard deviation σ. By normalizing the g_j's to lie in $[0, 1]^n$, σ describes the noise strength. CFD followed by a QEC recovery (if applicable) results in an effective phase- or bit-flip channel $\rho \mapsto (1-p)\rho + p\, A\rho A$, where $A = Z$ for the physical qubits, X_{L} for the repetition codes, and Z_{L} for hardware-efficient codes. The average infidelity, average trace distance and diamond distance to I are all $\propto p$. As the performance of all strategies shown depends on $\{g_j\}$, we plot the average of p over $\{g_j\} \in [0, 1]^n$. The error bands for the hardware-efficient codes denote the standard error of the mean from Monte Carlo integration. More details on the numerical implementation are given in [1].

with

$$
\begin{aligned}
|\chi_0\rangle &= c\Big(\sqrt{|g_1 - g_2|}\, e^{i\vartheta_0}\, |0\rangle + \sqrt{|g_1 + g_2|}\, e^{i\vartheta_2}\, |1\rangle\Big) \\
|\chi_1\rangle &= c\Big(\sqrt{|g_1 + g_2|}\, e^{i\varphi_1}\, |0\rangle + \sqrt{|g_1 - g_2|}\, e^{i\varphi_3}\, |1\rangle\Big),
\end{aligned}
\tag{4.11}
$$

where $|0\rangle$ and $|1\rangle$ refer to the states of a qubit. The $g_1 < 0$ case gives the same result up to a relabelling of $|0_{\text{L}}\rangle \leftrightarrow |1_{\text{L}}\rangle$. This code corrects for $\mathcal{E} = \text{span}\{I, H_E\}$; by design, however, it does not correct for $Z_1 Z_2$, nor Z_1 or Z_2 individually, none of which belong to $\mathcal{E}$. Rather, it corrects CFD with fewer qubits than the smallest repetition code precisely because we have chosen not to correct individual Pauli operators.

Observe that Eqs. (4.10) and (4.11) reduce to a DFS in the limit where one exists ($|g_1| = |g_2|$). More generally, notice that the choice $\vartheta_0 = \varphi_1 + \pi = -\vartheta_2 = -\varphi_3 = \vartheta$ for arbitrary ϑ proves convenient: First, it gives $\langle\chi_0|\chi_1\rangle = 0$, and a simple action of H_E on logical states:

$$
\begin{aligned}
H_E\, |0_{\text{L}}\rangle &\propto |\chi_1\rangle\, |0\rangle =: |0_{\text{E}}\rangle \\
H_E\, |1_{\text{L}}\rangle &\propto |\chi_0\rangle\, |1\rangle =: |1_{\text{E}}\rangle\,.
\end{aligned}
\tag{4.12}
$$

Both lines have the same proportionality constant, and we have defined the error states $|0_{\text{E}}\rangle$ and $|1_{\text{E}}\rangle$. We emphasize that since H_E cannot generically be decomposed as a tensor product, it maps most separable states to entangled states; Eq. (4.12)—wherein the first qubit is "flipped" by H_E—is due to our choice of $|0_{\text{L}}\rangle$ and $|1_{\text{L}}\rangle$. Second, consider the orthogonal projectors $P_{\text{L}} = |0_{\text{L}}\rangle\langle 0_{\text{L}}| + |1_{\text{L}}\rangle\langle 1_{\text{L}}|$ and $P_{\text{E}} = |0_{\text{E}}\rangle\langle 0_{\text{E}}| + |1_{\text{E}}\rangle\langle 1_{\text{E}}|$ onto $\mathcal{C}_0 = \text{span}\{|0_{\text{L}}\rangle, |1_{\text{L}}\rangle\}$ and $\mathcal{C}_1 = \text{span}\{|0_{\text{E}}\rangle, |1_{\text{E}}\rangle\}$ respectively ($\mathcal{H} = \mathcal{C}_0 \oplus \mathcal{C}_1$). One can detect an error non-destructively by measuring parity in the $|\chi_i\rangle\,|j\rangle$ basis, which can be done by performing phase estimation (i.e., "phase kickback") on

$$
S = P_{\text{L}} - P_{\text{E}} = U_z \otimes Z_2 \tag{4.13}
$$

with an ancilla [52]. Crucially, the choice of phases in $|0_{\text{L}}\rangle$ and $|1_{\text{L}}\rangle$ makes S separable here, where $U_z := |\chi_0\rangle\langle\chi_0| - |\chi_1\rangle\langle\chi_1|$ is a π rotation about some axis determined by

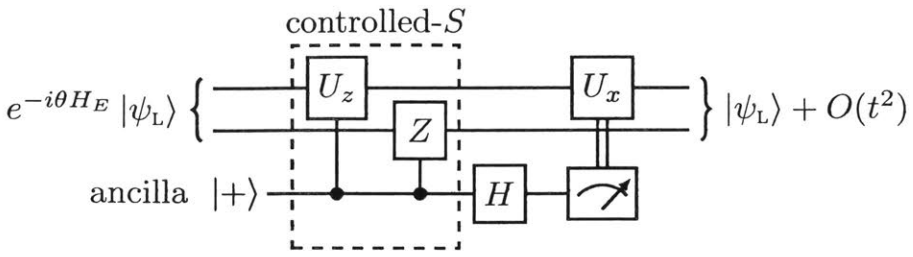

Figure 4-2: A recovery procedure for $n = 2$ qubits where $|\psi_L\rangle = \alpha|0_L\rangle + \beta|1_L\rangle$ for arbitrary α and β, H denotes a Hadamard gate, and ϑ is a random variable. The unitaries U_x and U_z are both π rotations about orthogonal axes on the Bloch sphere which are determined by g_1, g_2 and ϑ.

g_1, g_2 and ϑ. This means that the controlled-S (cS) operation used to measure the error syndrome can be implemented through a pair of two-qubit operations (cU_z and cZ), rather than a more challenging 3-qubit operation. If an error is detected, it can be corrected by applying $U_x := |\chi_0\rangle\langle\chi_1| + |\chi_1\rangle\langle\chi_0|$ to qubit 1—a π rotation about a different axis. (Both U_x and U_z could be synthesized out of a constant number of Pauli rotations, or implemented directly, e.g., by driving qubit 1 off resonance [143].) The full recovery procedure, which corrects CFD to leading order, is shown in Fig. 4-2. Note that S behaves like a stabilizer, in the sense of its action on $\mathcal{C}_0$ and $\mathcal{C}_1$. It does not, however, fit in the usual QEC stabilizer formalism since $\{H_E, S\} \neq 0$ generically, because $\{H_E, S\}|\psi\rangle = 0$ for $|\psi\rangle \in \mathcal{C}_0$ but not for $|\psi\rangle \in \mathcal{C}_1$ [89]. This is because H_E maps $\mathcal{C}_0$ to $\mathcal{C}_1$ without distortion, but not vice-versa, as H_E is not generically in the Pauli group. (Neither is S.) In spite of these unusual features, the procedure for feeding back on S in Fig. 4-2 is largely the same as that of the usual stabilizer formalism. Finally, (i) the encoding can be realized by applying a $c_2(U_x)_1$ gate to an initial state $|\chi_0\rangle|\psi\rangle$, and (ii) there is a simple way to implement any logical unitary U_L in this code: apply the corresponding physical U to qubit 2 followed by a recovery.

The logical states derived above are also valid for all $q > 1$ (i.e., $n > 2$ qubits), but the corresponding recovery and logical operations are generally more involved. Generically, the analogues of S in (4.13) are not separable for any choice of ϑ_j and φ_j [4].

[4]e.g., $S_1 = P_L + P_{E1} - P_{E2} - P_{E3}$ and $S_2 = P_L - P_{E1} + P_{E2} - P_{E3}$, which could be measured sequentially to identify an error for $n = 3$

One might still synthesize them with one- and two-qubit operations, perform phase kickback through optimal control, or implement a QEC recovery via more general channel-engineering techniques [115, 60, 132, 186]. More efficient solutions could even be found by analyzing specific experimental scenarios. One approach could be for example to use devices with $\{g_j\}$ chosen so that the recovery and logical operations can be conveniently implemented. One could also correct to a slightly lower order q [i.e., maintaining $n = O(\log q)$ but not saturating the ceiling in Eq. (4.3)]; this would yield a continuous family of possible $\vec{z}$'s [cf. Eq. (4.8)], among which one might find codes with convenient QEC operations. Note finally that for $n > 2$ it is not the bare H_E^m's that map the codespace to the orthogonal subspaces $\{\mathcal{C}_i\}_{i\geq 1}$, but rather linear combinations of them.

4.5 NV Quantum Register Implementations

Now we consider experimental implementation of the hardware-efficient QEC protocol on the quantum register in diamond. As assumed in the Hamiltonian (Eq. 4.1, 4.2), the dominant decoherence source for nuclear spins in a diamond quantum register is pure dephasing induced by a common fluctuator via the hyperfine interaction $\sum_{j=1}^{n} g_j Z_j$. However, we also see from Chapter. 2 and Appendix. D.3 that spatially randomly distributed ^{13}C 's have two hyperfine interaction terms with NV electron, the $S_z I_z$ term ($A_\parallel = g$) corresponding to pure dephasing, satisfying this model, but also a $S_z I_x$ term ($A_\perp$), which causes T_1 type of decoherence that violates the model. The hardware-efficient QEC code does not correct decoherence induced by $A_\perp$. It is critical to work in experimental conditions where decoherence is dephasing dominant and contribution from $A_\perp$ is small.

The previous chapters have shown it is experimentally convenient to work around 500 G of the NV excited-state level anticrossing, when the 532 nm laser illumination polarizes both NV and ^{14}N nuclear spin. Under this experimental condition, for most ^{13}C nuclear spins in the quantum register, $\omega_L \gg A_\parallel, A_\perp$. This guarantees that the decoherence is predominantly dephasing, as seen from the nuclear spin Hamiltonian

(Eq. 2.8):

$$\mathcal{H}_n = \omega_L I_z + A_\parallel S_z I_z + A_\perp S_z I_x. \tag{4.14}$$

We further explored the effect of $A_\perp$ by simulation, and found the QEC code works well for $A_\perp \sim< 10$ kHz. As an example, we take the NV examined in Chapter. 2 with DDRF, using parameters for ^{13}C A: $\{A_\parallel = -40.435 \text{ kHz}, A_\perp = 12 \text{ kHz}\}$, and ^{13}C D: $\{A_\parallel = 34.728 \text{ kHz}, A_\perp = 10 \text{ kHz}\}$, where $A_\perp$'s are estimated upper bound from the CPMG-32 spectrum (Fig. 2-10). The simulation shows negligible influence of $A_\perp$ on the QEC, which outperforms both physical qubits and the logical state without error correction (Fig. 4-3). In between QEC, we apply double quantum (DQ) dynamical decoupling (DD), which protects the nuclear spins from the NV, effectively decreasing the dephasing noise felt by ^{13}C . As shown in Chapter. 3, the DQ DD alone will improve the coherence time of nuclear spin. As a result, the single ^{13}C coherence improves from $1.5T_1^e$ (blue dash-dotted line). For this particular pair of ^{13}C 's, due to their similar hyperfine coupling strength, the logical state forms an approximate decoherence-free subspace (DFS) [38]. This results in better coherence time than the constituent physical qubits even without error correction (yellow dashed line). The approximate DFS state (also logical state) does not fully cancel out the dephasing noise, due to different $A_\parallel$ strength, indicated by the decay. By applying QEC on the logical state, we further cancel out the remaining dephasing noise, yielding a long-lived logical qubit (Fig. 4-3).

Although the requirements on $A_\perp$ strength of the probabilistically occuring ^{13}C 's seem daunting, we show in Appendix. D these ^{13}C 's are quite common considering ^{13}C 's with a hyperfine interaction $A_\parallel > 20$ kHz, which are resolvable at room-temperature by DDRF as shown in Chapter. 2. In fact, in a typical 1.1% natural abundance diamond lattice, roughly 60% of NVs have at least 2 suitable ^{13}C 's whose $A_\perp \sim< 10$ kHz, ready for hardware-efficient QEC experiments.

In the following chapter, we will demonstrate the necessary experimental tools that build up the QEC experiment.

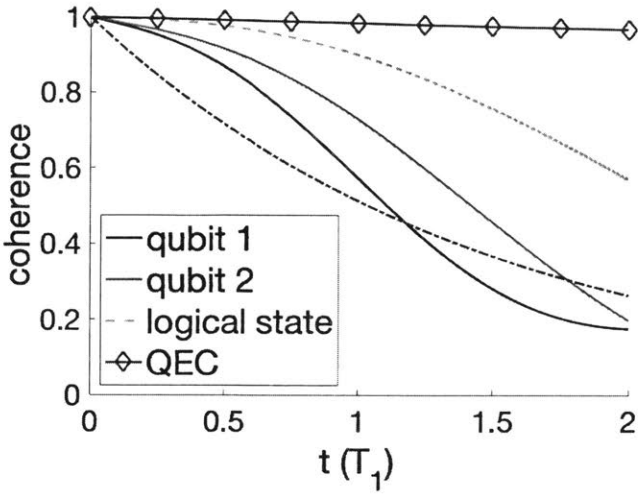

Figure 4-3: Simulation of QEC performance using parameters of ^{13}C A, D characterized before. We assume: $T_1^e = 4$ ms, the interpulse delay of DQ DD when not performing error correction is 5 μs, and error correction is done in 1 ms steps. The blue dash-dotted line indicates bare nuclear spin coherence time limited by NV fluctuation.

4.6 Discussion and Outlook

These noise-adapted QEC codes involve a trade-off: they correct CFD very efficiently at the cost of leaving most other errors uncorrected. For instance, errors during gates, due to miscalibration of g_j's, or from decoherence beyond CFD will generally affect the logical state [1]. Accordingly, these codes are manifestly not fault-tolerant in their current form [158]. They could potentially be made fault-tolerant using implementation-specific methods as in Ref. [177]. Crucially though, they offer such a large error budget under strong CFD—as evidenced by the gaps between QEC codes and physical qubits in Fig. 4-1—that this trade-off can easily be worthwhile, much like the targeted correction of photon loss in [160]. In the long-term, fault-tolerance could also be achieved through concatenation, using our noise-adapted codes at the lowest level of encoding to protect against the dominant error source, and more conventional codes at higher levels. Even more importantly, our codes could have a near-term impact in applications such as quantum sensing and communication, where long-lived quantum memories are useful even when they are not fault-tolerant. We emphasize, however, that these codes are designed expressly for small- and medium-scale qubit

registers, and that the exponential reduction in overhead should be understood to apply only in such devices. For one, there is typically a maximum n above which CFD no longer dominates. Also, while the error budget always increases with n in principle, so too do the effects of gate errors, miscalibration of g_j's and decoherence beyond CFD, as more qubits introduce more error channels. This growing sensitivity suggests an unconventional quantum sensing scheme to measure $\{g_j\}$ for large n, by variationally adjusting one's estimates to maximize code performance. In the nearer term, however, these imperfections will likely set a maximum n in any particular device beyond which one achieves no further gains, depending on their relative importance compared to CFD [1].

The QEC codes presented could be generalized in several ways. First, they can readily be made to correct dephasing due to multiple common fluctuators given enough qubits, at the cost of correcting to lower order in t. Similarly, they can correct spatially-correlated phase noise beyond that arising from common fluctuators. For instance, classical white noise in the energy gaps of register qubits leads to Lindblad error operators $L_j = \sqrt{\lambda_j}\,\vec{c}_j \cdot (Z_1, \ldots, Z_n)$, where $\{\sqrt{\lambda_j}\,\vec{c}_j\}$ describes the noise's normal modes [122]. In the limit of spatially uncorrelated noise the L_j's become Pauli Z operators; however, correlated noise produces L_j's with unequal amplitudes $\sqrt{\lambda_j}$. When the noise correlations are appreciable, it could be advantageous to use a QEC code that corrects the stronger noise modes (those with large λ_j's) to higher order in t than the weaker ones (smaller λ_j's) through an appropriate choice of V. It may also be possible to extend the codes presented here for the setting where a fluctuator's state affects not only the energy gap of each qubit, but also the direction of its Hamiltonian (i.e., its quantization axis) [7]. Eigenstate-preserving coupling arises frequently in practice because a large detuning between a weakly-coupled qubit and fluctuator suppresses non-commuting parts of their interaction Hamiltonian. However, when the coupling to the fluctuator is comparable to the internal Hamiltonian, such as for nuclear spins near defects in diamond, there can remain significant non-commuting terms leading to $H_E \sim \sum_j \vec{g}_j \cdot \vec{\sigma}_j$ in Eq. (4.2). We analyze this effect's impact on code performance in [1]. Extending the codes introduced here to this more general

setting would make them even more widely applicable to near-term experiments, but at the cost of larger overheads, since they would need to contend with a substantially larger space of possible errors. It may be more practical instead to suppress non-commuting interaction terms at the hardware level by increasing the energy gaps ω_j of the register qubits, or at the "software" level through concatenation [1]. Another interesting generalization would be to efficiently encode $k > 1$ logical qubits, which seems plausible based on the counting argument used throughout involving the dimension of $\mathcal{H}$ versus $\mathcal{E}$. Finally, it would be interesting to use the tools presented here to design codes for other common error sources, such as other types of decoherence or control/measurement errors.

Our results demonstrate that it is possible to find noise-adapted QEC codes with a well-defined advantage (here exponential) over known, general codes. It is commonly argued that QEC will be of little use in Noisy Intermediate-Scale Quantum (NISQ) devices due to its prohibitive overhead [167]. Noise-adapted QEC codes are a promising way to reduce this overhead, although to date they have mostly relied on numerical and variational techniques that lack transparency in terms of what advantage the codes can offer, and when [171, 81, 120, 202, 111] (see also [128] Ch. 13 and [159]). In contrast, the codes introduced here exhibit a clear reduction in overhead under a well-characterized and common type of noise. New QEC codes of this type could provide a middle ground between small-scale uncorrected devices and large-scale fault-tolerant ones, where the dominant decoherence mechanisms are tamed through specialized codes with only modest overheads. This view of near-term QEC as quantum "firmware" rather than "software" suggests a possible interplay between theory and experiment, whereby NISQ hardware and efficient QEC codes both guide each other's development.

Chapter 5

Hardware-Efficient Quantum Error Correction for Dephasing Induced by a Common Fluctuator: Developing Experimental Tools

In previous chapters, applying the philosophy of being hardware-efficient to our quantum register in diamond, we started by precise characterization of the system Hamiltonian, emphasizing on the energy non-conserving off-diagonal terms in the hyperfine coupling. With knowledge of the system Hamiltonian, we developed a semiclassical spin-fluctuator model to describe the decoherence of nuclear spins, and used the native ^{14}N as an example to experimentally verify the model. This model generalizes also to ^{13}C 's in the quantum register. When the $A_\perp$ terms are small for ^{13}C 's, their decoherence is predominantly dephasing due to a common fluctuator. Taking advantage of this knowledge, we have developed a hardware-efficient QEC code for common fluctuator dephasing (CFD), that offers an exponential reduction in overhead compared to the usual repetition code and is robust against model imperfections. The substantial gains in error suppression and reduction in overhead provide an opportunity to realize useful QEC in the diamond quantum register at room temperature.

In this chapter, we focus on the QEC code that encodes one logical qubit on two physical qubits, and develop experimental tools required for implementing this code. These include open loop dynamical decoupling, and nuclear spin operations including state initialization, control and tomography, which consists of building blocks of DDRF gates introduced in Chapter. 2. Using these tools, we demonstrate high-fidelity preparation of the basis logical states $|0_L\rangle, |1_L\rangle$.

5.1 Double Quantum Dynamical Decoupling

The first tool is double quantum (DQ) dynamical decoupling (DD), applied in between QEC recovery operations to mitigate the accumulation of dephasing errors induced by the common fluctuator. Because the timescale of nuclear spin coherence is the same as T_1^e of NV electron, it is necessary to consider all three levels of the electronic spin-1 fluctuator NV, and apply decoupling sequences between the $|m_s = +1\rangle$ and $|m_s = -1\rangle$ states (therefore double quantum) as discussed in Chapter. 3 and ref. [43]. The DQ transition is intrinsically forbidden by the transition rules, but could be implemented in experiment in two ways: composite pulse [103, 210] or two-tone microwave (MW) driving [151, 139]. In the former, a single DQ π pulse consists of three alternating $+1$ and -1 single quantum (SQ) π pulses [103, 210]. It is simple but the pulse is slow. Given the total MW power $\propto B_x^2$, each pulse takes $\propto \sqrt{2}\pi/B_x$ and the composite DQ π pulse takes $\propto 3\sqrt{2}\pi/B_x$. In the latter approach, a two-tone MW $B_1\cos(\omega_1 t + \delta_1) + B_2\cos(\omega_2 t + \delta_2)$ is generated to drive the ± 1 electron transitions simultaneously. The Hamiltonian in the rotating frame after dropping out the fast oscillating terms is:

$$\mathcal{H} = \begin{pmatrix} \Delta + \gamma_e B_z - \omega_1 & \frac{\gamma_e B_1 e^{-i\delta_1}}{2\sqrt{2}} & 0 \\ \frac{\gamma_e B_1 e^{i\delta_1}}{2\sqrt{2}} & 0 & \frac{\gamma_e B_2 e^{i\delta_2}}{2\sqrt{2}} \\ 0 & \frac{\gamma_e B_2 e^{-i\delta_2}}{2\sqrt{2}} & \Delta - \gamma_e B_z - \omega_2 \end{pmatrix}, \tag{5.1}$$

where $\Delta, \gamma_e B_z$ are the zero-field splitting and Zeeman splitting of NV. By having both frequencies on resonance with the NV ± 1 transitions, and tuning the driving

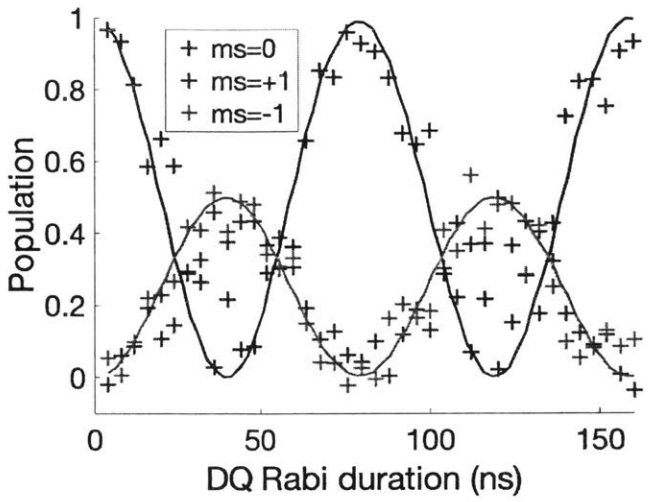

Figure 5-1: Two-tone microwave driving of the NV electronic spin starting from $|m_s = 0\rangle$. After a varied two-tone driving duration, each of the three spin states $|m_s = 0, \pm 1\rangle$ is mapped to the $|m_s = 0\rangle$ state by an optional π pulse and optically read out.

amplitude the same $B_1 = B_2$, the Hamiltonian becomes a spin-1 Pauli X operator that could drive the NV directly between $|m_s = \pm 1\rangle$ [151, 139]. Considering the same MW power split evenly between the two-tone $B_x^2 = B_1^2 + B_2^2$, the two-tone DQ π pulse takes $\propto 2\sqrt{2}\pi/B_x$, faster than the composite pulse. As a demonstration, we varied the two-tone pulse duration, and read out the remaining population in all three NV electronic spin state. The result is shown in Fig. 5-1, and we observe fast and high-fidelity control.

5.2 Nuclear Spin State Preparation and Measurement

In Chapter. 2 we have identified individual ^{13}C 's and demonstrated quantum control with unpolarized nuclear spins using both indirect and direct control techniques. Here we focus on the direct control method using DDRF sequence, which allows access to ^{13}C 's with small $A_\perp$ hyperfine terms. To realize the conditional and unconditional nuclear spin rotations via the DDRF sequence, a few tens of pulses have to be

considered. This has been analyzed and experimental demonstrated in the previous chapter. However, for more complicated nuclear spin operations that require multiple rotations, it is not convenient to work at the MW and RF pulse level which directly interface the physical qubits. Instead, we could now use the DDRF sequence as a single building block and subroutine, and abstract ourselves away from the physical realization of pulses. This way we focus on quantum circuits at a higher level. We next demonstrate a fundamental and indispensable part of QEC–state preparation and measurement (SPAM) of individual nuclear spins.

5.2.1 Quantum Circuits for SPAM

Since we cannot directly initialize and read out nuclear spins, SPAM operations are achieved with the help of the NV electron. To initialize the nuclear spin, we first polarize the NV electron through laser illumination, then transfer polarization from the NV electron to the target ^{13}C nuclear spin, and finally repolarize the NV by a short laser pulse without disturbing the nuclear spin (Fig. 5-2(a)). This operation maps NV $|0/1\rangle$ to the ^{13}C nuclear spin $|0/1\rangle$ state.

To fully characterize the nuclear spin state, we need the ability to perform nuclear spin state tomography. This is achieved by mapping the corresponding expectation values of each Pauli operators $\langle X\rangle(\langle Y\rangle, \langle Z\rangle)$ onto the NV electron for optical readout. The nuclear spin state density operator could be reconstructed by combining the three measurements $\rho^{\text{expt}} = \frac{1}{2}(\mathbb{1} + \langle X\rangle\sigma_x + \langle Y\rangle\sigma_y + \langle Z\rangle\sigma_z)$. The three mapping circuits for quantum state tomography are listed in Fig. 5-2(b-c).

5.2.2 Experiment

We demonstrate our capabilities of the SPAM operations via the nuclear Ramsey experiment on both ^{13}C A and D. The subroutine of $\text{CR}_\vartheta(\frac{\pi}{2})$ gate is calibrated using nuclear Rabi nutation shown in Chapter. 2. Building upon the $\text{CR}_\vartheta(\frac{\pi}{2})$ gate, we construct the quantum circuits utilizing nuclear spin SPAM gates (Fig. 5-3(a)). We firstly initialize the nuclear spin, prepare it in an equal superposition state by a CR

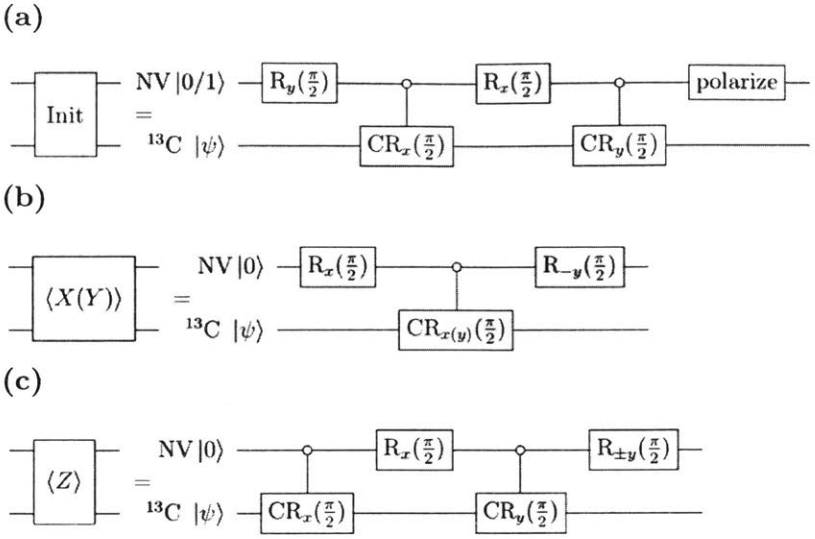

Figure 5-2: Quantum circuits for state preparation and measurement. (a) Initialization sequence. The polarization is transferred from NV to the ^{13}C , and then the NV electron is repolarized. (b-c) Nuclear spin state tomography. The expectation values of Pauli X, Y, Z are mapped to the NV electron for optical readout. The last NV rotation for $\langle Y\rangle, \langle Z\rangle$ depends on the definition of nuclear spin $|0/1\rangle$ state, which should yield $g_1 > 0$ for the hardware-efficient QEC.

gate, and let it evolve. The nuclear spin accumulates a phase during the Ramsey free precession, which is subsequently read out by state tomography measurements for $\langle X\rangle, \langle Y\rangle, \langle Z\rangle$. The results are plotted in Fig. 5-3(c, e) for ^{13}C A and D, respectively. The experiments are consistent with theory, confirming our high-level control of the nuclear spin including state initialization and tomography.

Next, we verify the conditional and unconditional nuclear spin control. In the previous nuclear Ramsey experiment, we insert an optional MW π pulse that prepares NV in $|0/1\rangle$ [1] immediately after nuclear spin initialization (Fig. 5-3(a)). Consequently, due to the NV dependent nuclear spin $\mathrm{CR}_x(\frac{\pi}{2})$ gate, the Ramsey experiment measures free evolution from the nuclear spin $\frac{1}{\sqrt{2}}(|0\rangle \pm i\,|1\rangle)$ state, manifesting opposite phase in the $\langle X\rangle$ oscillation. This is consistent with our measurements, shown as crimson and gray curves for ^{13}C A and D in Fig. 5-3(d, f), further confirming the nuclear spin gate is conditional on NV. In comparison, we replace the conditional nuclear spin

[1] Because the nuclear spin is read out via the NV, a corresponding π pulse on NV is required before the readout for correct interpretation. Here we apply the second π pulse before the nuclear spin free precession to ensure the nuclear spins have the same free precession rate to avoid misinterpretation.

gate $\mathrm{CR}_x(\frac{\pi}{2})$ by an unconditional nuclear spin $\frac{\pi}{2}$ rotation (Fig. 5-3(b)) and perform Ramsey experiment. The nuclear spin is prepared in $\frac{1}{\sqrt{2}}(|0\rangle + i\,|1\rangle)$ regardless of the NV electronic spin state. Experimental result is shown as black curve in the same figure as the conditional gate (Fig. 5-3(d, f)). Recall our DDRF CR gate is controlled by $|m_s = 0\rangle$. The agreement between Ramsey curves with CR gate when NV starts in $|1\rangle$ and with unconditional gate when NV starts in $|0\rangle$ confirms the nuclear spin rotation is unconditional in the latter case. The unconditional single nuclear spin rotation and conditional two-qubit gate between the nuclear spin and NV form a complete set for universal control.

5.2.3 Discussion

There are various factors that contribute to the reduced contrast in experiments shown in Fig. 5-3. Some are intrinsic to our measurement protocol caused by the imperfect polarization of NV electron [203], some are due to control pulse errors and decoherence during the quantum gates. These can be in principle calibrated. A discussion on the imperfect NV polarization is included in Chapter. 6. Calibration of control errors are discussed for example in [56]. In experiment, we observed asymmetry between $\langle \pm\sigma \rangle$ measurements, indicating miscalibrated controls. In the following section, we avoid potential bias due to the measurement asymmetry by performing differential readout. For every measurement, we perform the same experiment with an additional MW π pulse right before the readout. The difference between these two signals are used.

So far we have demonstrated the ability to isolate and address individual nuclear spins and perform both unconditional and conditional nuclear spin rotations, which form a universal set of control (Chapter. 2). Building upon these building blocks, we demonstrated higher-level controls that initialize the nuclear spin by polarization transfer from NV electron, and measure expectation values of all Pauli operators to perform state tomography. We will now employ all these machinery of quantum control towards operations required for preparing logical states and performing QEC recovery.

5.3 Control for Logical State Preparation and QEC Recovery

Recall the logical states are

$$\begin{aligned} |0_L\rangle &= |\chi_0\rangle |0\rangle , \\ |1_L\rangle &= |\chi_1\rangle |1\rangle . \end{aligned} \tag{5.2}$$

To avoid the expensive nuclear-nuclear spin gate, we would like to prepare any logical superposition state $c_0 |0_L\rangle + c_1 |1_L\rangle$ utilizing the quantum circuit shown in Fig. 5-4. We start with the two ^{13}C nuclear spins prepared in $|\chi_1\rangle$ and $|0\rangle$ respectively, and the NV prepared in the target state $c_0 |0\rangle + c_1 |1\rangle$. Subsequent Controlled-$U_x$ and C_eNOT_n (e means NV electron and n means nuclear spin qubit) gates then entangle NV and the nuclear spin qubits, creating a tripartite entangled state. Finally a C_nNOT_e gate is applied on NV to disentangle NV from the logical qubit, completing the logical state preparation. The initialization of nuclear spins to $|0\rangle$ has been shown in the previous section. The controlled-X or CNOT gate can be decomposed into

$$\text{CNOT} = \text{CR}_x(-\frac{\pi}{2})\text{R}_x(\frac{\pi}{2}), \tag{5.3}$$

whose components have been demonstrated before. The remainings parts are preparation of $|\chi_1\rangle$, realization of U_x gate and C_nNOT_e on NV. In the following, we first focus on the preparation and characterization of state $|\chi_1\rangle$, then construct controls required for QEC recovery: U_y, U_z, which are equivalent to Pauli Y and Z operators in the $\{\chi_0, \chi_1\}$ basis up to a global phase. They can combine to realize U_x operator. With all these tools, we are in a good position to demonstrate the preparation of logical basis states at the end.

5.3.1 Preparation of $|\chi_1\rangle$

Provided the capabilities to initialize, control and measure single nuclear spins, we move on towards the logical state preparation. Eq. 5.2 defines the logical states.

The two nuclear spins of choice are ^{13}C A, D, which show small $A_\perp$ hyperfine coupling strength. From DDRF characterization, $g_1 = -A_{\parallel,A} = 40435$ Hz, $g_2 = A_{\parallel,D} = 34728$ Hz. Plugging into Eq. 4.11, and using $\vartheta_0 = \varphi_1 = 0, \vartheta_2 = -\varphi_3 = \frac{\pi}{2}$,

$$\begin{aligned} |\chi_0\rangle &= c\Big(\sqrt{|g_1 - g_2|}\ |0\rangle - i\sqrt{|g_1 + g_2|}\ |1\rangle\Big) \\ |\chi_1\rangle &= c\Big(\sqrt{|g_1 + g_2|}\ |0\rangle + i\sqrt{|g_1 - g_2|}\ |1\rangle\Big) \end{aligned} \tag{5.4}$$

These are the basis states for ^{13}C A in our hardware-efficient QEC. They are rotated from the computational states $|0/1\rangle$ by $\varphi = 33°$, where $\tan\frac{\varphi}{2} = \sqrt{\frac{g_1-g_2}{g_1+g_2}}$. Shown in Fig. 5-5, $|\chi_1\rangle$ is close to $|0\rangle$, and we demonstrate its preparation first. We follow the quantum circuit shown in Fig. 5-6(a), with ^{13}C A initialized in $|0\rangle$. A conditional nuclear spin rotation $\mathrm{CR}_{-x}(\varphi)$ brings it to $|\chi_1\rangle$. This is achieved by a DDRF sequence, with $N = 4$ along $-x$ axis. We then perform quantum state tomography to characterize the prepared state, and obtain a fidelity $\mathcal{F}_{\chi_1} = \left[\mathrm{tr}(\sqrt{\rho^{\mathrm{expt}}}\rho^{\mathrm{target}}\sqrt{\rho^{\mathrm{expt}}})\right]^2 =$ 76(3)% (Fig. 5-8(a)).

5.3.2 Realization of U_y operator

To prepare $|\chi_0\rangle$, we start from $|\chi_1\rangle$, and apply $\mathrm{U}_y = |\chi_1\rangle\langle\chi_0| - |\chi_0\rangle\langle\chi_1|$. This is the equivalent of Pauli Y operator in the $\{|\chi_0\rangle, |\chi_1\rangle\}$ basis up to a global phase. Conveniently, the desired control is implemented by

$$\mathrm{U}_y = |\chi_1\rangle\langle\chi_0| - |\chi_0\rangle\langle\chi_1| = \mathrm{R}_x(\pi), \tag{5.5}$$

realized by a single DDRF gate (Fig. 5-7(a)). Utilizing the optional π phase shift in DDRF gate, we can change the rotation into $\mathrm{CR}_x(\pi)$ and obtain NV controlled CU_y gate. This gate is useful both for state preparation as we demonstrate here in Fig. 5-6(b) and for recovery in QEC. To be consistent with logical superposition state

preparation following the quantum circuit in Fig. 5-4, we use the CU_y gate to prepare $|\chi_0\rangle$ from $|\chi_1\rangle$ and obtain $\mathcal{F}_{\chi_0} = 73(3)\%$, shown in Fig. 5-8(b).

As we have briefly discussed in the nuclear Ramsey experiment, the fidelities of state tomography are mainly limited by the imperfect polarization of NV electron. The imperfect NV polarization is first transferred to the nuclear spin for initialization and then mapped back for readout. A more detailed discussed is included in Chapter. 6. Here, without precise knolwedge of the charged state dynamics or a systematic benchmarking of the nuclear spin control, we cannot remove only effects from imperfect NV polarization. Instead, we calibrate our results for both initialization and readout errors. This is achieved by renormalizing all experimental measurements by the experimental $\langle Z \rangle$ measurement of nuclear spin $|0\rangle$ state, in consistence with ref. [203]. The calibrated state tomography results are shown in Fig. 5-8(c,d) for $|\chi_1\rangle, |\chi_0\rangle$, with a calibrated fidelity of $\mathcal{F}_{\chi_1} = 96(3)\%$, $\mathcal{F}_{\chi_0} = 92(3)\%$.

5.3.3 Realization of U_z operator

Another operator necessary for the recovery operation in QEC is U_z, which is equivalent to Pauli Z operator in the $\{|\chi_0\rangle, |\chi_1\rangle\}$ basis (Chapter. 4). This could be achieved by a detuned DDRF gate directly, which is briefly discussed in Chapter. 2. However, a detuned gate on nuclear spin is challenging for calibration purposes. To sidestep this issue, we decompose the U_z gate into well-calibrated operations as shown in Fig. 5-7(b). In particular

$$U_z = R_x(\varphi)R_z(\pi)R_x(-\varphi). \tag{5.6}$$

The φ rotation is already demonstrated in preparation of $|\chi_1\rangle$ state. The R_z rotation could be embedded into a simulated frame rotation in all following nuclear spin operators, imposing no control infidelities or time cost. Alternatively, we can interpret the $R_z(\pi)$ operation in the original frame: we redefine the states adaptively as the

QEC experiment is undergoing,

$$
\begin{aligned}
|\chi_0\rangle &= c\Big(\sqrt{|g_1 - g_2|}\ |0\rangle + (-1)^{n+1} i \sqrt{|g_1 + g_2|}\ |1\rangle\Big), \\
|\chi_1\rangle &= c\Big(\sqrt{|g_1 + g_2|}\ |0\rangle + (-1)^{n} i \sqrt{|g_1 - g_2|}\ |1\rangle\Big),
\end{aligned}
\tag{5.7}
$$

where n is the total number of U_z operator implemented so far. Either way, the $R_z(\pi)$ is achieved on the software level and does not impose any experimental overhead. The U_z operator is therefore equivalent to $R_x(-2\varphi)$ in experiment. Care has to be taken for simulated rotations such as R_z, especially when operated in controlled gates. A good practice is to analyze case-by-case to ensure effects of the simulated rotations are carried out.

As $U_{x,y,z}$ are correspondingly the Pauli operators in the $\{|\chi_0\rangle, |\chi_1\rangle\}$ basis, and we have shown $U_{y,z}$, it is straightforward to realize

$$
U_y U_z = i U_x = R_x(\pi - 2\varphi), \tag{5.8}
$$

with a simulated frame rotation.

5.3.4 Logical State Preparation and Measurement

Having laid the foundations, we demonstrate preparation of logical states and their characterization. First, we introduce measurements for two-qubit tomography. Like in the one qubit case, where we measured expectation values of Pauli operators $\langle X\rangle, \langle Y\rangle, \langle Z\rangle$ for the reconstruction of the qubit density operator, here we measure the expectation values of two-qubit Pauli operator $\langle \sigma_1 \sigma_2 \rangle$. This measurement can be achieved via the general circuit shown in Fig. 5-9(a). For our experimental realizations using the building blocks of DDRF sequences, the quantum circuits are shown in Fig. 5-9(b-f). Here we only show five measurement operators which are relevant to non-zero components of the $|0_L\rangle$, $|1_L\rangle$ states.

We then prepare the logical states using circuits shown in Fig. 5-10. The tomography of raw data is shown in Fig. 5-11(a,b), giving logical state fidelities of

$\mathcal{F}_{0_L} = 54(9)\%$, $\mathcal{F}_{1_L} = 52(9)\%$. Similar to the single nuclear spin state tomography, the fidelities from raw data are limited by the imperfect polarization of NV electron. With two nuclear spin qubits, the polarization transfer from NV happens twice, and the loss in contrast is therefore worse than before. We renormalize all two-qubit measurements by the result of performing $\langle ZZ \rangle$ measurement on $|00\rangle$ state, and obtain the calibrated state tomography shown in Fig. 5-11(c,d), with state fidelities $\mathcal{F}_{0_L} = 93(13)\%$, $\mathcal{F}_{1_L} = 95(14)\%$.

We remark that encoding quantum information generally requires superpositions of the logical basis states. It demands one more step from our demonstration here: decoupling NV from the logical qubit, indicated by the C_nNOT_e gate in Fig. 5-4. In Fig. 5-12 we show a SWAP gate between NV electron and one ^{13}C nuclear spin qubit, which guarantees universal control together with the qubit rotations we have thus far demonstrated. It is an overkill for state preparation. And given the overhead mainly comes from the DDRF gates, we should always optimize the quantum circuit by the DDRF gate count on a case-by-case basis, instead of always implementing the SWAP gate. For example the quantum circuit in Fig. 5-4 should have a better DDRF gate count by 2 compared to using SWAP.

5.4 Discussion and Conclusion

In this Chapter, we have developed all the experimental tools required by the hardware-efficient QEC protocol. We first show double quantum control between NV $|m_s = +1\rangle$ and $|m_s = -1\rangle$, which protects the nuclear spins in an open loop and mitigates their dephasing. We then focus on single nuclear spin qubit and demonstrate its state preparation, control and measurement. Using the DDRF gate as a single building block, we developed quantum circuits that enable the initialization and tomography measurement of the nuclear spin qubits. Running Ramsey sequence as an illustrative example, we experimentally demonstrated successful initialization, both conditional and unconditional control, and full tomography of the nuclear spin qubits. Next, we prepared both $|\chi_0\rangle$ and $|\chi_1\rangle$ states with high fidelities, and demonstrated ways to ap-

ply U_x, U_y and U_z operations which supplement the previous nuclear spin controls and form a complete control set for the QEC protocol introduced in Chapter. 4. Lastly, we showed state preparation and tomography of the logical basis states $|0_L\rangle, |1_L\rangle$ with high fidelities, opening up an avenue to encoding quantum information in the logical states protected against common fluctuator dephasing.

Combining all experimental tools developed in this chapter with the demonstrated high fidelities, it is possible in the near future to implement the hardware-efficient QEC protocol in experiment. In the next chapter, we will discuss remaining challenges and possible approaches to overcome these obstacles.

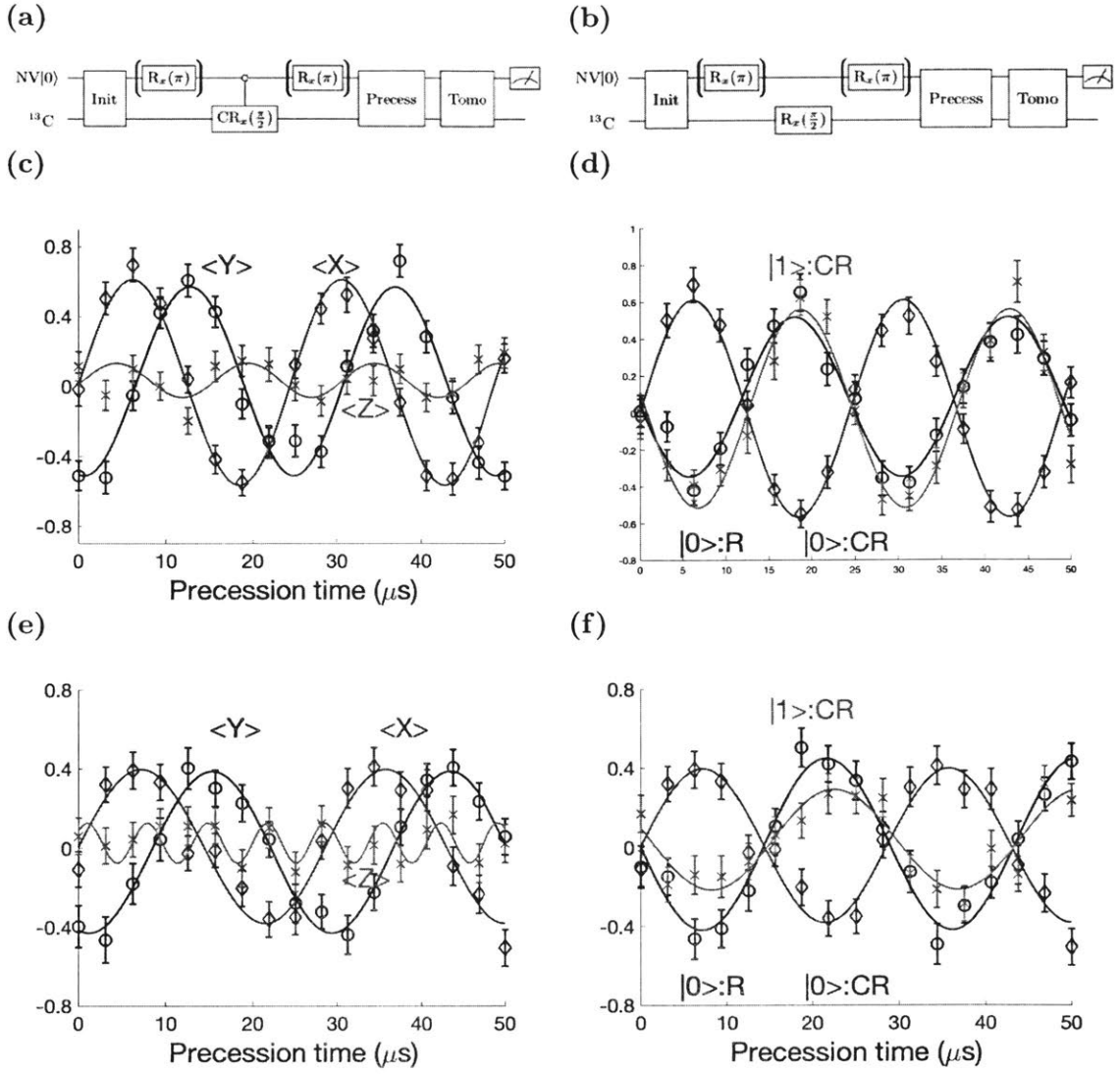

Figure 5-3: Verification of nuclear spin polarization, control and measurement. (a, b) Quantum circuit for nuclear spin Ramsey experiment. The nuclear spin is initialized (Init) and brought to a superposition state either by (a) conditional or (b) unconditional nuclear spin rotation. The last tomography (Tomo) gate is applied to measure $\langle X\rangle, \langle Y\rangle, \langle Z\rangle$. The Init and Tomo gates are broken down into basic control units in Fig. 5-2. (c, e) Nuclear Ramsey experiment on ^{13}C (c) A (e) D, using conditional nuclear spin rotation, with NV starting in $|0\rangle$ selecting the $R_{-x}(\frac{\pi}{2}$ rotation for Ramsey. (d, f) A comparison between conditional and unconditional rotations on ^{13}C (d) A (f) D. The crimson and gray curves are $\langle X\rangle$ measurements of nuclear Ramsey using conditional gate, with NV starting in $|0, 1\rangle$, applying $R_{\mp x}(\frac{\pi}{2})$ rotation to prepare the nuclear spin superposition state. The black curve uses unconditional gate, always applying $R_x(\frac{\pi}{2})$. This experiment starts with $|m_s = 0\rangle$.

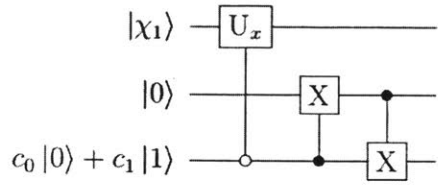

Figure 5-4: Quantum circuit to prepare logical state $c_0 |0_L\rangle + c_1 |1_L\rangle$. The three qubits from top to bottom are ^{13}C A, ^{13}C D, NV.

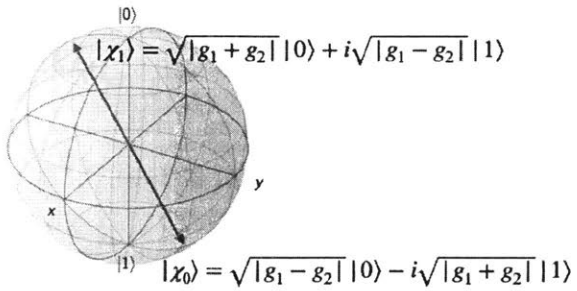

Figure 5-5: States $|\chi_0\rangle, |\chi_1\rangle$ represented on the Bloch sphere. Each is rotated from the $|1\rangle, |0\rangle$ state for 33° for our quantum register of interest.

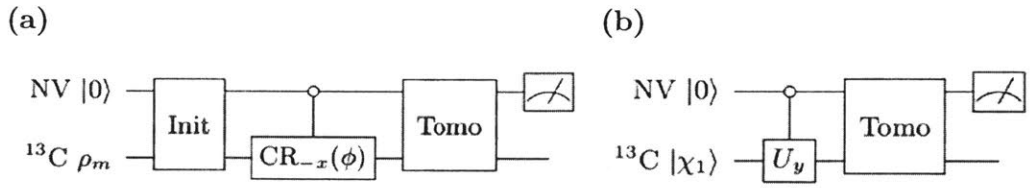

Figure 5-6: Quantum circuits for preparation of state (a) $|\chi_1\rangle$, (b) $|\chi_0\rangle$.

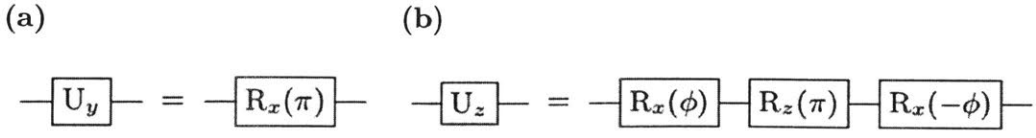

Figure 5-7: Quantum circuits for realizing operators (a) U_y, (b) U_z.

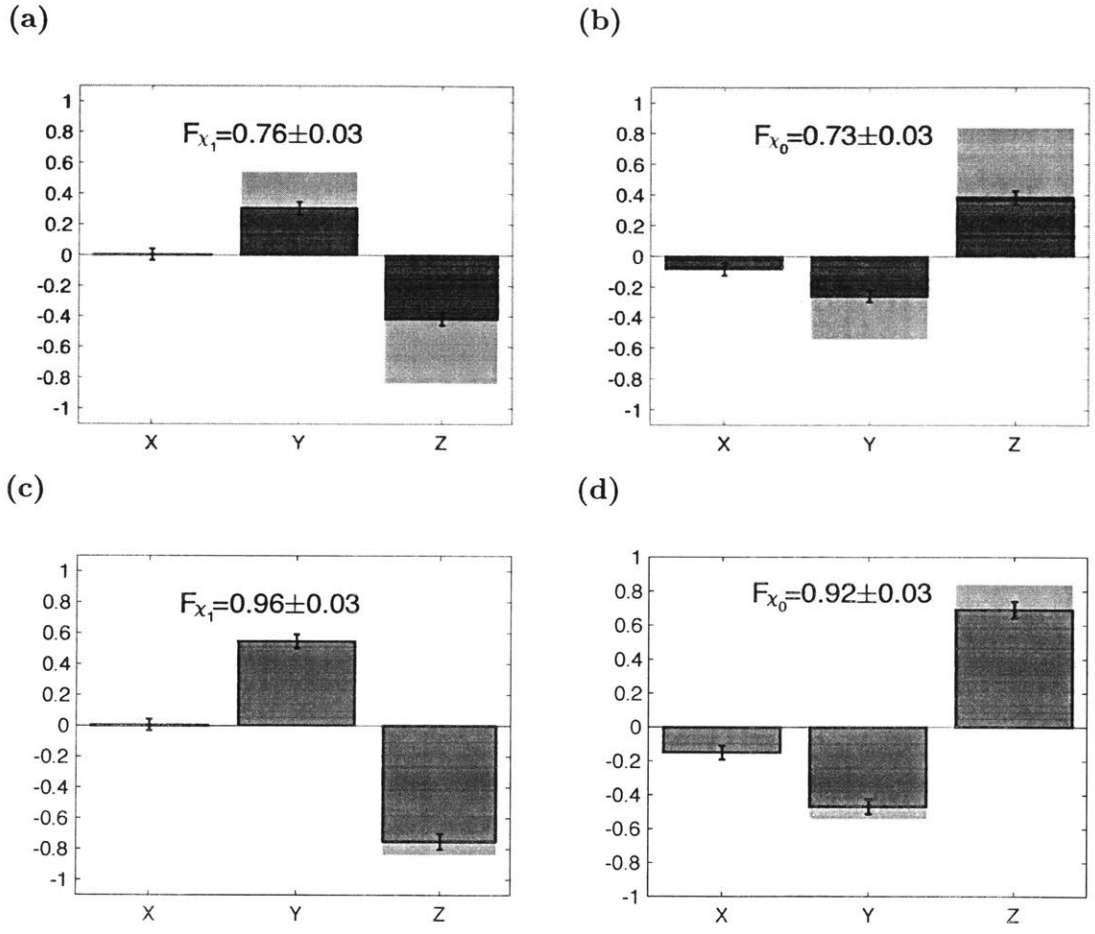

Figure 5-8: Tomography of (a, c) $|\chi_1\rangle$, (b, d) $|\chi_0\rangle$ state. The shaded gray area is theoretical value, and crimson (blue) is experimental result without (with) initialization and readout calibration.

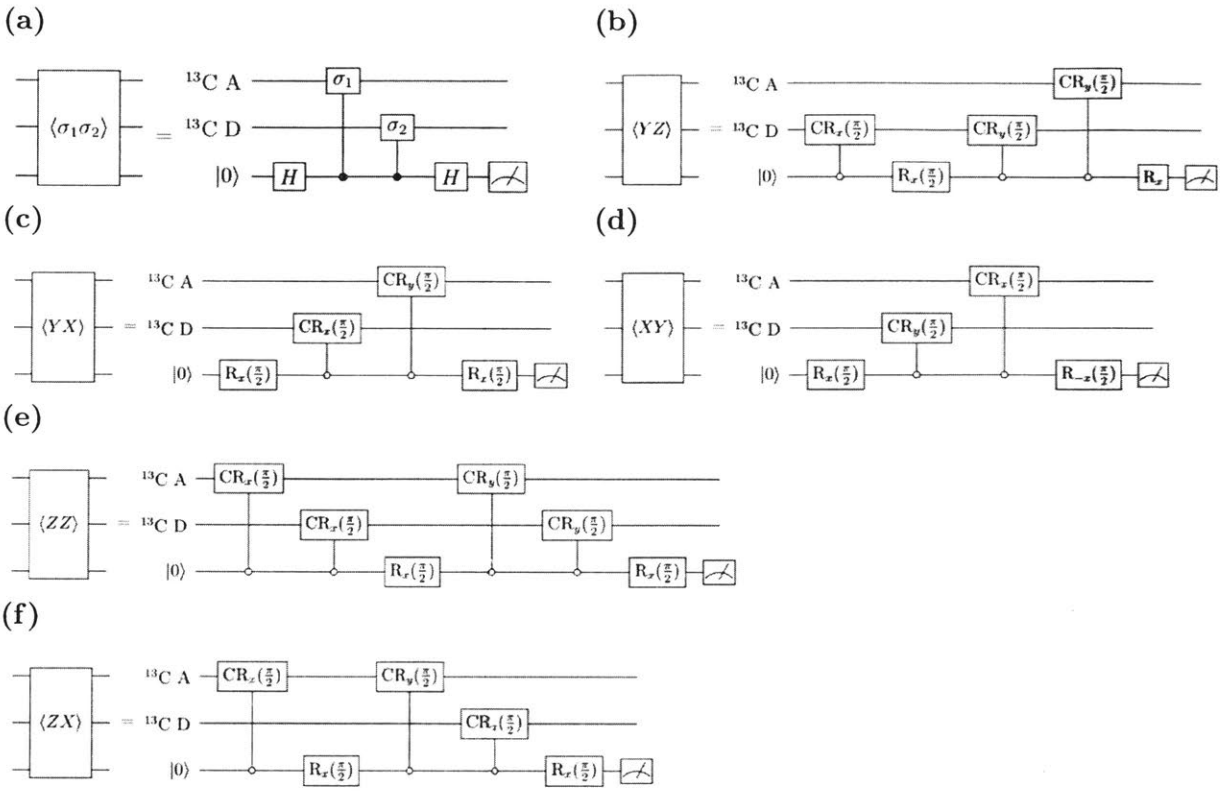

Figure 5-9: (a) General circuit for two-qubit measurement $\langle\sigma_1\sigma_2\rangle$. Quantum circuits used in experiments for measuring (b) $\langle YZ\rangle$, (c) $\langle YX\rangle$, (d) $\langle XY\rangle$, (e) $\langle ZZ\rangle$, (f) $\langle ZX\rangle$

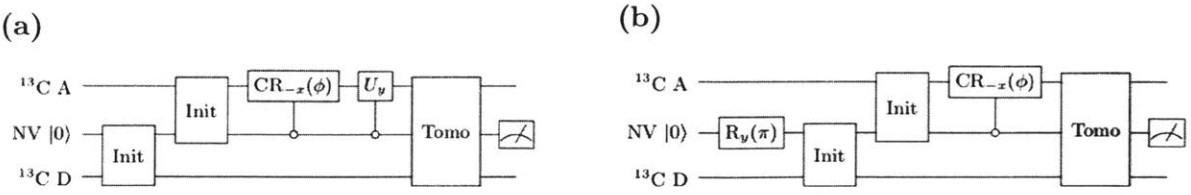

Figure 5-10: Quantum circuits for preparation of the logical basis states (a) $|0_L\rangle$, and (b) $|1_L\rangle$.

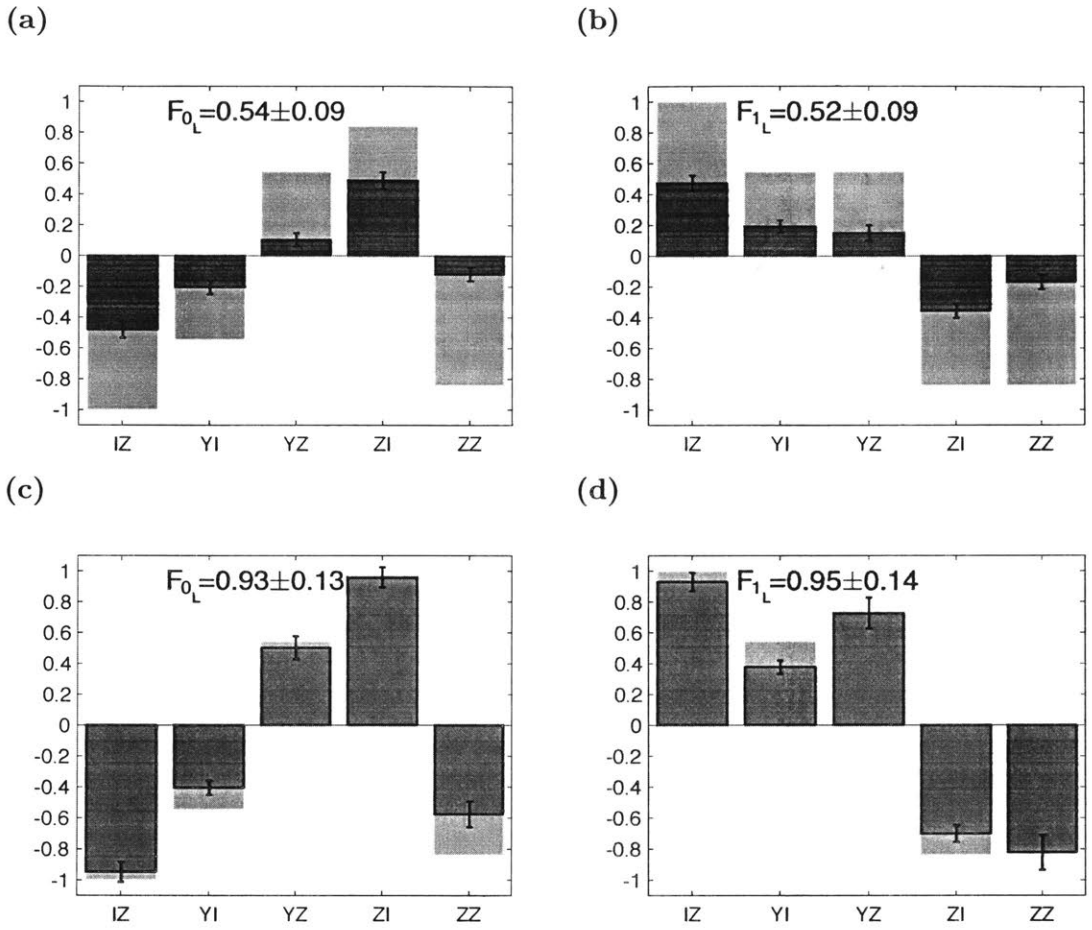

Figure 5-11: Tomography of (a, c) $|0_L\rangle$, (b, d) $|1_L\rangle$ state. The shaded gray area is theoretical value, and crimson (blue) is experimental result without (with) initialization and readout calibration.

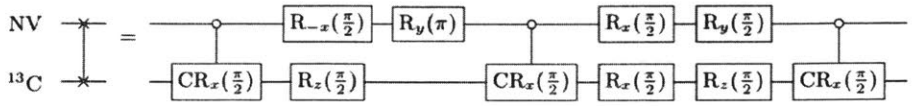

Figure 5-12: Quantum circuit for SWAP gate between NV and a ^{13}C nuclear spin qubit.

THIS PAGE INTENTIONALLY LEFT BLANK

Chapter 6

Discussion and Outlook: Implementation of Hardware-Efficient QEC

Equipped with all the experimental tools developed in Chapter. 5, we are in good shape to implement the hardware-efficient QEC code in our diamond quantum register. There are a few remaining challenges that we will discuss here. The most prominent one is to maintain a decent overall process fidelity, including the state preparation, QEC and measurement. The infidelity of measurement in a process that involves reinitialization of NV electron is intrinsic to the system and poses an ultimate limit to the process fidelity. Analysis and ways to calibrate it is discussed first. Next, a possibility of single-shot readout of individual ^{13}C is discussed, with the experimental sequence proposed. This could to a large extent suppress the infidelity caused by imperfect NV polarization. The remaining infidelities mainly come from the interplay between NV decoherence and control errors, which can be mitigated by incorporating DDRF with double quantum dynamical decoupling. None of the these are fundamental limits and near-term experimental demonstration of our hardware-efficient QEC code is promising.

6.1 Calibration for Nuclear Spin Readout Due to Imperfect NV Polarization

One challenge in QEC implementation is the loss in readout contrast due to reinitialization of NV. Under green laser illumination, the NV is not perfectly polarized. On the one hand, the decay rates from metastable state to all spin ground states are on the same order, resulting in non-zero populations in $|m_s = \pm 1\rangle$ state. On the other hand, there is roughly 30% chance NV ends up in NV^0 state [15, 45, 94]. Both scenarios add up and contribute to $\sim$ 70% NV polarization to $|m_s = 0\rangle$ [174, 207, 93]. A detailed description of the NV model under optical illumination is presented in Appendix. A. Taking an analysis approach similar to [203], we compare the differential signal $\Delta_f = S_f - \bar{S}_f$ between the fluorescence readout of the final state and the fluorescence readout of the final state followed by an immediate π pulse. This signal is normalized by the differential readout of the initialized state with and without a π pulse

$$C = \frac{S_f - \bar{S}_f}{S_i - \bar{S}_i}. \tag{6.1}$$

Assuming the π pulse for differential signal is perfect, then $-1 \leq C \leq 1$ and is symmetric.

We now consider a phenomenological representation of the imperfect polarization of NV

$$\rho_i = p_1\rho_0 + p_2\rho_m + p_3\rho_s + p_4\rho_c, \tag{6.2}$$

where ρ_0 is the desired $|m_s = 0\rangle$ state, ρ_m fully mixed state between $|m_s = 0, +1\rangle$, ρ_s the unused spin state $|m_s = -1\rangle$, and ρ_c the charged state NV^0. $p_1 + p_2 + p_3 + p_4 = 1$. Only p_1 contributes to differential readout signal. In a simple experiment without reinitialization of NV, it is obvious $C_{\max} = 1$.

In a more complicated experiment such as QEC, the NV electron goes through several reinitialization processes to polarize and later to measure the nuclear spins. The resulting successful rate and contrast of readout therefore depend on the details of the reinitialization process. As a simplified model, we consider that the reinitializa-

tion does not influence the nuclear spin state and fully redistribute the NV electron population. After polarization transfer from NV electron to the nuclear spin, we start from state

$$\rho = p_1\rho_m \otimes \rho_0 + p_2\rho_m \otimes \rho_m + p_3\rho_s \otimes \rho_m + p_4\rho_c \otimes \rho_m. \tag{6.3}$$

The reinitialization changes the state to

$$\rho = (p_1\rho_0 + p_2\rho_m + p_3\rho_s + p_4\rho_c) \otimes [p_1\rho_0 + (1-p_1)\rho_m] \tag{6.4}$$

Therefore the maximum contrast for nuclear spin measurement is

$$C_{\max} = \frac{p_1^2}{p_1} = p_1 \tag{6.5}$$

In another note, if the reinitialization process does not change the NV charged state, then instead of Eq. 6.4 we have

$$\rho = p_1\frac{p_1\rho_0 + p_2\rho_m + p_c\rho_s}{p_1+p_2+p_3} \otimes \rho_0 + (p_2+p_3)\frac{p_1\rho_0 + p_2\rho_m + p_c\rho_s}{p_1+p_2+p_3} \otimes \rho_m + p_4\rho_c \otimes \rho_m, \tag{6.6}$$

resulting in maximum contrast

$$C_{\max} = \frac{p_1}{p_1+p_2+p_3} > p_1 \tag{6.7}$$

NV charged state population is reported around 70% in literature [15, 45, 94], suggesting $C_{\max} \leq p_1 + p_2 + p_3 \approx 70\%$. This limits the contrast of two-qubit correlation measurements to $\sim 50\%$. We should therefore calibrate two-qubit readouts accordingly.

In experiments so far, we have no precise knowledge of p_1. Therefore, a calibration of the initialization and readout accounting only for the imperfect polarization of NV is not available. Instead, we have used the experimental measurement of $\langle Z\rangle, \langle ZZ\rangle$ of nuclear spin qubit states $|0\rangle$ and $|00\rangle$ to renormalize one- and two-qubit measurements. This is consistent with ref. [203], and works in practice given high control fidelity. However, the calibration still includes both contributions due to imperfect

NV polarization and due to control infidelities. It therefore over-compensates. One possible strategy to avoid over-compensation is to perform a systematic benchmarking of our nuclear spin control gates. Then we could decouple contributions from control infidelities and obtain effects due to imperfect NV polarization p_1. A possible strategy is the gate set tomography [146, 31, 64], which takes measurement into account. This could give us more faithful tomography measurements, though the contrast in one- and two-qubit measurements remains small, and long averaging is required. In addition, the benchmarking could provide useful information about sources of control infidelities, and improve our nuclear spin qubit control.

6.2 Repetitive Readout for Nuclear Spin

Another way to circumvent the readout issue due to imperfect NV polarization is by developing repetitive readout capability for ^{13}C . After analysis, we find the $\langle X \rangle$ readout operator $\mathrm{U}_{\langle X \rangle}$ maps the nuclear spin state to NV electron in a non-demolition fashion

$$\begin{aligned} \mathrm{U}_{\langle X \rangle} |0, +\rangle &= |1, +\rangle , \\ \mathrm{U}_{\langle X \rangle} |0, -\rangle &= |0, -\rangle . \end{aligned} \tag{6.8}$$

In addition, for weakly-coupled ^{13}C , strong laser illumination for NV readout does not decohere the ^{13}C [142]. It is therefore possible to repetitively readout the nuclear spin to increase SNR, and even achieve single-shot readout [156, 142, 216, 74, 130].

The ability to read out individual nuclear spin state in a single shot would allow state preparation-by-measurement. In this case, the nuclear spin state initialization fidelity is no longer limited by NV polarization, but rather by the single-shot readout fidelity and the fidelity of quantum-non-demolition. In two experiments involving weakly coupled nuclear spins similar to our implementation scenario, the fidelity of preparation-by-measurement can easily go beyond 95% by discarding less confident

data in post-processing [142, 130]. The initial NV-^{13}C state is then

$$\rho = (p_1\rho_0 + p_2\rho_m + p_3\rho_s + p_4\rho_c) \otimes \rho_0. \tag{6.9}$$

We remark that for nuclear spin control and two-qubit readout, we still have to use the NV electron. However, single-shot readout circumvents the loss of contrast due to NV reinitialization (Eq. 6.4, 6.6), which results in a maximum readout contrast via NV $C_{\max} = 1$ and is independent of the total number of nuclear spins involved. In the two nuclear spin case for QEC, this increase in contrast is about a factor of 2.

Also noteworthy, NV charge state initialization has been demonstrated at room temperature [15, 71]. It is therefore possible to have $p_1 > 0.95$ [211], and true entanglement proven in experiment at room temperature. Without these components, the measured state fidelities (e.g. in Chapter. 5) differ from the actual fidelity by the normalization factor $p_1 \approx 70\%$, which prohibits demonstration of entanglement. We remark however, the characterizations of the (entangling) gates for QEC in Chapter. 5 are faithful.

6.3 Improving the Fidelity Limit Due to NV Decoherence

Another challenge at room-temperature is the limited coherence time of NV electronic spin. Take the CU_y gate required in the QEC recover operation as an example. In its current form, the gate lasts $\sim 500\mu s$. For an NV electron with $T_2 = 1.6$ ms, this corresponds to $\sim 10\%$ of coherence loss, coutneracting the gain from QEC. To make QEC useful, these overheads need be suppressed. We discuss two strategies here.

The first one is to increase the coherence time of NV. It has been shown that the coherence time of NV in electronic grade diamond sample at room temperature is limited by the spin bath of ^{13}C [47], and researchers have observed elongated NV coherence time in isotopically purified samples [142, 216]. It is therefore straightforward to decrease the ^{13}C abundance in exchange for longer NV coherence time. In turn,

the NV no longer needs protection from DD and ^{13}C nuclear spins could be directly driven by RF field just like ^{14}N . The control fidelity is likely to improve. Although isotopic purification also reduces number of ^{13}C nuclear spins in each quantum register, a trade-off is possible [216]. Alternatively, better DD could fully decouple NV from the spin bath, yielding phonon process limited decoherence [20]. This limit by phonon could be further improved by lowering the temperature. At 4 K, 1 s coherence was achieved in experiment [4]. Although at lower temperature, due to the increase in T_1 of NV electron, the nuclear spin coherence time is no longer due to the NV fluctuation at idling, our hardware-efficient QEC code could still prove useful. This is discussed in the next section.

The second approach is to employ faster nuclear spin control gates to reduce the QEC overhead limited by NV coherence. Higher RF field increases the nuclear Rabi frequency and decreases the DDRF gate time correspondingly. This is easily achieved by increasing the RF driving power with a by-product of overheating the sample, or improving the RF delivery. Currently we deliver both MW and RF field via a coplanar waveguide (CPW) fabricated on glass substrate glued to the diamond chip. The glass substrate with CPW is bonded to a PCB board mounted on piezo stage. To facilitate the increased heat generation with higher RF power, one can replace the glass substrate and PCB with a better heat-conducting material like SiC. The transparent SiC substrate could serve both as the optical window for confocal microscope and part of the heat sink that dissipates heat generated by RF. In the meanwhile, the current CPW is not well impedance matched to 50 Ω. A better CPW design could improve RF power transmission efficiency, and enhance the RF driving field.

In addition to hardware improvement, we could apply faster nuclear spin gates by improving the quantum control. Again we take the CU_y gate for example

$$\begin{aligned} \mathrm{CU}_y &= |0\rangle\langle 0| \mathbb{1} + |1\rangle\langle 1| \mathrm{U}_y \\ &= |0\rangle\langle 0| \mathbb{1} + |1\rangle\langle 1| \mathrm{R}_x(\pi) \\ &= \mathrm{R}_x(\tfrac{\pi}{2})\mathrm{CR}_x(\tfrac{\pi}{2}). \end{aligned} \tag{6.10}$$

Due to the limitation of DDRF in its current form, the qubit is constantly rotating whether the control qubit is in $|0\rangle$ or $|1\rangle$. The control qubit only determines the direction of the qubit rotation. Consequently, a CNOT type of gate is twice as long as the control actually requires. In Eq. 6.10, half of the total gate time is wasted to realize the identity operator via a rotation and then counter-rotation when NV in $|m_s = 0\rangle$. By incorporating double quantum dynamical decoupling instead of single quantum dynamical decoupling in the DDRF sequence, we could avoid this dilemma and shorten the gate time by half. When NV is in either state $|m_s = \pm 1\rangle$, the hyperfine interaction is on, and we can selectively address the same ^{13}C by resonant RF field. To build up the RF driving constructively, we now require

$$\varphi_k = \varphi_0 + (k-1)\varphi_\tau \tag{6.11}$$

where $\varphi_\tau = (\omega_2 - \omega_1)\tau$, with ω_1, ω_2 being the RF frequency when $|m_s = \pm 1\rangle$.

Although DQ coherence time is typicaly shorter than SQ [139], anormalous decoherence where DQ coherence time outlasts the SQ is also demonstrated both theoretically [231] and experimentally [103]. It is therefore possible to both increase the decoherence time and shorten the gate time simultaneously.

Once the nuclear spin coherence time goes beyond the limit due to NV T_1 fluctuation with the help of our hardware-efficient QEC, the ^{13}C -^{13}C dipolar interaction kicks in. These nuclear-nuclear spin interactions are on the order of $100 - 1000$ Hz for diamond sample with natural abundance carbon [34, 4, 3]. The dipolar interaction can be easily suppressed by having the NV idle in $|m_s = \pm 1\rangle$ [34]. The $\sim$ 10 kHz hyperfine interaction creates a frozen core around the NV where ^{13}C 's inside the core are protected from the dipolar interaction of the ^{13}C spin bath due to energy mismatch. Another factor to consider is the nuclear spin T_1 limit. This is usually a few seconds at room temperature, and could be improved by three orders of magnitude at elevated magnetic field [11].

6.4 Nuclear Spin Coherence Beyond Room-Temperature NV Fluctuation

Looking forward, we consider our hardware-efficient QEC code for common fluctuator dephasing (CFD) advantagenous beyond correcting nuclear spin dephasing due to the thermal fluctuation of NV at room temperature. Firstly, CFD is a common decoherence model found not only in NV center, but also in quantum dots and superconducting qubits dispersively coupled to a common resonator with non-zero effective temperature [142, 188, 229, 43, 26, 27, 85, 138, 51, 184, 227, 228, 226, 219]. The reduced overhead of such hardware-efficient QEC code could prove useful for NISQ devices, serving as a "firmware" level protection and being concatenated with more general QEC code at higher "software" level.

In addition, hardware-efficient QEC code for CFD is useful in protocols with intrinsic fluctuation. One example of near-term applications is entanglement generation via heralding, which is the key component for a quantum repeater [117, 75, 48]. In this protocol, the NV spin-photon entanglement is first generated at each node. Joint measurement of the photons from different nodes then heralds remote NV electronic spins into an entangled state [24]. Successful entanglement is transferred to local quantum memory for storage while the NV continues to create remote entanglement. The local nuclear spins are typically used as quantum memory [71] and are subject to noise induced by NV during the entanglement generation. When NV goes through optical cycles between ground and excited states, the hyperfine interaction strength with the nuclear spin changes and dephases the nuclear spin. This noise is CFD for the local nuclear spins in the node and a decoherence-protected subspace has proven effective in mitigating the noise [172]. Our hardware-efficient QEC code could further improve the quantum memory and help in quantum repeaters.

Appendix A

Repetitive Readout Enhanced by Machine Learning

Single-shot readout is a key component for scalable quantum information processing. However, many solid-state qubits with favorable properties lack the single-shot readout capability. One solution is to use the repetitive quantum-non-demolition readout technique, where the qubit is correlated with an ancilla, which is subsequently read out. The readout fidelity is therefore limited by the back-action on the qubit from the measurement. Traditionally, a threshold method is taken, where only the total photon count is used to discriminate qubit state, discarding all the information of the back-action hidden in the time trace of repetitive readout measurement. Here we show by using machine learning (ML), one obtains higher readout fidelity by taking advantage of the time trace data. ML is able to identify when back-action happened, and correctly read out the original state. Since the information is already recorded (but usually discarded), this improvement in fidelity does not consume additional experimental time, and could be directly applied to preparation-by-measurement and quantum metrology applications involving repetitive readout.

A.1 Introduction

Single-shot readout is a key component for scalable quantum information processing [68, 169], for its close connection to state initialization and fault-tolerant quantum error correction [157]. Indeed, it is one of the main deciding factors in the selection of potential qubits. Single-shot readout has been achieved in various physical qubit systems, ranging from neutral atoms [17, 77, 54], to trapped ions [152], superconducting qubit [108], and solid-state defect centers [148, 76, 96, 156, 142, 74, 216, 130]. There are however situations where a candidate qubit has favorable coherence properties, but does not naturally come with single-shot readout capabilities. Examples include Al^+ ions [183, 104] and room-temperature nitrogen-vacancy (NV) centers in diamond [156, 142, 74, 216, 130], where a closed optical cycle for readout is either lacking, or experimentally challenging. A solution to this problem is through repetitive quantum-non-demolition (QND) measurements [104].

In the repetitive QND protocol, a Controlled-NOT (CNOT) gate is applied to correlate the qubit state to an ancilla, which is subsequently read out (Fig. A-1 (a)). If the readout operator commutes with the qubit's intrinsic Hamiltonian, in other words, if the readout is QND, one can repeat the above process multiple times to increase signal-to-noise ratio, until the desired fidelity is reached.

This protocol is also known as the repetitive readout technique widely adopted in NV research at room-temperature, where the nuclear spin state (here the ^{14}N or a ^{13}C) is repetitively read out with the help of the NV electronic spin [110, 156]. In its implementations so far, the spin state was determined by comparing the total photon number collected through all the repetitive readouts with a previously established *threshold* (Fig. A-1 (b)). The detected photon count numbers are thus divided into two classes, referred to as bright (dark) state of the qubit.

In this threshold method (TM), the readout infidelity can be evaluated from the overlap between the photon count distributions of bright and dark states. Two factors contribute to this overlap: inefficient optical readout [59], including photon shot noise and limited photon collection efficiency; and deviation from the QND condition. The

first factor can be improved by embedding the emitter into photonic structures and by using better single photon detectors. The second factor imposes a more fundamental constraint. Indeed, if the readout operator does not fully commute with the system Hamiltonian, back-action from the measurement will eventually limit the number of photons that can be collected before quantum information is destroyed [58, 164].

To mitigate this effect, we propose to use the additional information carried by the measurement-induced state perturbation itself. Information about the perturbation is already recorded during typical experiments, in the form of the time trace of photon clicks from the repetitive readouts (Fig. A-1 (c)), but is usually discarded in the TM after extracting the total photon number. Identifying the perturbation and tracing back to the unperturbed original state using this information is the key to improving the fidelity of readout.

Unfortunately, finding an elegant analytical approach proves difficult–the complexity of the photodynamics exhibits intrinsic randomness, and the inefficient photon collection process yields noisy data, precluding clean analytical analysis that would take advantage of the additional information. On the other hand, machine learning (ML) is designed to discover hidden data correlations, and it is widely used in classification problems [121]. It has been recently introduced in quantum information tasks to mitigate crosstalks in multi-qubit readout [185], to enhance quantum metrology [180, 67], to identify quantum phases of matter and phase transitions [41, 212, 127], to identify entanglement [134, 135, 86], and even to determine existence of quantum advantage [145], to name a few. In particular, ML shows success in efficient interpretation of quantum state tomography (QST), by being robust to partial QST and state-preparation-and-measurement (SPAM) errors [86, 208, 162, 209].

In this work, we apply ML to state discrimination for the repetitive readout of NV center. To design and evaluate the ML method, we use the full information from time trace data generated by quantum Monte-Carlo simulation. We tried different supervised ML methods and mainly focused on a shallow neural network realized using MATLAB® Neural Net Pattern Recognition tool (npartool). We observed consistent increase in readout fidelity using ML over TM. The improvement in readout fidelity

albeit small is robust over a parameter space that covers individual NV differences. One application of our results is in preparation-by-measurement: when one discards less trustworthy measurements, ML yields a more efficient initialization process than TM.

Since in our method the training labels are readily available in experiments with very high fidelity [156, 142, 216, 74, 130], it can be readily applied to current experiments. Together with the robustness of our method over NV photodynamic parameters, we expect that the improved readout fidelity can be achieved in experiments.

A.2 Repetitive Readout Model and Simulation

We consider reading out the native ^{14}N nuclear spin state through the electronic spin of NV center at room-temperature as an example. The NV center's ground state is an electronic spin triplet ($S = 1$), and can be optically polarized to the $|m_s = 0\rangle$ state. The other two sublevels $|m_s = \pm 1\rangle$ have additional non-radiative decay channels under optical illumination, allowing optical readout of spin state by fluorescence intensity. The native ^{14}N nuclear spin is a nuclear spin-1 ($I = 1$), and couples to the NV center through hyperfine interaction. ^{14}N does not have optical readout, but it supports a C_nNOT_e operation (control on nuclear spin and NOT gate on electronic spin): $|m_s = 0, m_I = +1\rangle \leftrightarrow |m_s = +1, m_I = +1\rangle$, and $|m_s, m_I = 0, -1\rangle \leftrightarrow |m_s, m_I = 0, -1\rangle$, which correlates the ^{14}N to the NV state.

In the repetitive readout protocol, the NV starts in $|m_s = 0\rangle$, and a CNOT gate correlates the nuclear spin state to NV. A green laser then reads out the NV state, while also repolarizing it back to $|m_s = 0\rangle$. Under high magnetic field, where the NV and ^{14}N energies are well separated, this process is approximately QND and can be repeated a few thousand times to accumulate signal, discriminating the bright $|m_I = 0, -1\rangle$ (dark $|m_I = +1\rangle$) state of ^{14}N in a single shot (Fig. A-1). Still, the high magnetic field cannot fully eliminate back-action of the measurement on ^{14}N , which is caused by the relatively strong excited state transverse hyperfine interaction $A_\perp(S_+I_- + S_-I_+)$. This perturbation causes flip-flips between NV and the ^{14}N ,

destroying the quantum information. In the TM, this perturbation prevents us from keeping to accumulate useful signal and reduces the fidelity of state discrimination. ML, instead, as we find out, can identify the majority of such flips and therefore improve the readout fidelity. Ultimately, the readout fidelity is limited by flips that occur very early during repetitive readout.

We used simulated data to explore the effectiveness of ML in repetitive readout and to better analyze the source of improvement. To fully capture the photodynamics involved in the repetitive readout process, we employed a 33-level model, considering the NV^- electronic and ^{14}N nuclear spins and the neutrally charged NV^0 state. The model is described in more detail in the Appendix. Most transition rates in the model were accurately measured from independent experiments [174, 207, 93, 140] and we use values from Gupta et al [93]. The excited state NV-^{14}N transverse hyperfine interaction strength and NV^- to NV^0 (de)ionization rate at strong laser power were not precisely determined before, and therefore a reasonable range is explored to cover possible variations in individual NVs, based on the results from [142, 156, 165, 84].

In the simulation, we assumed an intermediate magnetic field of 7500 G typical for repetitive readout experiments, and a photon collection efficiency of 30%, standard with photonic structures like solid immersion lens or parabolic mirrors on the diamond [141, 175, 217]. A perfect CNOT gate connecting $|m_s = 0, m_I = +1\rangle \leftrightarrow |m_s = +1, m_I = +1\rangle$ was assumed. Correspondingly, the dark state is $|m_I = +1\rangle$, and bright state is $|m_I = 0, -1\rangle$.

We remark that it is possible to use the same protocol to read out ^{13}C rather than ^{14}N [74, 216, 142, 130], given well-characterized hyperfine interaction strengths [105, 168, 195, 73].

A.3 Neural Network Architecture

The network in nprtool is a two-layer feed-forward neuron network (Fig. A-1 (c)). In all trainings, we used a data set of size $10,000$ with a random portion of 15% for validation. The input data is the time trace of single photon detector clicks through

the repetitive readout process (Fig. A-1 (c)). Because the total photon count is a good metric for state discrimination, we take the cumulative sum of the time trace of photon detection $\{x_k\}$ before feeding it to the neural network $\bar{x}_i = \sum_{k=1}^{i} x_k$. Out of the $10,000$ data, half are dark state $|m_I = +1\rangle$, while the other half are bright with a $1:1$ ratio between $|m_I = 0\rangle$ and $|m_I = -1\rangle$. After training, we used a test set of size $4,000$, which was generated in the same way as the training set but not used in training, to independently test the network. We performed Monte Carlo cross-validation, which typically repeated the aforementioned training process 10 times and the average accuracy was used throughout this work. Error bars represent the standard error of the 10 results.

We found that approximately 12.5 neurons per 1000 repetitions was a good balance between the increase in fidelity and avoidance of overfitting.

A.4 Results

We first investigate the influence of the repetition number on readout fidelity. The fidelity F across this manuscript is defined as

$$F = \frac{F_{\text{bright}} + F_{\text{dark}}}{2} \tag{A.1}$$

where F_{bright} and F_{dark} are the percentage of bright and dark states that are correctly read out, respectively.

The number of repetition influences the readout fidelity in two ways: 1. A larger repetition number means more photons detected and better separation between photon count distributions of the bright (dark) states (Fig. A-1 (b)). 2. A larger repetition number, however, also implies a longer illumination time and a higher probability of the ^{14}N nuclear spin to flip, due to the large transverse hyperfine interaction in the excited state, which mixes the photon count distributions of two initially different states. As a result of these competing effects, there is an optimal repetition number N_{opt} for the TM. On the other hand, the readout fidelity from ML keeps improving as

we increase the repetition number even if the increase rate slows down (Fig. A-2 (a)). At N_{opt}, we observed a 0.34% increase in fidelity with ML. Since the time trace input for ML is recorded in all experiments even when intended for TM, this improved fidelity does not consume additional experimental time. One can add more repetitions in the experiment, and harness a further increase as much as 0.57% in readout fidelity (compared to TM at N_{opt}). The improvement at $N > N_{\text{opt}}$ suggests that ML is not only more robust against ^{14}N flips, but rather extracts useful information from the flips. This is investigated in more detail later.

As mentioned earlier, the excited state transverse hyperfine interaction strength $A_\perp$ between NV and ^{14}N , and (de)ionization rate $k_{\text{ion}}(k_{\text{deion}})$ between NV^- and NV^0 under strong illumination have been not yet determined to satisfactory precision. We therefore explored a parameter range to cover realistic values one might encounter in experiment: $A_\perp = \{-30, -40, -50\}$ MHz and $k_{\text{ion}} = \{70, 90, 110\} \times \beta$ MHz, where β is a unit-less value proportional to laser power. In the simulation, we choose β such that for any combination of parameters the NV would emit the same total number of photons in the bright state during repetitive readout. Comparisons of TM at N_{opt}, ML at N_{opt} and ML at $N = 8000$ are shown in Fig. A-2 (b) under different $A_\perp, k_{\text{ion}}$. The trend matches Fig. A-2 (a). ML consistently outperforms TM with both repetition numbers chosen.

To better understand how ML achieves higher fidelity, we take a closer look at cases where ^{14}N experienced flip-flops in the excited state, which is a major limit to the TM fidelity. We find the neural network is able to extract information from the time trace input to recognize if a flip has occurred, and recover the original state. Such flips could bring the photon count across the threshold, yielding misclassification when using TM. This is shown in Fig. A-3, where we plot the cumulative sum of the time traces in cases where flip(s) occurred. In Fig. A-3 (a), ML correctly assigns all these time traces to their original states, while TM looks only at the total photon count at the end and compares it to the threshold (dashed line), making $\sim 25\%$ wrong decisions. In Fig. A-3 (b), we show instances when ML gave the wrong classification. We notice that in those cases, the ^{14}N flip-flops happen at the very beginning, making

the time traces indistinguishable from those of the opposite initial state with no flips. There is little hope in correctly reading out these states, posing an ultimate limit to the readout fidelity.

Another important objective of ML is that of generalization. We explore this generalization power by testing the network R trained by $\{k_{\text{ion}} = 90\beta\text{MHz}, A_\perp = -50\text{MHz}\}$ on data generated with different parameters.

First, we test the network R on different (de)ionization rate $\{k_{\text{ion}} = 110\beta\text{MHz}, A_\perp = -50\text{MHz}\}$, obtaining a fidelity of 94.4(1)% from the network R, compared to 96.31(4)% from TM. We attribute this deteriorated performance of ML to the change in the photodynamics. Under the same condition, different k_{ion} change the relative distributions of bright and dark states. This change cannot be compensated by laser intensity, and makes the network R obsolete.

We then tested the network R on data of different transverse hyperfine strengths, $A_\perp = \{-40, -30\}$ MHz. Intuitively, a small change in $A_\perp$ does not change the photoluminescence pattern, but rather modifies the ^{14}N flip-flop rate a little, which could be captured by the network, given its ability to recognize the occurrence of flip-flops. Indeed, we observed better fidelity from the network R on $A_\perp = -40$ MHz data than TM, and comparable fidelity to TM on $A_\perp = -30$ MHz, where the parameter has changed by 40% (Table. A.1). Here we used N_{opt} of the test data for both ML and network R. These results indicated that provided variations in the NV parameters are small, it is possible to use a fixed network R to directly read out any NV, without the need to run experiments to generate the traning data.

$A_\perp$ (MHz)	TM fidelity	ML fidelity	network R fidelity
-40	97.94(2)%	98.20(4)%	98.24(4)%
-30	98.67(2)%	98.76(3)%	98.66(4)%

Table A.1: Robustness test of network R trained with $\{k_{\text{ion}} = 90\beta\text{MHz}, A_\perp = -50\text{MHz}\}$. We compare the readout fidelities of test data with different $A_\perp$ from TM, ML, and network R. The result from network R is better than TM when $A_\perp$ is not changed too much.

A.5 Application to initialization by readout

One scenario where even a modest increase in the fidelity can be beneficial is in state preparation-by-measurement [156, 142, 74, 216, 130]. In this is a widely adopted technique, to achieve a higher fidelity of state preparation with the TM, two distinct thresholds are set, $N_{\text{dark}} < N_{\text{th}}$ and $N_{\text{bright}} > N_{\text{th}}$, where N_{th} is the readout threshold. Measurements in between the two thresholds are discarded, as they cannot be assigned to either bright or dark state with enough confidence. This leads to a lengthier state preparation routine. In ML, the neural network assigns each input to a probability p_{bright} (p_{dark}) of the state being bright (dark). A final step compares $p_{\text{bright}}, p_{\text{dark}}$ and classifies accordingly. To achieve a higher fidelity, we discard cases where $0.5 - t < p_{\text{dark/bright}} < 0.5 + t$, with an adjustable threshold t. We compare the state preparation fidelity from TM and ML, when discarding the same amount of data, and observe that ML maintains its advantage over TM, and scales more favorably than TM with the ratio of discarded measurements (Fig. A-4). This enables preparing a high fidelity initial state more efficiently. We observed similar improvement from unsupervised learning (see Appendix), agreeing with [137].

A.6 Conclusion and Outlook

In conclusion, we have shown that ML techniques can exploit the hidden structure in the repetitive readout data of NV center at room-temperature to improve the state measurement fidelity. We used Quantum Monte-Carlo simulation based on a 33-level NV model to generate data for machine learning, and found improved single-shot readout fidelity over the traditional threshold method, that can be attributed to the ML ability to correctly classify a larger number of readout trajectory that are perturbed by the measurement process itself.

While we used simulations, generally the training process does not depend on knowledge of the model. In fact, the only information required is the label for the state ($|m_I = +1\rangle$ or $|m_I = 0, -1\rangle$), which is readily available in experiments by discarding

less trustworthy data [156, 142, 74, 216, 130]. One can then use this data to train a network specific to the NV of interest, and expect an increase in readout fidelity in all subsequent repetitive readout experiments, free of any additional experimental time (although at the cost of an increased computational time). Although individual NVs may have slightly different photodynamic parameters, they should be covered by the range we explored in this work, and therefore the improvement in fidelity is expected to be ubiquitous.

In addition, the off-the-shelf MATLAB® deep learning toolbox we employed greatly reduces the complexities in the neuron network architecture, making this improvement easily reproducible and more accessible to experimentalists.

Though small, the increase in fidelity does not require any additional experimental time, and is readily compatible with experiments using repetitive readout of nuclear spins, including in quantum metrology [16, 133, 63] to improve sensitivity.

To further shed light on the bright/dark decisions that affect the ML readout fidelity, one could use decision tree learning instead of a neuron network. This could potentially inform optimized readout protocols, with varying illumination times, or help further improve the neuron network architecture. More broadly, ML could be applied to more complex systems, for example to help mitigate crosstalk of fluorescence signals in a solid-state register consisting of a few nearby NV or other color centers [185].

Acknowledgements

This work was supported in part by the NSF grant EFRI-ACQUIRE 1641064 and by Skoltech.

The data that support the findings of this study are openly available at DOI insert URL.

A.7 Appendix I: NV model and Quantum Monte-Carlo Simulation

We used a 33-level model to fully describe the dynamics of NV-^{14}N in the repetitive readout process. This model includes the spin-1 triplet ground and excited states, and singlet metastable state for NV^-, the spin-1/2 ground and excited states for NV^0, and the nuclear spin-1 of ^{14}N , as illustrated in Fig. A-5. The transition rates directly related to the NV photoluminescence have been precisely determined and reported in various works [174, 207, 93, 140], although with some significant variations. For the simulation we took the values from Gupta *et al.* [93] listed in Table. A.2.

transition rates	k_r	k_{47}	k_{57}	k_{71}	k_{72}
(MHz)	65.9	92.1	11.4	1.18	4.84

Table A.2: Transition rates used in the 33-level model.

The exact (de)ionization mechanisms under 532 nm laser illumination have not been yet determined experimentally, neither have the (de)ionization rate under laser-power comparable to the saturation power (measurement under weak power can be found in [15, 45, 94]). Here we assume the (de)ionization $k_{\text{ion}}(k_{\text{deion}})$ occurs only in the excited states, and obeys selection rules as illustrated in Fig. A-5. To maintain the experimentally determined 70/30 ratio [15] between the charge states, we set $k_{\text{deion}} = 2k_{\text{ion}}$. The ionization rate is proportional to the laser intensity, which is swept around $k_{\text{ion}} \approx 90\beta$ MHz, in accordance with [142].

When the magnetic field is applied along the NV-axis, the ground state NV-^{14}N Hamiltonian has negligible effect on the repetitive readout, thus it is not considered in the numerical simulation. The NV^- excited state Hamiltonian reads:

$$H_- = \Delta_{es} S_z^2 + Q I_z^2 + \gamma_e B S_z + \gamma_n B I_z + \mathbf{S} \cdot \mathbf{A} \cdot \mathbf{I} \tag{A.2}$$

where $\mathbf{S}$ and $\mathbf{I}$ are the electronic and nuclear spin operators, $\Delta_{es} = 1.42$ GHz is the zero-field splitting of the electronic spin, $Q = -4.945$ MHz the nuclear quadrupole interaction [196], and $\gamma_e = 2.802$ MHz/G and $\gamma_n = -0.308$ kHz/G the electronic

and nuclear gyromagnetic ratios. The hyperfine interaction term is diagonal due to symmetry:

$$\mathbf{S}\cdot\mathbf{A}\cdot\mathbf{I} = A_{\parallel}S_zI_z + A_{\perp}(S_xI_x + S_yI_y) \tag{A.3}$$

where $A_{\parallel} = -40$ MHz were determined via ODMR experiment [154]. $A_{\perp}$ was believed to be similar to $A_{\parallel}$ and is recently measured between -40 and -50 MHz [165].

The NV^0 excited state Hamiltonian takes the form:

$$H_0 = QI_z^2 + \gamma_e BS_z + \gamma_n BI_z + \mathbf{S}\cdot\mathbf{C}\cdot\mathbf{I} \tag{A.4}$$

with the hyperfine interaction term:

$$\mathbf{S}\cdot\mathbf{C}\cdot\mathbf{I} = C_{\parallel}S_zI_z + C_{\perp}(S_xI_x + S_yI_y) \tag{A.5}$$

The hyperfine interaction strengths were considered similar to those in the NV^- excited state [84], and we set $C_{\parallel} = C_{\perp} = -40$MHz.

To simulate repetitive readout experiments for both the training and testing data, we used the quantum Monte-Carlo method based on the aforementioned 33-level model. One challenge lies in the various time scales involved in the numerical simulation, from the electronic spin's fast oscillation $\omega \sim (2\pi)\cdot 10$ GHz, to the optical transition rates $k_{ij} \sim 100$ MHz, to the flip-flop rate of ^{14}N nuclear spin $1/T_1^n \sim$ kHz. We mitigate this issue by employing the Born-Oppenheimer approximation [32] in our numerical simulation, and average out the fast oscillation at ω as following.

We define δp_{mn} as the transition probability from the state $|m\rangle$ to $|n\rangle$ in the time step δt. Starting from $|\psi(t=0)\rangle = |m\rangle$, we have

$$\begin{aligned}\delta p_{mn} &= \int_0^{\delta t}\left(\sum_{i=1}^{33}|\langle n|i\rangle|^2\ |\langle i|\psi(t)\rangle|^2\right)dt \\ &= \sum_{i=1}^{33}\left(k_{in}\int_0^{\delta t}|\langle i|\psi(t)\rangle|^2 dt\right)\end{aligned} \tag{A.6}$$

Notice that $|\langle i|\psi(t)\rangle|^2$ is periodic with period $2\pi/\omega$, which is much smaller than the

time step $\delta t \sim 1/k_{ij}$. Thus, we assume only the average effect of this oscillation is seen in each time step, and numerically find $\langle \frac{\delta p_{mn}}{\delta t} \rangle$. This allows us to efficiently perform the quantum Monte-Carlo simulation.

A.8 Appendix II: Machine Learning Discussions

A.8.1 Recurrent Neural Network

Recurrent neural network (RNN) is a commonly used architecture specializing in time-series data with the capability to understand the correlation within the time-series. In the main text, we showed results obtained using shallow neural network. In order to see if we gain by exploiting the correlation within the time series we also tested the performance of an advanced recurrent neural network: long short-term memory (LSTM). Due to the nature of recurrent neural network, the training process is very time-consuming and therefore not suitable for exploring multiple parameters in our model. To speed up the training process, we averaged the input time trace data over 100 realizations, to greatly reduce the training set dimension. Indeed, this may have caused some loss of information. The result though still consistently outperforms the TM and is comparable to the shallow neural network shown in the main text (see Table. A.3). One remark is that we did not take the cumulative sum for the input data, because LSTM specializes in time series data and is able to recognize some quasi-periodic patterns.

$A_\perp$ (MHz)	k_{ion} (MHz)	TM fidelity	ML fidelity	LSTM fidelity
-50	70β	97.56(4)%	97.86(7)%	97.61(5)%
	90β	96.98(4)%	97.32(5)%	97.40(2)%
	110β	96.31(4)%	96.71(5)%	96.77(7)%
-30	90β	98.67(2)%	98.76(3)%	98.44(3)%
-40		97.94(2)%	98.20(4)%	98.29(3)%
-50		96.98(4)%	97.32(5)%	97.40(2)%

Table A.3: Comparison between the fidelity obtained through TM, ML and LSTM under different parameters. All training and testings were conducted at the N_{opt} of that set of parameters. Overall, the LSTM algorithm has similar performance compared with the shallow neural network.

A.8.2 Unsupervised learning

In the main text we compared the enhanced fidelities of TM and supervised learning after discarding less trustworthy data. Another possibility is to use unsupervised learning [137]. This method is of interest because unsupervised learning does not require any well-labelled data. We implemented the k-means algorithm that classifies a given data set into k different groups.

We first use the TM readout to obtain a bright (dark) group of measurement trajectories. We then perform k-means on the bright (dark) group to further classify it into k subgroups. The fidelity increases when we discard the smallest subgroup. Compared to the TM, k-means gives better fidelity as shown in Fig. A-6, because the unsupervised learning extracts some information about ^{14}N flips through the hidden structures in time trace data, in agreement with [137]. Note that unlike TM or supervised learning, we cannot control the ratio of discarded data. Therefore, the fidelity defined by Eq. A.1 is not available, and only the fidelity of dark state is shown. We also remark that in rare cases, k-means gives outlier results with fidelity much worse than TM.

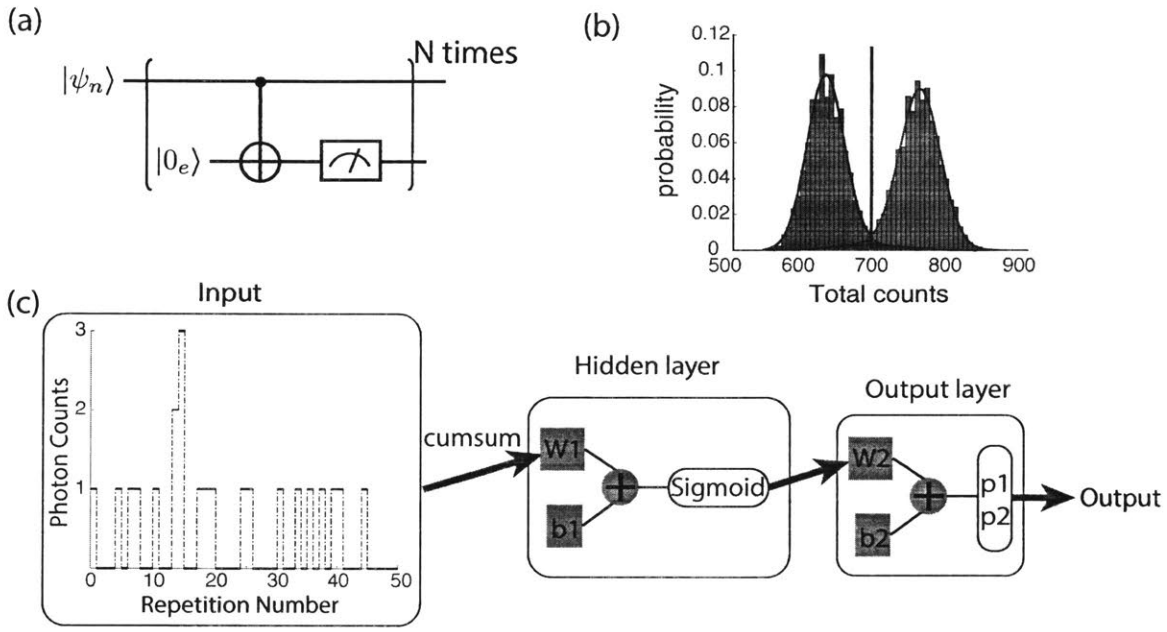

Figure A-1: (a) Quantum circuit for repetitive quantum-non-demolition readout of the nuclear spin state $|\psi_n\rangle$, using the ancilla electronic spin ($|0_e\rangle$). Here we assume e.g., to map the $|m_I = 0\rangle$ nuclear spin state to the NV $|m_S = 0\rangle$ state and the $|m_I = +1\rangle$ state to the $|m_s = +1\rangle$ state. (b) A typical histogram of total photon numbers collected from repetitive readout, originating from bright (red, $|m_I = 0, -1\rangle$) and dark (grey, $|m_I = +1\rangle$) states, is generated using simulation. A threshold at the cross point classifies future readout results in the threshold method. (c) Shallow neuron network architecture of MATLAB® Neural Net Pattern Recognition tool (nprtool), with sigmoid as activation function and softmax output. nprtool only allows users to change the number of neurons in the hidden layer for high dimensional data. The ML input is the time trace of single photon detector clicks x_k (at repetition k) in individual repetitive readout experiment, and we take the cumulative sum ("cumsum") $\bar{x}_i = \sum_{k=1}^{i} x_k$ of individual time traces before feeding the data to the neural network. W1 (W2) and b1 (b2) are the weights and bias of the hidden (output) layer, which are learnable parameters of the network. The output is the probability p1 (p2) of the state being dark (bright).

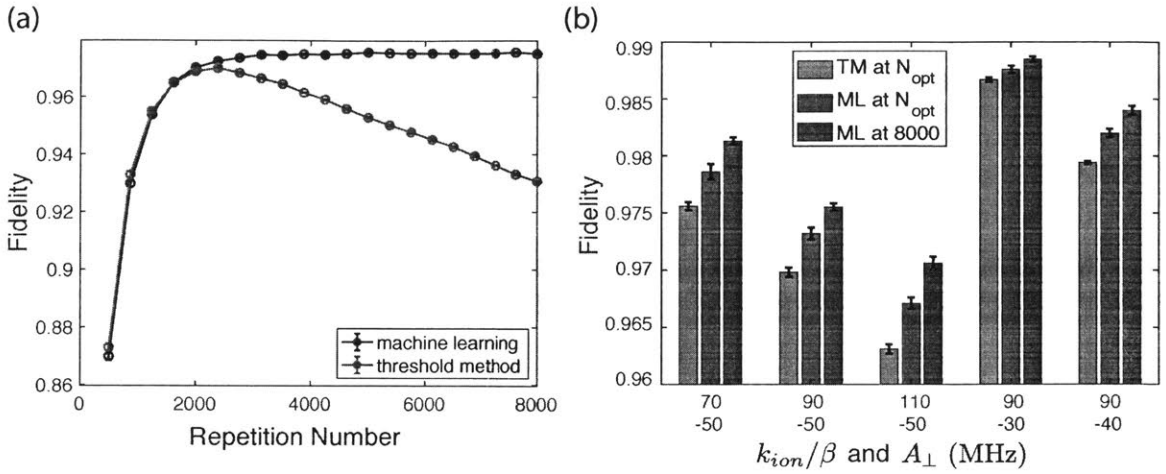

Figure A-2: (a) Readout fidelity as a function of repetition number N in the repetitive readout. The fidelity from TM (grey) declines after $N_{\text{opt}} = 2375$ due to increasing probability of ^{14}N nuclear spin flips. The fidelity from ML keeps improving, although the increase rate slows down. For each repetition number, we retrain the network and take the average fidelity over 10 trainings. Error bars are the standard error of the 10 training results and are smaller than markers. Simulation parameters: $\{k_{\text{ion}} = 90\beta\text{MHz}, A_\perp = -50\text{MHz}\}$. (b) Fidelity comparison of TM at its optimal repetition number N_{opt}, ML at N_{opt}, and ML at $N = 8000$ under different NV parameters. N_{opt} for each were respectively (from left to right): 2000, 2375, 2750, 3125 and 2750. Error bars are the standard error of 10 training results.

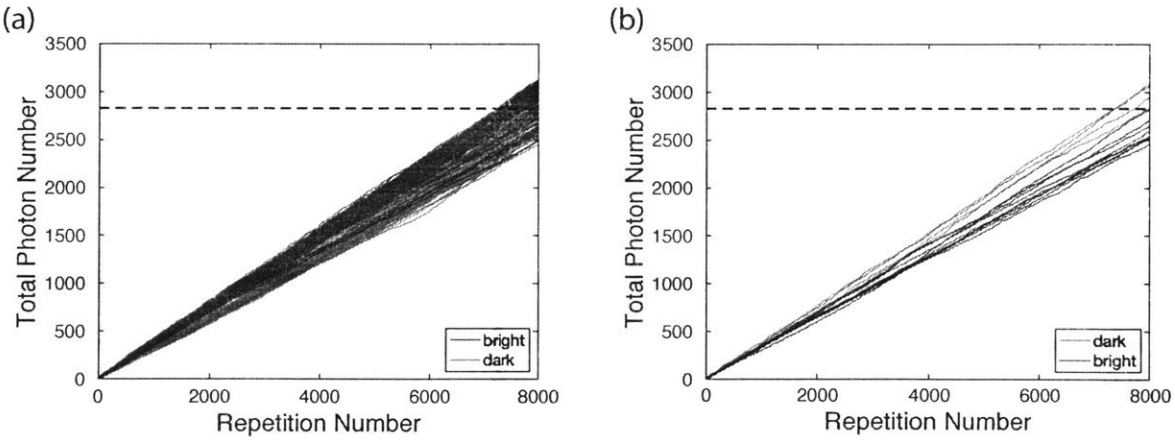

Figure A-3: Cumulative number of photons as a function of read out repetitions. Each trace corresponds to one input to the neural network. All traces shown here experienced at least one ^{14}N flip, and are (a) correctly or (b) wrongly assigned by ML. The larger number of traces in (a) (93.78% of the total number of traces considered) reflects the high fidelity of the ML readout. In contrast, the TM only looks at the final photon number and compares it to the threshold (dashed line), assigning roughly 25% in (a) and all in (b) to the wrong state. In the figures, red lines represent time traces starting in bright state, grey in dark state; the dashed line is the threshold for $N = 8000$.

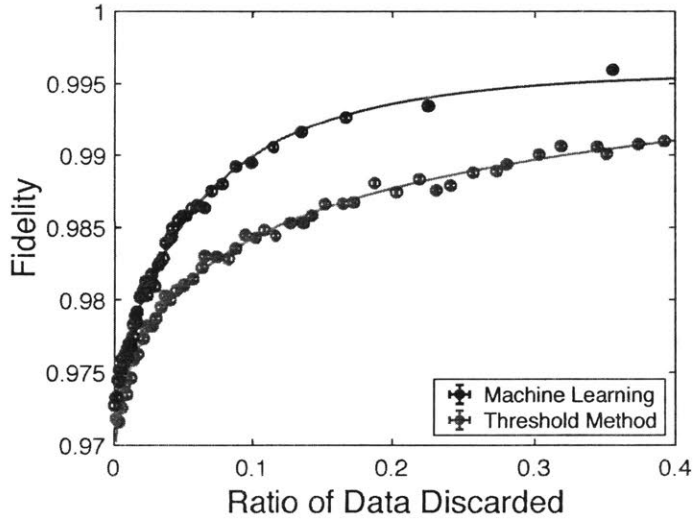

Figure A-4: More efficient state preparation-by-measurement. The state readout fidelity increases after discarding less trustworthy measurements and this improves the state preparation. ML always outperforms TM and scales more favorably with the ratio of discarded data. The solid curves are a guide to the eye. Error bars are the standard error of 10 training results, and are smaller than the marker.

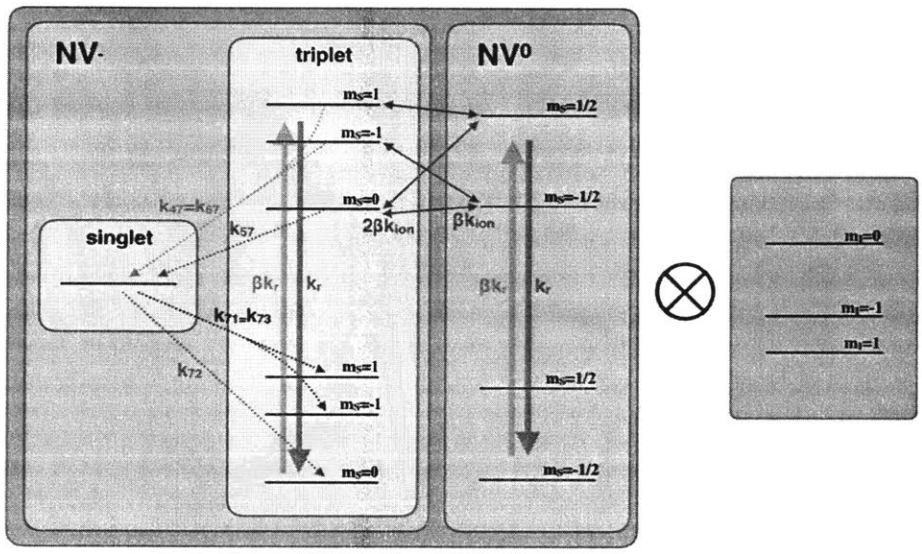

Figure A-5: The 33-level NV model used in our simulation, consisting of 11 electronic spin levels times 3 nuclear spin levels (level spacings not to scale). k_r, $k_{47}(= k_{67})$, k_{57}, $k_{71}(= k_{73})$, k_{72} and k_{ion} are incoherent transition rates connecting the corresponding energy levels. The optical transition rate k_r between excited state and ground state are set equal for $NV^-$and NV^0, and are assumed to be spin-conservative (spin non-conservative part is $< 1\%$ [174]). β is a dimensionless parameter given by the ratio of the laser power to the optical transition rate. $k_{(\text{de})\text{ion}}$ is the (de)ionization rate. We assume the (de)ionization happens in the excited state and follows the selection rules depicted by the brown arrows.

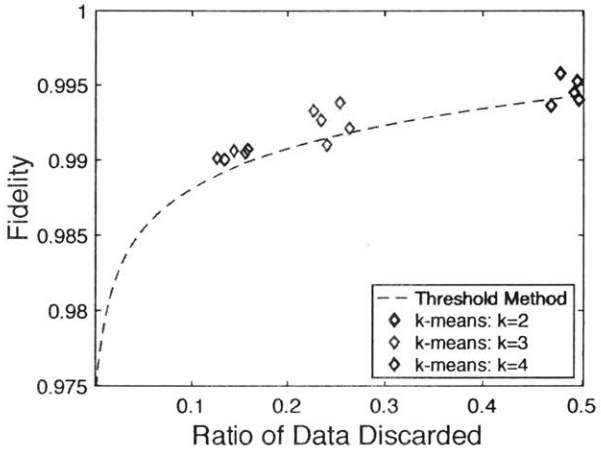

Figure A-6: More efficient state preparation-by-measurement. Improved dark state readout accuracy after discarding less trustworthy readouts. Each diamond-shaped point represents an individual k-means test.

THIS PAGE INTENTIONALLY LEFT BLANK

Appendix B

Rabi Enhancement: Model and Error Analysis

B.1 Exact expressions for the Rabi enhancement

B.1.1 NV center system

For single NV, we effectively polarize the nitrogen nuclear spin at +1 (around excited state level anti-crossing $\sim$ 500G), and the only transition of concern is $|m_I = +1\rangle \leftrightarrow |m_I = 0\rangle$. We simplify the problem by reducing nuclear spin-1 to an effective spin-1/2 system by applying the following transform where a factor of $\sqrt{2}$ is introduced

$$I_z^2, I_z \to \frac{1}{2}\mathbb{1} + I_z, \qquad I_{x,y} \to \sqrt{2} I_{x,y} \tag{B.1}$$

In the main text we described our procedure to find expression for the enhancement of the nuclear spin Rabi nutation due to virtual transitions of the electronic spin. Here we provide the exact expressions for the enhancement factor in each electronic spin

manifold m_s:

$$\begin{aligned}
\alpha_{+1} &= \cos(\vartheta^+) + \frac{\gamma_e}{\gamma_n}\sin(\vartheta^+), \\
\alpha_0 &= \cos(\vartheta^+)\cos(\vartheta^-) - \frac{\gamma_e}{\gamma_n}\sin(\vartheta^+ - \vartheta^-), \\
\alpha_{-1} &= \cos(\vartheta^-) - \frac{\gamma_e}{\gamma_n}\sin(\vartheta^-).
\end{aligned} \tag{B.2}$$

where the rotation angles, as shown in main text, are given by

$$\tan(2\vartheta^+) = \frac{2A_\perp}{\Delta+\gamma_e B_z-\gamma_n B_z-Q} = \frac{2A_\perp}{\omega_{\rm mw}^{+1}-\omega_{\rm rf}^{+1}}, \tag{B.3}$$

$$\tan(2\vartheta^-) = \frac{-2A_\perp}{\Delta-\gamma_e B_z-A_\parallel+\gamma_n B_z+Q} = \frac{-2A_\perp}{\omega_{\rm mw}^{-1}+\omega_{\rm rf}^{-1}+A_\parallel}. \tag{B.4}$$

Here

$$\begin{aligned}
\omega_{\rm mw}^{+1} &= \Delta + \gamma_e B_z + A_\parallel, \\
\omega_{\rm rf}^{+1} &= Q + \gamma_n B_z + A_\parallel, \\
\omega_{\rm mw}^{-1} &= \Delta - \gamma_e B_z - A_\parallel, \\
\omega_{\rm rf}^{-1} &= Q + \gamma_n B_z - A_\parallel.
\end{aligned} \tag{B.5}$$

are the resonance frequencies for electron $|0,+1\rangle \leftrightarrow |\pm1,+1\rangle$ and nuclear $|\pm1,1\rangle \leftrightarrow |\pm1,0\rangle$ transitions, which can be easily obtained experimentally.

Taking the approximation up to first order, we obtain equations linear in $A_\perp$ as given in the main text.

B.1.2 Electronic Spin-1/2

Formulas for the enhancement of the driving frequency when the nuclear spin is coupled to an electronic spin 1/2 have been reported previously [30]. For completeness, we provide here their expressions with the same notations and derivation procedure as above. The system can be subdivided in two manifolds (a double-quantum and a zero-quantum manifold, where the mixing between nuclear and electronic transitions can occur). Following a procedure analogous to what described in the main text, we

can rotate the ZQ manifold and thus obtained the enhancement factors:

$$\begin{aligned} \alpha_{+1/2} &= \cos(\vartheta) + \tfrac{\gamma_e}{\gamma_n}\sin(\vartheta), \\ \alpha_{-1/2} &= \cos(\vartheta) - \tfrac{\gamma_e}{\gamma_n}\sin(\vartheta). \end{aligned} \tag{B.6}$$

where the rotation angle ϑ is given by

$$\tan(2\vartheta) = \frac{\sqrt{2}A_\perp}{\gamma_e B_z - \gamma_n B_z - Q + \frac{A_\parallel}{2}} = \frac{\sqrt{2}A_\perp}{\omega_{\rm mw} - \omega_{\rm rf}}, \tag{B.7}$$

with

$$\omega_{\rm mw} = \gamma_e B_z, \qquad \omega_{\rm rf} = \gamma_n B_z + Q - \frac{A_\parallel}{2}. \tag{B.8}$$

Note that for a nuclear spin 1/2, the same formulas are valid with the replacement $\omega_{\rm rf} = \gamma_n B_z$ and replace $\sqrt{2}A_\perp$ with $A_\perp$.

B.2 Validity of Rabi enhancement formulas

In order to obtain the expressions in Eq. (B.2), we made some approximations; in particular we neglected the counter-rotating term of the RF driving field and, after the diagonalization procedure presented in the main text, we neglect any off-resonance transition involving electronic spin levels. Since for the electronic spin the driving field strength $\gamma_e B_1$ is typically much larger than the driving frequency $\omega_{\rm rf}$, the first approximation might not always hold.

To test the validity of these approximations and thus of our enhancement formulas Eq. (B.2), we performed numerical simulation using a first-order Trotter expansion in the lab frame, thus considering both rotating and counter-rotating terms. Here we used the same parameters as in the experiments. Figure B-1 shows a good agreement between Trotter simulation and our theoretical formula, even for very large RF strength. This indicates that although the nominal bound for the validity of the rotating wave approximation (RWA) for the electronic spin might be broken, its effects on the nuclear spin transitions are small. From these results we conclude that for the RF strengths used in our experiment, effects from counter-rotating fields and other

approximations are on the order of 10^{-4} of Rabi nutation rate, two orders of magnitude smaller than our estimated uncertainty $\delta A_\perp$ and thus do not affect our estimate of the value of $A_\perp$.

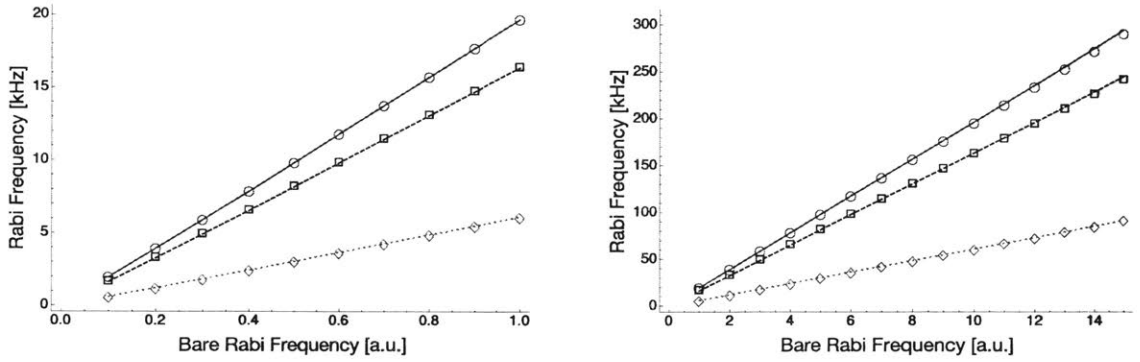

Figure B-1: Left: Comparison between theoretical formula (lines) and Trotter simulation (open symbols). Red, circles, $m_s = 0$. Black (dashed line and squares), $m_s = -1$. Gray (dotted line and diamonds), $m_s = +1$. This range corresponds to our experimental condition, where RWA is shown valid. Relative error between Trotter and theoretical curve is $\sim 10^{-4}$. Right: Comparison between theoretical formula (solid line) and trotter simulation (open symbols) over large range of RF strength. Red, $m_s = 0$. Black, $m_s = -1$. Gray, $m_s = +1$. Good agreement indicates small effects from counter-rotating term.

B.3 Error Analysis

In the main text, when discussing the uncertainty in the estimate of $A_\perp$, resulting from our measurement and fitting procedure, we only considered error from measured nuclear Rabi frequency. For a comprehensive discussion of error, we need to consider all the sources of uncertainty and errors.

Small errors from imperfect MW π pulses duration and nuclear spin polarization contribute to reduction of fluorescent contrast and do not enter our estimation procedure. Under current experimental conditions, these two factors are negligible. The detuning of selective MW pulse is estimated by measuring the linewidth of fourier transformed electronic spin Ramsey signal. To find the uncertainty in RF frequency, we perform pulsed RF excitation, sweeping across the resonance frequency and observing the fluorescence intensity after mapping the nuclear spin state to the electronic

spin. The linewidth of the observed dip provides us a conservative estimate of the uncertainty in $\omega_{\rm rf}$. These uncertainties range from $1.8 - 7.9$ kHz. In the fitting process, uncertainty in $A_{\parallel}$ also contributes linearly. It was measured with high precision before [196].

In the estimation procedure, we truncate Eq.(B.2) to first order and rewrite them in order to express $A_{\perp}$ as a function of experimental measurements:

$$\begin{aligned} A_{\perp} &= \frac{\gamma_n}{\gamma_e}(\omega_{\rm mw}^{+1} - \omega_{\rm rf}^{+1})(\frac{\pi\Omega_{+1}}{\gamma_n B_1} - 1) \\ &= \frac{\gamma_n}{\gamma_e}(\omega_{\rm mw}^{-1} + \omega_{\rm rf}^{-1} + A_{\parallel})(\frac{\pi\Omega_{-1}}{\gamma_n B_1} - 1) \\ &= \frac{\gamma_n}{\gamma_e}(\frac{1}{\omega_{\rm mw}^{+1} - \omega_{\rm rf}^{+1}} + \frac{1}{\omega_{\rm mw}^{-1} + \omega_{\rm rf}^{-1} + A_{\parallel}})^{-1}(1 - \frac{\pi\Omega_0}{\gamma_n B_1}) \end{aligned} \tag{B.9}$$

We calculate contributions to the uncertainty $\delta A_{\perp}$ of $A_{\perp}$ from all fitting parameters using the approximate propagation of error formula, $\delta A_{\perp}(x_1, x_2, \cdots) = \sqrt{\Sigma_n \left(\frac{\partial A_{\perp}}{\partial x_n}\right)^2 \delta x_n^2}$. The contribution of each factor, $D_x = |\frac{\partial A_{\perp}}{\partial x}\delta x|$, calculated according to Eq. B.9 using values from our experiment are reported in Table B.1.

These results show that uncertainties from $\omega_{\rm mw}$, $\omega_{\rm rf}$ and $A_{\parallel}$ are at least 4 orders smaller than that from the measured nuclear Rabi frequency Ω_{m_s}. Therefore, our fitting considering only error from measured Rabi frequency is valid.

The uncertainty in the Rabi frequency is limited by coherence time of the nuclear spin under driving (which can introduce further decoherence due to the driving field instability) and photon shot noise of the optical readout process. Thus the precision of the estimate could be improved with more averaging, at the expense of longer measurement time, or by using more advanced readout techniques [141, 187]. Another limit of a few hundred Hz is imposed by accuracy of γ_e and γ_n, with $\sim 10^{-4}$ relative error [69, 155].

	$\delta\omega_{\mathrm{mw}}$	$D_{\omega_{\mathrm{mw}}}$	$\delta\omega_{\mathrm{rf}}$	$D_{\omega_{\mathrm{rf}}}$	$\delta\Omega_{m_s}$	$D_{\Omega_{m_s}}$	$\delta A_{\parallel}$	$D_{A_{\parallel}}$ (Hz)
$m_s = +1$	5.5×10^3	3	1.8×10^3	1	650	2.7×10^5	2×10^3	0
$m_s = 0$	—	8*	—	11*	1×10^3	1.3×10^5	2×10^3	3
$m_s = -1$	5.5×10^3	10	7.9×10^3	14	1×10^3	1.6×10^5	2×10^3	4

Table B.1: Contribution to uncertainty in $A_\perp$ from all parameters according to Eq. (B.9) and the error propagation formula. D_x stands for $|\frac{\partial A_\perp}{\partial x}\delta x|$.
*In the electronic $m_s = 0$ manifold, ω^0_{mw} and ω^0_{rf} do not enter Eq. (B.9), while $\omega^{\pm 1}_{\mathrm{mw}}$ and $\omega^{\pm 1}_{\mathrm{rf}}$ contribute. The error is estimated by combining contributions from the $m_s = \pm 1$ manifolds, $D_{\omega,0} = \sqrt{D^2_{\omega,+1} + D^2_{\omega,-1}}$.

Appendix C

Decoherence Mechanism of Nuclear Spins: Experimental Methods and Analysis

C.1 Experimental Methods

C.1.1 Differential Measurement of Nuclear Spin Coherence

In our experiments we do not have a direct measurement of the nuclear spin qubit, which would reveal its coherence time. A common strategy to overcome this limitation is to initialize the NV and apply a CNOT gate, flipping the NV state conditional on the nuclear spin state. This effectively maps the state information from the nuclear to the electronic spin. In the nuclear Ramsey experiment in Sec. 3.2.2, we create the entangled state $\alpha|0,+1\rangle + \beta|-1,0\rangle$ with this protocol. The NV is then optically read out, giving the same probability distribution $|\alpha|^2, |\beta|^2$ as if directly measuring the nuclear spin. However, when we measure the nuclear spin coherence, the NV undergoes T_1^e flips, potentially introducing errors in this readout process. First, if the NV final state is different from the nominal one, the second RF pulse operates in the incorrect NV manifold and is thus off-resonance, failing to transfer the nuclear coherence into state populations. Second, the mapping between nuclear and electronic

spin states might fail as the NV state is not fully polarized anymore.

To account for these errors, we perform a differential readout to obtain T_2^{*n}: the first measurement is the regular nuclear Ramsey experiment, measured by applying a CNOT on the NV, subject to possible readout failure; for the second measurement, we add a π phase shift on the second RF $\pi/2$ pulse in the nuclear Ramsey sequence, and then apply the same readout. The difference of the two measurements yields the expected T_2^{*n} decay, as shown in Fig. C-1a. The intuitive explanation is that since one jump of the strong fluctuator totally decoheres the qubit, any nuclear spin coherence is preserved only when the NV stays in the original state. No coherence is left when the final state is different. Therefore, measurements (including unsuccessful ones) already contain all the information about the nuclear spin coherence. The purpose of the differential readout is to remove the two errors mentioned above, which are not related to the nuclear spin coherence decay. Therefore, one could even choose a different measurement as the second data set, as long as it contains the same common mode error. One such choice is to apply a CNOT gate conditional on the nuclear spin being in the $|m_I = 0\rangle$ state (instead of $|m_I = +1\rangle$). We chose to apply a π phase shift on the nuclear Ramsey because when taking the difference of the two measurements this also doubles the signal amplitude. When the qubit is protected against RTN by the DD control, this differential measurement is no longer effective because some nuclear spin coherence is stored in all NV manifolds (Fig. C-1b). We emphasize that this is not a fundamental limit. Single-shot readout, either using on-resonant laser at cryogenic temperature [175] or using intermediate-high magnetic field at room-temperature [156] solves this issue and has been experimentally demonstrated.

C.1.2 Data Analysis for Engineered T_1^e

In the engineered T_1^e experiment, we consider $N_T = 200$ predetermined traces. Each trace is repeated 4×10^4 times in order to build enough statistics to determine the final population state of the NV. In Fig. C-2a, we plot the average signal at t= 16μs for each one of the 200 T_1^e traces, clearly showing that the final state of each trace can be reliably determined to be either $|0\rangle$ or $|-1\rangle$. As another demonstration, in Fig. C-

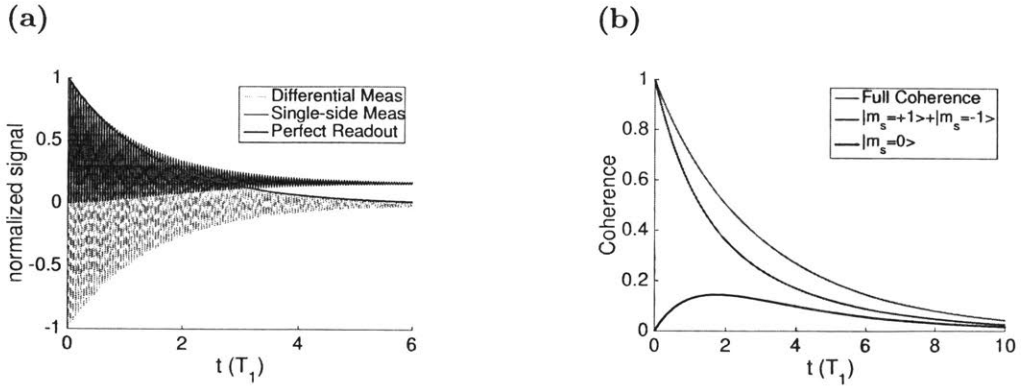

Figure C-1: (a) Simulation of differential measurement for T_2^{*n}. Red solid line assumes perfect readout of the nuclear spin coherence. Black solid line is one set of the differential data. The asymmetric shape and non-zero asymptotic value indicate the presence of a common mode signal not related to nuclear coherence. Gray dashed line shows differential measurement, revealing T_2^{*n}. (b) Nuclear coherence stored in different NV manifolds when we apply DQ DD. Gray solid line is the full coherence. Red solid line is the coherence stored in $|m_s = \pm 1\rangle$ and black solid line in $|m_s\rangle = 0$. As coherence is stored in all manifolds, the differential measurement is no longer effective in removing common mode noise from the NV T_1^e process.

2b we plot out the #47 engineered T_1^e trace in black solid line, and the experimental result in red diamonds. The error bars in all engineered T_1^e experiments are then the standard deviation resulting from the $200 \times 4 \times 10^4$ acquired data for each time point, divided by $\sqrt{N_T}$, which corresponds to the usual standard error of the mean used for the other experimental results.

C.1.3 Engineered T_1^e with DD

In order to simulate a T_1^e flip, we apply a π pulse, the same pulse used for DD. As the pulse length (44ns) is comparable to the smallest time interval between pulses of the DD sequence (200ns), there is a non-negligible probability that a T_1^e flip overlaps with DD pulses for some of the T_1^e traces. We deal with this possibility in two ways: if the overlap of the T_1^e flip and DD π-pulse is larger than half the pulse duration, we do not apply either pulses; also, we discard all traces that contain an overlap of less than half of the pulse duration. We verify that this strategy does not bias the overall engineered noise by measuring T_1^e with and without DD sequence. The results in Fig. C-3a show that the fitted $T_{1\,DD}^e = 10.0 \pm 0.4\mu$s is the same as T_1^e without DD

$(10.0 \pm 0.4\mu s)$ within the errorbars. This verifies that our treatment of overlapping π-pulses does not change the underlying physics, and that the protection of nuclear spin coherence derives from DD, rather than from changes in the engineered T_1^e under DD.

C.1.4 Natural T_1^e with DD

To show that even for the natural T_1^e noise our DD method can efficiently decouple the nuclear spin from its RTN, we measure the natural T_1^e while applying a DD sequence (Fig. C-3b). In order to have a sequence robust against flip angle error and off-resonance pulses, we employ the KDD pulse sequence [197], $\mathrm{KDD}_\varphi = \tau/2 - (\pi)_{\pi/6+\varphi} - \tau - (\pi)_\varphi - \tau - (\pi)_{\pi/2+\varphi} - \tau - (\pi)_\varphi - \tau - (\pi)_{\pi/6+\varphi}$, and concatenate this 5-pulse block following the XY-16 phase cycle [92]: $\mathrm{KDD}_x - \mathrm{KDD}_y - \mathrm{KDD}_x - \mathrm{KDD}_y - \mathrm{KDD}_y - \mathrm{KDD}_x - \mathrm{KDD}_y - \mathrm{KDD}_x - \mathrm{KDD}_{\bar{x}} - \mathrm{KDD}_{\bar{y}} - \mathrm{KDD}_{\bar{x}} - \mathrm{KDD}_{\bar{y}} - \mathrm{KDD}_{\bar{y}} - \mathrm{KDD}_{\bar{x}} - \mathrm{KDD}_{\bar{y}} - \mathrm{KDD}_{\bar{x}}$. We measure up to 8ms, corresponding to 4×10^4 pulses, longer than T_2^{*n}. We fit the data to an exponential decay and find the $1/e$ time to be 3.7 ± 1.3ms, matching $T_1^e = 4.3 \pm 0.3$ms. At this τ, we expect more than a factor of 3 gain in T_2^n, therefore there should be a net improvement in nuclear spin coherence. This suggests that for up to about $\sim 10^5$ pulses, pulse errors in the DD do not accumulate so significantly to counteract potential gains in T_2^n. We expect our method to protect ^{14}N beyond the limit set by natural T_1^e of a few ms, as it could be verified with single-shot readout of the nuclear spin coherence.

C.1.5 Discussion on the relation between T_1^e and T_2^{*n}

Given the large uncertainty in the measured natural $T_1^e = 4.3(3)$ms and $T_2^{*n} = 5.6(1.7)$ms (errors are 95% confidence interval from fit), we find a T_2^{*n}/T_1^e ratio of $5.6/4.3 = 1.3(2)$, which is compatible with the 3LF model prediction ($T_2^{*n}/T_1^e = 1.5$), but does not exclude other models. It is then worth to examine more in depth whether the data does indeed support the three-level spin-fluctuator model or whether other models could be a better match.

Table C.1: Comparing different models for T_2^{*n}/T_1^e

	MSE	T_1^e(ms)	$\sigma_{T_1^e}$(ms)	T_2^{*n}/T_1^e
model 1	0.0083	4.1	0.8	3/2
model 2	0.0091	3.6	0.8	2
model 3	0.0086	5.0	1.0	1
model 4	0.0084	4.3	1.2	1.3(5)

Instead of extracting T_1^e and T_2^{*n} independently from the fit, we fit the two experimental datasets together to four models: 1) fixing $T_2^{*n}/T_1^e = 1.5$; 2) fixing $T_2^{*n}/T_1^e = 2$; 3) fixing $T_2^{*n}/T_1^e = 1$; 4) leaving T_2^{*n}/T_1^e as a free fitting parameter. We compare the mean square error (MSE) of the fit and the uncertainty of the fitted T_1^e for the four models; results are summarized in Table. C.1. This analysis reveals that the model assuming $T_2^{*n}/T_1^e = 1.5$ (model 1) yields the best result both in terms of smallest MSE and smallest uncertainty in T_1^e. A more general fit (model 4) converges to $T_2^{*n}/T_1^e = 1.3(5)$, similar to the result when the two datasets are fitted independently, but results in larger uncertainty in T_1^e. We therefore argue that the experimental data, although with a relatively large uncertainty, are consistent with the spin-fluctuator model predictions.

We further note that we can ascribe the slightly smaller T_2^{*n} than expected ($T_2^{*n}/T_1^e < 1.5$) to environmental drift. Each data point in Fig. 3-2b is averaged over $100,000$ repetitions. We observe $\sim$ 20Hz drift in the nuclear Larmor frequency even after recalibrating the experiment about every hour by measuring the magnetic field drift with the NV and compensating its effect on the nuclear Larmor frequency by adding a corresponding phase shift to the second $\pi/2$ pulse of the nuclear Ramsey sequence. Although small, the frequency drift is non-negligible compared to the detuning in the nuclear Ramsey experiment ($\sim$ 800Hz). The resulting off-resonance pulses cause the average data to have a reduced contrast at long time, which is interpreted as a shorter T_2^{*n}.

C.2 Coherence decay for random telegraph noise

C.2.1 Master Equation Description of the Nuclear Coherence

While the random walker model provides an intuitive semiclassical picture of the decay process, one could also solve the coupled fluctuator-qubit dynamics with a fully quantum mechanical framework. In particular, as the T_1^e process of the NV center is purely Markovian, it is valid to describe the combined electron-nuclear spin dynamics using a master equation. We can then write a Lindblad master equation

$$\frac{d\rho}{dt} = \mathcal{L}[\rho] = -i[\mathcal{H}_i, \rho] + \sum_{k=1}^{M}(L_k\rho(t)L_k^\dagger - \frac{1}{2}L_k^\dagger L_k\rho(t) - \frac{1}{2}\rho(t)L_k^\dagger L_k), \tag{C.1}$$

where the jump operators L_k describe the T_1^e flips of NV, and are therefore $L_k = \Gamma\,|m_s\rangle\langle m_s'|$, where $m_s, m_s' = \{-1, 0, +1\}$. $\Gamma = 1/\sqrt{2T_1^e}$ ($1/\sqrt{3T_1^e}$) for 2LF (3LF). We note that we do not need to explicitly write jump operators for the nuclear spin, as its decoherence is mediated by the Hamiltonian $\mathcal{H}_2 = \omega_e S_z + \omega_n I_z + S\cdot\mathcal{A}\cdot I$ ($\mathcal{H}_3 = DS_z^2 + \omega_e S_z + \omega_n I_z + S\cdot\mathcal{A}\cdot I$) for the electron-nuclear spin register for an electronic spin-1/2 (spin-1). The evolved density operator can be simply found by vectorizing this equation to obtain $\rho(t) = e^{\mathcal{L}t}\rho(0)$. We find that the numerical results from the spin-fluctuator model and the master equation match, indicating the validity of using the semiclassical spin-fluctuator model to describe a fully quantum process. We note that the quantum mechanical treatment could handle more general cases, such as the initial NV state being a superposition state [223].

C.2.2 Analytical results for the coherence time due to a 2LF

In the 2LF case, we can obtain an intuitive picture of the dynamics under DD by diagonalizing the block $[e^{M_{-1}\tau/2}\cdot U_\pi \cdot e^{M_{-1}\tau/2}] = V^{-1}\Lambda_{dd}V$. The diagonal elements of Λ_{dd} are real:

$$\lambda^{\pm} = \frac{e^{-\gamma\tau}}{W}[\gamma\sin(W\tau) \pm \sqrt{v^2 - \gamma^2\cos^2(W\tau)}\,], \tag{C.2}$$

with $W = \sqrt{v^2 - \gamma^2}$. They satisfy $\lambda^+ \geq 0 \geq \lambda^-$, with the equal sign only for $v = \gamma$. As we do not expect a net growth of coherence, the negative eigenvalue λ^- is not expected to contribute. As we will see soon, its coefficient is almost 0. For an initial state $\vec{P} = [1; p]$, $p \in [-1, 1]$, we can express the coherence explicitly:

$$\begin{aligned} \langle e^{i\varphi}(N\tau)\rangle =& \{V\Lambda_{dd}^n V^{-1}\vec{P}\}_1 \\ =& pc_1\lambda_+^n - pc_2\lambda_-^n + c_3\lambda_+^n + c_4\lambda_-^n \end{aligned} \tag{C.3}$$

with c_n as follows

$$\begin{aligned} c_1 =& c_2 = iv\gamma \sin^2(W\tau/2)B, \\ c_3 =& \frac{1}{2} + \frac{B}{2}[v^2 - \gamma^2\cos(W\tau)], \\ c_4 =& \frac{1}{2} - \frac{B}{2}[v^2 - \gamma^2\cos(W\tau)], \end{aligned} \tag{C.4}$$

where $B = 1/[W\sqrt{v^2 - \gamma^2\cos^2(W\tau)}]$. In the strong fluctuator regime, $v \gg \gamma$, we have $c_1, c_2 \sim \gamma/v \approx 0$, $c_3 \approx 1$, $c_4 \approx 0$, yielding an exponential decay $\langle e^{i\varphi}(N\tau)\rangle \approx \lambda_+^n$. Note that Equations (C.2-C.4) are valid even in the weak fluctuator regime.

C.2.3 Analytical results for the coherence time due to a 3LF

The 3-level fluctuator case is more complicated, and we cannot derive an elegant analytical form. When we apply the DQ drive, the coherence approximately follows a simple form

$$\langle e^{i\varphi}(n\tau)\rangle \approx c_+\lambda_+^n + c_0\lambda_0^n + c_-\lambda_-^n, \tag{C.5}$$

where $\{\lambda_+, \lambda_0, \lambda_-\}$ are the eigenvalues of $e^{M_{-1}\tau/2} \cdot U_\pi \cdot e^{M_{-1}\tau/2}$. Instead of writing down their cumbersome expressions, to obtain some intuition in Fig. C-4 we plot how the eigenvalues and their corresponding coefficients change as a function of τ. Similar to the 2LF case, there is one eigenvalue, λ_0, that is negative but has a vanishing contribution to the dynamics. The coherence behavior also depends on the initial state (which sets c_k). Assuming T_1^e= 4ms and starting from the subspace spanned by $|m_s = \pm 1\rangle$, we obtain the solid lines in Fig. C-4; the dashed lines represent the

case of starting from $|m_s = 0\rangle$. Interestingly, in the latter case, the coefficients will go beyond 1 and below 0, causing better coherence for some τ value than the best decay rate of the three eigenvalues.

C.2.4 Weak fluctuator regime for 3-level system

For completeness, we discuss briefly the 3-level weak fluctuator regime, $v \ll \gamma$ (results for the 2LF can be found in reference [22]). When evaluating the decay without DD (to obtain the dephasing time T_2^{*n}) only one of the three eigenvalues of M_{-1} contributes significantly to the decay. Therefore the decoherence has an exponential form, with

$$\begin{aligned} \frac{1}{T_2^*} =& 2\gamma - \frac{3\gamma^2 - v^2}{3^{1/3}K} - \frac{K}{3^{2/3}} \\ K =& \left(9\gamma^3 + \sqrt{3}v\sqrt{v^4 - 9v^2\gamma^2 + 27\gamma^4}\right)^{1/3} \end{aligned} \tag{C.6}$$

The relationship between T_2^{*n} and v is shown in Fig. C-5, covering the full range from weak fluctuator to strong fluctuator. The black circles are the approximated result from the expression in Eq. C.6, which ignores small contributions from the other two eigenvalues. We note that this approximation captures the average behavior for any v, even if the exact result (red curve obtained from numerical calculations) shows additional features. Unlike in the strong fluctuator regime, where $T_2^{*n} = 1.5T_1^e$ is independent of v, T_2^{*n} for a weaker fluctuator is longer in the regime where $v < \gamma$ and increases with γ/v. We also see that both in the weak and strong fluctuator regimes, an exponential decay is a good approximation, but the behavior is more complicated in the intermediate regime.

When we apply DD to protect the nuclear spin qubit in the weak fluctuator regime, we find that only one eigenvalue mainly contributes to the decay, while we had two eigenvalues contributing in the strong coupling regime. The decoherence process is thus exponential. Interestingly, the main contribution comes from the slowest decay term. In Fig. C-6, we show example of the decay component (we did not plot the other two fast decaying components because they are many orders larger) and their contributions to the total decay under DQ drive, similar to Fig. C-4. Here we take

T_1^e= 10μs, $v = 0.01\gamma$. A different result due to initial state as in strong fluctuator regime is not seen here (solid lines overlap with dashed lines). The oscillatory behavior seen in Fig. 3-4a and Fig. C-4a is also missing for the weak fluctuator.

C.2.5 T_2^{*n} in the strong fluctuator regime

In the strong fluctuator regime, T_2^{*n} becomes independent of v (the fluctuator/qubit coupling). This had been observed in Ref. [22] for the TLF. For the 3LF, we can find a similar result by taking the limit of $v \gg \gamma$ in Eq. C.6,

$$\begin{aligned} \lim_{v \gg \gamma} \frac{1}{T_2^*} &= 2\gamma = \frac{2}{3T_1^e} \\ T_2^{*n} &= \frac{3}{2} T_1^e \quad \text{(3LF)} \end{aligned} \tag{C.7}$$

Similarly, for 2LF, the two eigenvalues of M_{-1} are $\gamma \pm \sqrt{\gamma^2 - v^2}$. In the strong fluctuator regime, the only real contribution to decay is γ,

$$T_2^{*n} = \frac{1}{\gamma} = 2T_1^e \quad \text{(2LF)}. \tag{C.8}$$

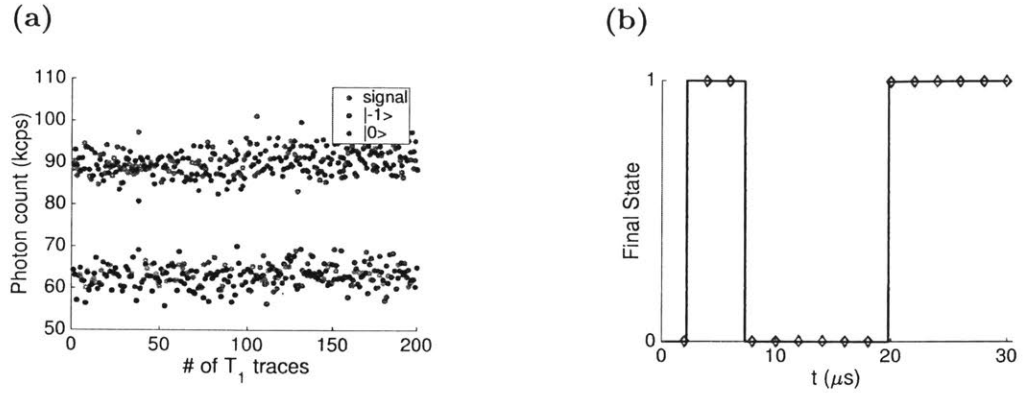

Figure C-2: Engineered T_1^e measurement. (a) We compare the measured NV fluorescence at a fixed time, t= 16μs, to the "bright" and "dark" reference lines, given by the population states $|0\rangle$, $|-1\rangle$, for all 200 different traces. We clearly see that the final state can be read out with high fidelity. (b) One of the engineered T_1^e trace of theory (black solid line) and experiment (red diamond). Error bars are one SEM.

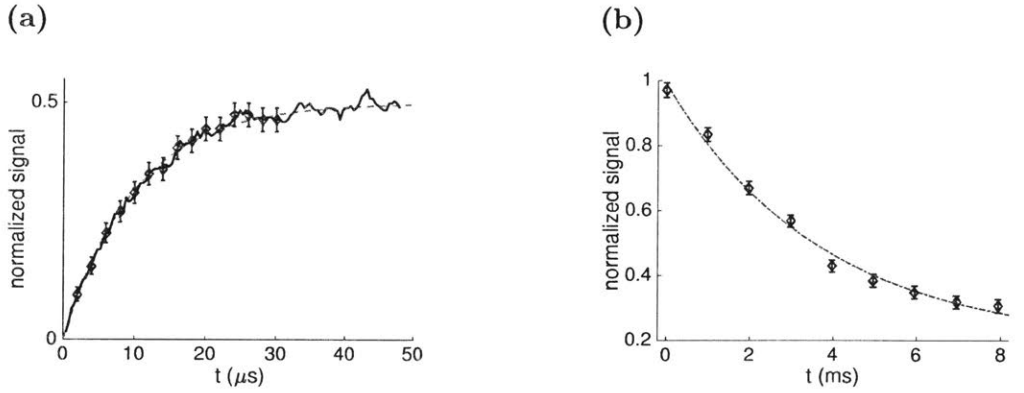

Figure C-3: (a) Same T_1^e experiment as shown in Fig. 3-3b, but with DD sequence. In this experiment, we deal with the overlap of T_1^e flip and DD pulses the same way as to measure T_2^n, demonstrating the same RTN environment when we apply DD sequence and protect ^{14}N . Red diamond: experiment; black solid line: simulation; gray dashed line: fit. (b) natural T_1^e measurement under a DD sequence with $\tau = 200$ns interval (red diamond). The fit to an exponential decay (gray dashed line) gives 3.7 ± 1.3ms in good agreement with the T_1^e measured in the absence of DD pulses. All error bars are one SEM.

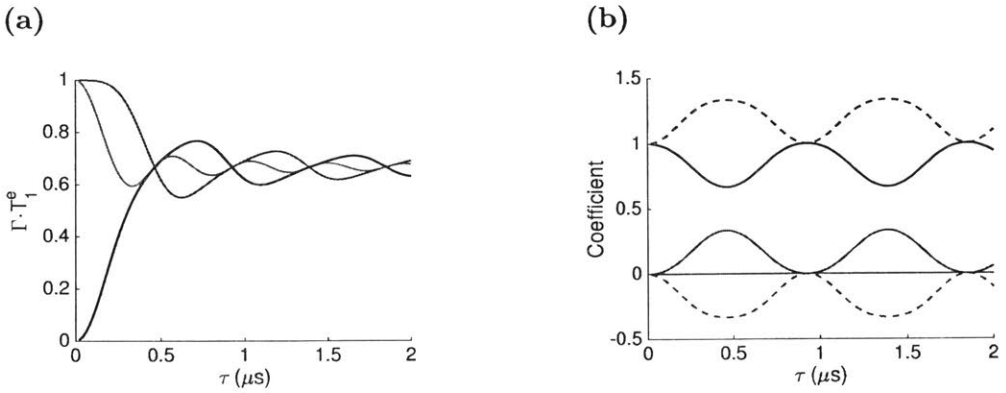

Figure C-4: Contribution of three eigenvalues to the T_2^n decay due to a 3LF. (a) Decay rate corresponding to each eigenvalue as a function of the DD interval τ. Note the gray curve represents the negative eigenvalue, and here we plot its absolute value. (b) Contribution of each eigenvalue to the qubit coherence. We see the negative eigenvalue has almost zero contribution. Solid lines: NV starts in the subspace spanned by $|m_s = \pm 1\rangle$; Dashed lines: NV starts in $|m_s = 0\rangle$.

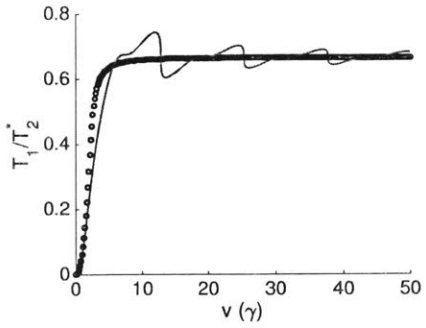

Figure C-5: T_2^{*n} from weak to strong fluctuator regimes as a funcion of v/γ. In the weak fluctuator regime, T_2^{*n} increases as the fluctuator interacts more weakly with the qubit.

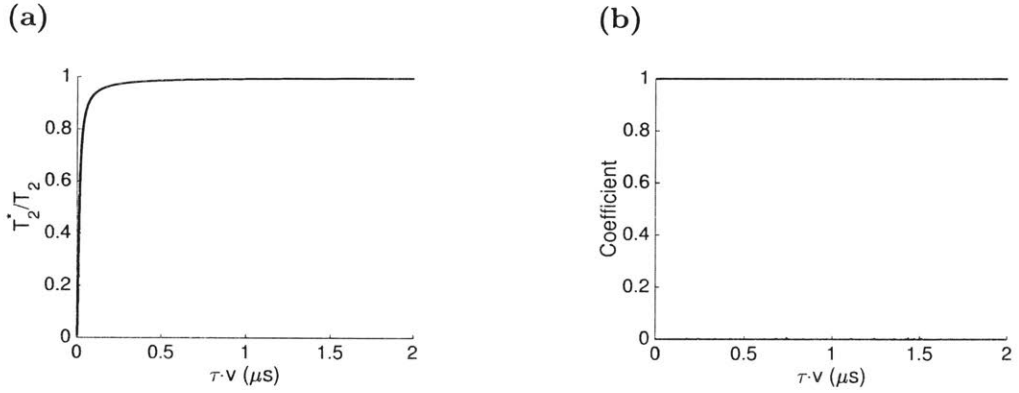

Figure C-6: Contribution of different eigenvalues in the T_2^n decay with a 3-level RTN, for weak fluctuator. (a): decay rate corresponding to the slowest decaying eigenvalue as a function of the DD interval τ. (b): Contribution of each eigenvalue to the qubit coherence. We see that only the black line corresponding to slowest decay has nonzero contribution. Solid lines: NV start in subspace spanned by $|m_s = \pm 1\rangle$; Dashed lines (superimposed): NV starts in $|m_s = 0\rangle$.

Appendix D

Hardware-Efficient QEC: Experimental Methods

D.1 Magnetic Field Stability

We use Neodymium permanent magnet of grade N52, which has a temperature coefficient of $\sim -0.6\%/\mathrm{K}$ from ambient temperature. It is therefore critical to stabilize the temperature. We used two layers of 2-inch insulation materials ($R = 10$ for each layer) to block the windows of the lab. The optical table is enclosed in blackout curtains, in addition to the black hardboard panels enclosing the setup, which both prevents ambient light and heat transfer via convection. Inside the enclosure of the setup, we have a home-made PID temperature control system, with a heating power of 40 W. We observe a typical temperature fluctuation of ± 0.15 K over a few days by a thermostat. In Fig. D-1, we show the observed fluctuation in NV energy splitting between $|0\rangle \leftrightarrow |+1\rangle$ in 292 experiments over 208 hours. The typical fluctuation is within 100 kHz, correspondign to ± 0.04 G in magnetic field.

D.2 Precise Calibration of ω_L

With the magnetic field fluctuation estimated to be ~ 0.04 G, we should be able to determine the Larmor frequency $\omega_L = \gamma_C B$ with an uncertainty of 43 Hz. In

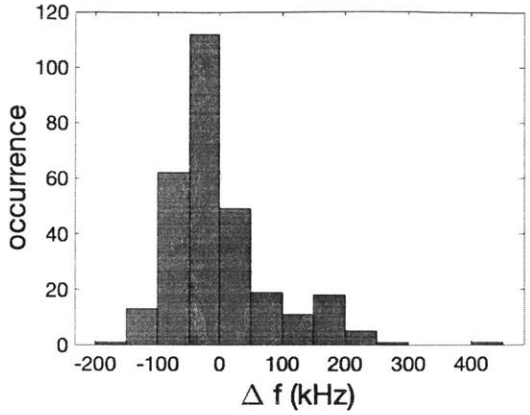

Figure D-1: NV energy fluctuation over 208 hours.

experiment, we achieved this by performing nuclear Ramsey experiment, which reveals the frequency difference $\omega_1 - \omega_L$, where ω_1 is the RF frequency we use to drive the ^{13}C . This gives us 524831 ± 67 Hz (Fig. D-2).

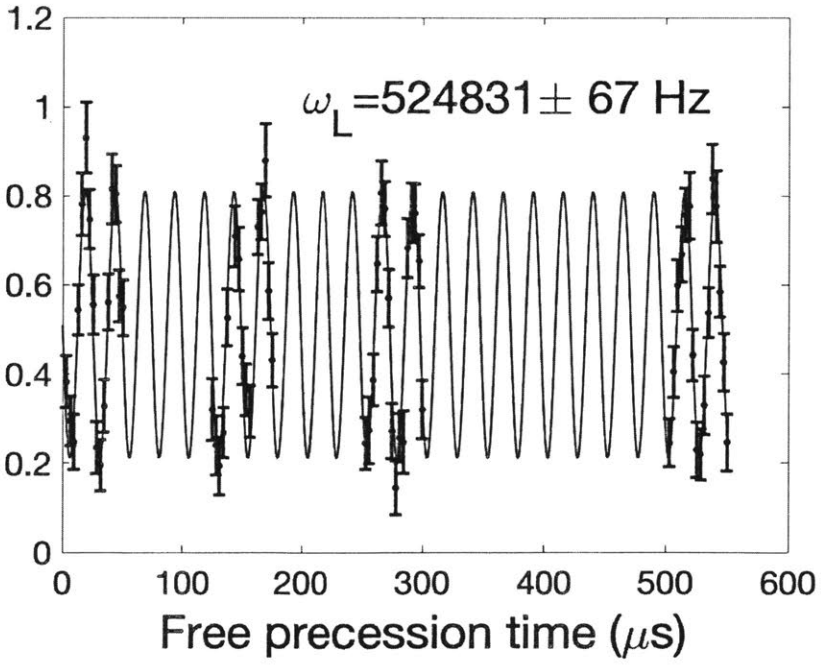

Figure D-2: NV energy fluctuation over 208 hours.

D.3 Simulation of ^{13}C distribution

As discussed in Section. 4.5, our hardware-efficient QEC code corrects pure dephasing induced by a common fluctuator. This in turn restricts our selection of ^{13}C in the quantum register to have small $A_\perp$ hyperfine coupling strength. At first sight, this might seem demanding, due to the probabilistic occurence of ^{13}C . Here we show with simulation that in fact such ^{13}C s are very common.

We start by constructing the diamond lattice, which is face-centered-cubic (FCC) with basis unit consisting of two carbon atoms at $(0,0,0), (\frac{1}{4},\frac{1}{4},\frac{1}{4})$ respectively. Take the natural abundance of 1.1%, we randomly assign sites to be ^{13}C s, indicated by red circles in Fig D-3(a).

Assuming there is only point magnetic dipole-dipole interaction between NV electron and the ^{13}C s

$$H = -\frac{\mu_0 \gamma_e \gamma_C \hbar^2}{4\pi |\vec{r}|^3}\Big(3(\vec{S}\cdot\hat{r})(\vec{I}\cdot\hat{r}) - \vec{S}\cdot\vec{I}\Big), \tag{D.1}$$

we can estimate the hyperfine coupling strength for each ^{13}C . Note that by convention, we take the NV-^{13}C basis such that $A_{zy} = 0$ in the Hamiltonian. Therefore, the $A_\perp$ term is in fact $\sqrt{A_{zx}^2 + A_{zy}^2}$.

We ran through 500 randomly generated ^{13}C distributions around one NV electron, and observed 6211 ^{13}C s whose $A_\parallel = A_{zz} >= 20$ kHz, which can be selectively addressed and individually controlled. 63.8% of all the NVs possess at least two ^{13}C s dominated by pure dephasing error induced by NV fluctuation. Requirements for our hardware-efficient QEC is therefore easily satisfied. The distribution of the hyperfine coupling strength is shown in Fig. D-3(b, c).

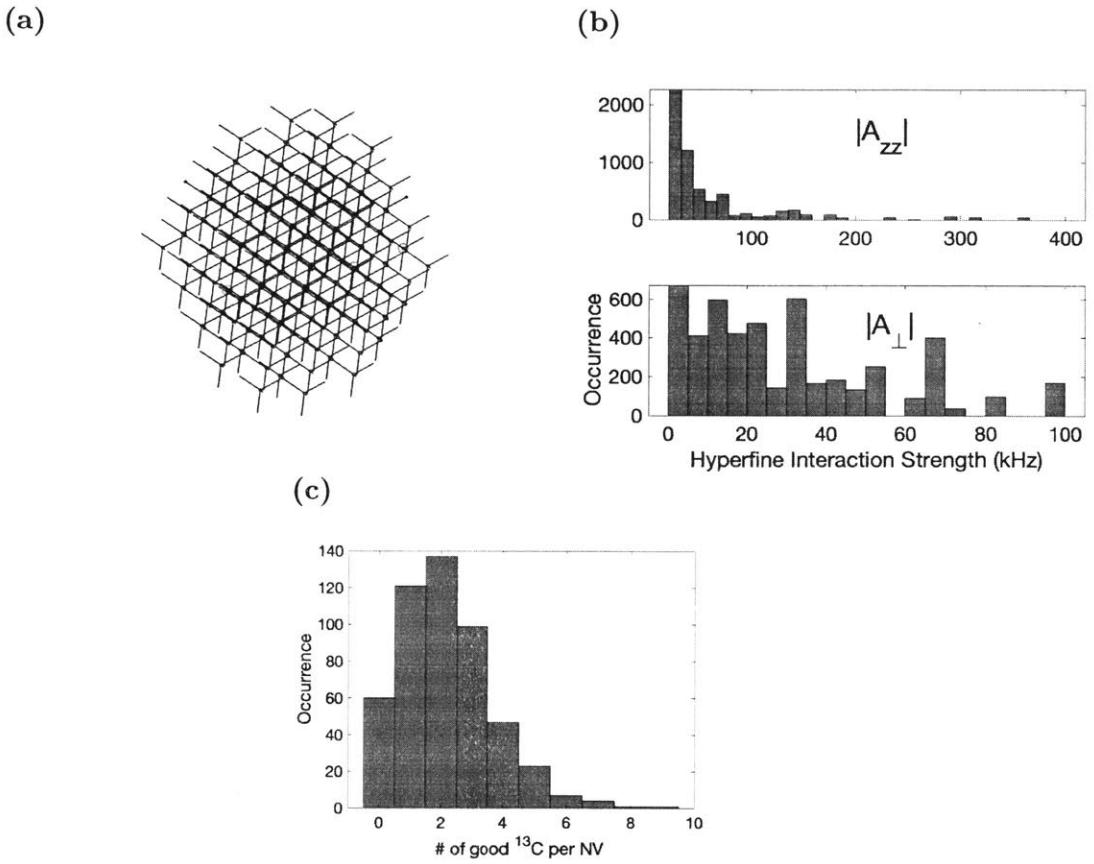

Figure D-3: (a) Diamond lattice. The red circles are randomly assigned ^{13}C . NV is in the middle. (b) Distribution of the strength of the secular $A_{\|}, A_{\perp}$ coupling terms. We selected only addressable and controllable ^{13}C s with $A_{\|} > 20$ kHz. (c) Distribution of the number of ^{13}C s suitable for hardware-efficient QEC per NV. All the distributions are drawn from 500 randomly generated diamond lattice illustrated in (a), with a natural ^{13}C abundance of 1.1%.

Bibliography

[1] See Supplemental Material at [URL will be inserted later], which includes Ref. [73], for stability analyses of various model imperfections, and for further details regarding numerics.

[2] Such coupling induces an effective $\sigma_+\sigma_- + \sigma_-\sigma_+$ interaction between qubits, which could be suppressed through dynamical decoupling or through large detunings between qubits. See J. Majer, J. Chow, J. Gambetta, J. Koch, B. Johnson, J. Schreier, L. Frunzio, D. Schuster, A. Houck, A. Wallraff et al. Nature **449**, 443 (2007).

[3] M. H. Abobeih, J. Randall, C. E. Bradley, H. P. Bartling, M. A. Bakker, M. J. Degen, M. Markham, D. J. Twitchen, and T. H. Taminiau. Atomic-scale imaging of a 27-nuclear-spin cluster using a single-spin quantum sensor, 2019.

[4] Mohamed H. Abobeih, Julia Cramer, Michiel A. Bakker, Norbert Kalb, Daniel J. Twitchen, Matthew Markham, and Tim H. Taminiau. One-second coherence for a single electron spin coupled to a multi-qubit nuclear-spin environment. *Nat. Commun.*, 9,:2552, January 2018.

[5] A Abragam and B. Bleaney. *Electron Paramagnetic Resonance of Transition Ions.* Clarendon Press, Oxford, 1970.

[6] Igor Aharonovich, Andrew D Greentree, and Steven Prawer. Diamond photonics. *Nature Photonics*, 5:397–405, 2011.

[7] Clarice D. Aiello and Paola Cappellaro. Time-optimal control by a quantum actuator. *Phys. Rev. A*, 91:042340, Apr 2015.

[8] Clarice D. Aiello, Masashi Hirose, and Paola Cappellaro. Composite-pulse magnetometry with a solid-state quantum sensor. *Nat. Commun.*, 4:1419–, Jan 2013.

[9] Ashok Ajoy and Paola Cappellaro. Stable three-axis nuclear-spin gyroscope in diamond. *Phys. Rev. A*, 86:062104, Dec 2012.

[10] Ashok Ajoy, Yi-Xiang Liu, Kasturi Saha, Luca Marseglia, Jean-Christophe Jaskula, Ulf Bissbort, and Paola Cappellaro. Quantum interpolation for high-resolution sensing. *Proc. Nat. Acad. Sc.*, 114(9):2149–2153, 2017.

[11] Ashok Ajoy, Ben Safvati, Raffi Nazaryan, J. T. Oon, Ben Han, Priyanka Raghavan, Ruhee Nirodi, Alessandra Aguilar, Kristina Liu, Xiao Cai, Xudong Lv, Emanuel Druga, Chandrasekhar Ramanathan, Jeffrey A. Reimer, Carlos A. Meriles, Dieter Suter, and Alexander Pines. Hyperpolarized relaxometry based nuclear t1 noise spectroscopy in hybrid diamond quantum registers, 2019.

[12] Victor V. Albert, Kyungjoo Noh, Kasper Duivenvoorden, Dylan J. Young, R. T. Brierley, Philip Reinhold, Christophe Vuillot, Linshu Li, Chao Shen, S. M. Girvin, Barbara M. Terhal, and Liang Jiang. Performance and structure of single-mode bosonic codes. *Phys. Rev. A*, 97:032346, Mar 2018.

[13] G. Arrad, Y. Vinkler, D. Aharonov, and A. Retzker. Increasing sensing resolution with error correction. *Phys. Rev. Lett.*, 112:150801, Apr 2014.

[14] Frank Arute, Kunal Arya, Ryan Babbush, Dave Bacon, Joseph C. Bardin, Rami Barends, Rupak Biswas, Sergio Boixo, Fernando G. S. L. Brandao, David A. Buell, Brian Burkett, Yu Chen, Zijun Chen, Ben Chiaro, Roberto Collins, William Courtney, Andrew Dunsworth, Edward Farhi, Brooks Foxen, Austin Fowler, Craig Gidney, Marissa Giustina, Rob Graff, Keith Guerin, Steve Habegger, Matthew P. Harrigan, Michael J. Hartmann, Alan Ho, Markus Hoffmann, Trent Huang, Travis S. Humble, Sergei V. Isakov, Evan Jeffrey, Zhang Jiang, Dvir Kafri, Kostyantyn Kechedzhi, Julian Kelly, Paul V. Klimov, Sergey Knysh, Alexander Korotkov, Fedor Kostritsa, David Landhuis, Mike Lindmark, Erik Lucero, Dmitry Lyakh, Salvatore MandrÃ?, Jarrod R. McClean, Matthew McEwen, Anthony Megrant, Xiao Mi, Kristel Michielsen, Masoud Mohseni, Josh Mutus, Ofer Naaman, Matthew Neeley, Charles Neill, Murphy Yuezhen Niu, Eric Ostby, Andre Petukhov, John C. Platt, Chris Quintana, Eleanor G. Rieffel, Pedram Roushan, Nicholas C. Rubin, Daniel Sank, Kevin J. Satzinger, Vadim Smelyanskiy, Kevin J. Sung, Matthew D. Trevithick, Amit Vainsencher, Benjamin Villalonga, Theodore White, Z. Jamie Yao, Ping Yeh, Adam Zalcman, Hartmut Neven, and John M. Martinis. Quantum supremacy using a programmable superconducting processor. *Nature*, 574(7779):505–510, 2019.

[15] N Aslam, G Waldherr, P Neumann, F Jelezko, and J Wrachtrup. Photo-induced ionization dynamics of the nitrogen vacancy defect in diamond investigated by single-shot charge state detection. *New J. Phys.*, 15(1):013064, 2013.

[16] Nabeel Aslam, Matthias Pfender, Philipp Neumann, Rolf Reuter, Andrea Zappe, Felipe Fávaro de Oliveira, Andrej Denisenko, Hitoshi Sumiya, Shinobu Onoda, Junichi Isoya, and Jörg Wrachtrup. Nanoscale nuclear magnetic resonance with chemical resolution. *Science*, 357(6346):67–71, 2017.

[17] Waseem S. Bakr, Jonathon I. Gillen, Amy Peng, Simon Folling, and Markus Greiner. A quantum gas microscope for detecting single atoms in a hubbard-regime optical lattice. *Nature*, 462(7269):74–77, 2009.

[18] Masashi Ban. Photon-echo technique for reducing the decoherence of a quantum bit. *Journal of Modern Optics*, 45(11):2315–2325, 1998.

[19] Masashi Ban, Sachiko Kitajima, and Fumiaki Shibata. Dynamical suppression of dephasing for Markov processes. *Phys. Lett. A*, 373(40):3614–3618, sep 2009.

[20] N. Bar-Gill, L.M. Pham, A. Jarmola, D. Budker, and R.L. Walsworth. Solid-state electronic spin coherence time approaching one second. *Nat. Commun.*, 4:1743–, April 2013.

[21] Cédric Bény. Perturbative quantum error correction. *Phys. Rev. Lett.*, 107:080501, Aug 2011.

[22] Joakim Bergli and Lara Faoro. Exact solution for the dynamical decoupling of a qubit with telegraph noise. *Phys. Rev. B*, 75(5), feb 2007.

[23] Adam Bermeister, Daniel Keith, and Dimitrie Culcer. Charge noise, spin-orbit coupling, and dephasing of single-spin qubits. *App. Phys. Lett*, 105(19):192102, 2014.

[24] H. Bernien, B. Hensen, W. Pfaff, G. Koolstra, M. S. Blok, L. Robledo, T. H. Taminiau, M. Markham, D. J. Twitchen, L. Childress, and R. Hanson. Heralded entanglement between solid-state qubits separated by three metres. *Nature*, 497:86 EP –, Apr 2013.

[25] Hannes Bernien, Sylvain Schwartz, Alexander Keesling, Harry Levine, Ahmed Omran, Hannes Pichler, Soonwon Choi, Alexander S. Zibrov, Manuel Endres, Markus Greiner, Vladan Vuletic, and Mikhail D. Lukin. Probing many-body dynamics on a 51-atom quantum simulator. *arXiv:1707.04344*, July 2017.

[26] P. Bertet, I. Chiorescu, G. Burkard, K. Semba, C. J. P. M. Harmans, D. P. DiVincenzo, and J. E. Mooij. Dephasing of a superconducting qubit induced by photon noise. *Phys. Rev. Lett.*, 95:257002, Dec 2005.

[27] P Bertet, I Chiorescu, CJP Harmans, and JE Mooij. Dephasing of a flux-qubit coupled to a harmonic oscillator. *arXiv:0507290*, 2005.

[28] M J Biercuk, A C Doherty, and H Uys. Dynamical decoupling sequence construction as a filter-design problem. *J. of Phys. B*, 44(15):154002, 2011.

[29] Michael J Biercuk, Hermann Uys, Aaron P VanDevender, Nobuyasu Shiga, Wayne M Itano, and John J Bollinger. Optimized dynamical decoupling in a model quantum memory. *Nature*, 458(7241):996–1000, April 2009.

[30] Bleaney. In A.J. Freeman and R.B. Frankel, editors, *Hyperfine interactions*, page 1. Academic Press, 1967.

[31] Robin Blume-Kohout, John King Gamble, Erik Nielsen, Kenneth Rudinger, Jonathan Mizrahi, Kevin Fortier, and Peter Maunz. Demonstration of qubit operations below a rigorous fault tolerance threshold with gate set tomography. *Nature Communications*, 8(1):14485, 2017.

[32] M. Born and R. Oppenheimer. Zur quantentheorie der molekeln. *Annalen der Physik*, 389(20):457–484, 1927.

[33] N. Boulant, M. A. Pravia, E. M. Fortunato, T. F. Havel, and D. G. Cory. Experimental concatenation of quantum error correction with decoupling. *Quantum Information Processing*, 1(1):135–144, Apr 2002.

[34] C. E. Bradley, J. Randall, M. H. Abobeih, R. C. Berrevoets, M. J. Degen, M. A. Bakker, M. Markham, D. J. Twitchen, and T. H. Taminiau. A ten-qubit solid-state spin register with quantum memory up to one minute. *Phys. Rev. X*, 9:031045, Sep 2019.

[35] J. Burnett, L. Faoro, I. Wisby, V. L. Gurtovoi, A. V. Chernykh, G. M. Mikhailov, V. A. Tulin, R. Shaikhaidarov, V. Antonov, P. J. Meeson, A. Ya. Tzalenchuk, and T. Lindstroem. Evidence for interacting two-level systems from the 1/f noise of a superconducting resonator. *Nat. Commun.*, 5:4119–, June 2014.

[36] Mark S. Byrd and Daniel A. Lidar. Comprehensive encoding and decoupling solution to problems of decoherence and design in solid-state quantum computing. *Phys. Rev. Lett.*, 89:047901, Jul 2002.

[37] J-M Cai, B Naydenov, R Pfeiffer, L P McGuinness, K D Jahnke, F Jelezko, M B Plenio, and A Retzker. Robust dynamical decoupling with concatenated continuous driving. *New J. Phys.*, 14(11):113023, 2012.

[38] P. Cappellaro, J. S. Hodges, T. F. Havel, and D. G. Cory. Control of qubits encoded in decoherence-free subspaces. *Las. Phys.*, 17:545–551, 2007.

[39] P. Cappellaro, L. Jiang, J. S. Hodges, and M. D. Lukin. Coherence and control of quantum registers based on electronic spin in a nuclear spin bath. *Phys. Rev. Lett.*, 102(21):210502, 2009.

[40] H. Y. Carr and E. M. Purcell. Effects of diffusion on free precession in nuclear magnetic resonance experiments. *Phys. Rev.*, 94(3):630–638, 1954.

[41] Juan Carrasquilla and Roger G. Melko. Machine learning phases of matter. *Nat. Phys.*, 13:431–, February 2017.

[42] E. A. Chekhovich, M. N. Makhonin, A. I. Tartakovskii, A. Yacoby, H. Bluhm, K. C. Nowack, and L. M. K. Vandersypen. Nuclear spin effects in semiconductor quantum dots. *Nature Mat.*, 12:494–504, 2013.

[43] M. Chen, W. K. C. Sun, K. Saha, J.-C. Jaskula, and P. Cappellaro. Protecting solid-state spins from a strongly coupled environment. *New J. Phys.*, 20(6):063011, June 2018.

[44] Mo Chen, Masashi Hirose, and Paola Cappellaro. Measurement of transverse hyperfine interaction by forbidden transitions. *Phys. Rev. B*, 92:020101, Jul 2015.

[45] Xiang-Dong Chen, Chang-Ling Zou, Fang-Wen Sun, and Guang-Can Guo. Optical manipulation of the charge state of nitrogen-vacancy center in diamond. *App. Phys. Lett*, 103(1):013112, jul 2013.

[46] J. Chiaverini, D. Leibfried, T. Schaetz, M. D. Barrett, R. B. Blakestad, J. Britton, W. M. Itano, J. D. Jost, E. Knill, C. Langer, R. Ozeri, and D. J. Wineland. Realization of quantum error correction. *Nature*, 432(7017):602–605, 2004.

[47] L. Childress, M. V. Gurudev Dutt, J. M. Taylor, A. S. Zibrov, F. Jelezko, J. Wrachtrup, P. R. Hemmer, and M. D. Lukin. Coherent dynamics of coupled electron and nuclear spin qubits in diamond. *Science*, 314(5797):281–285, 2006.

[48] L. Childress, J. M. Taylor, A. S. Sørensen, and M. D. Lukin. Fault-tolerant quantum communication based on solid-state photon emitters. *Phys. Rev. Lett.*, 96:070504, Feb 2006.

[49] Kevin S. Chou, Jacob Z. Blumoff, Christopher S. Wang, Philip C. Reinhold, Christopher J. Axline, Yvonne Y. Gao, L. Frunzio, M. H. Devoret, Liang Jiang, and R. J. Schoelkopf. Deterministic teleportation of a quantum gate between two logical qubits. *Nature*, 561(7723):368–373, 2018.

[50] Isaac L. Chuang, Debbie W. Leung, and Yoshihisa Yamamoto. Bosonic quantum codes for amplitude damping. *Phys. Rev. A*, 56:1114–1125, Aug 1997.

[51] A. A. Clerk and D. Wahyu Utami. Using a qubit to measure photon-number statistics of a driven thermal oscillator. *Phys. Rev. A*, 75:042302, Apr 2007.

[52] R. Cleve, A. Ekert, C. Macchiavello, and M. Mosca. Quantum algorithms revisited. *Proceedings of the Royal Society of London. Series A: Mathematical, Physical and Engineering Sciences*, 454(1969):339–354, 1998.

[53] I. Cohen, T. Unden, F. Jelezko, and A. Retzker. Protecting a nuclear spin from a noisy electron spin in diamond. *ArXiv: 1703.01596*, March 2017.

[54] Alexandre Cooper, Jacob P. Covey, Ivaylo S. Madjarov, Sergey G. Porsev, Marianna S. Safronova, and Manuel Endres. Alkaline-earth atoms in optical tweezers. *Phys. Rev. X*, 8:041055, Dec 2018.

[55] D. G. Cory, M. D. Price, W. Maas, E. Knill, R. Laflamme, W. H. Zurek, T. F. Havel, and S. S. Somaroo. Experimental quantum error correction. *Phys. Rev. Lett.*, 81(10):2152–2155, 1998.

[56] J. Cramer, N. Kalb, M. A. Rol, B. Hensen, M. S. Blok, M. Markham, D. J. Twitchen, R. Hanson, and T. H. Taminiau. Repeated quantum error correction on a continuously encoded qubit by real-time feedback. *Nature Communications*, 7:11526, may 2016.

[57] Andrew W. Cross, Lev S. Bishop, Sarah Sheldon, Paul D. Nation, and Jay M. Gambetta. Validating quantum computers using randomized model circuits. *Phys. Rev. A*, 100:032328, Sep 2019.

[58] K. S. Cujia, J. M. Boss, K. Herb, J. Zopes, and C. L. Degen. Tracking the precession of single nuclear spins by weak measurements. *Nature*, 571(7764):230–233, 2019.

[59] B. D'Anjou and W. A. Coish. Soft decoding of a qubit readout apparatus. *Phys. Rev. Lett.*, 113:230402, Dec 2014.

[60] P. de Fouquieres, S.G. Schirmer, S.J. Glaser, and Ilya Kuprov. Second order gradient ascent pulse engineering. *Journal of Magnetic Resonance*, 212(2):412 – 417, 2011.

[61] S. E. de Graaf, A. A. Adamyan, T. Lindström, D. Erts, S. E. Kubatkin, A. Ya. Tzalenchuk, and A. V. Danilov. Direct identification of dilute surface spins on al_2o_3: Origin of flux noise in quantum circuits. *Phys. Rev. Lett.*, 118:057703, Jan 2017.

[62] G. de Lange, Z. H. Wang, D. Riste, V. V. Dobrovitski, and R. Hanson. Universal dynamical decoupling of a single solid-state spin from a spin bath. *Science*, 330(6000):60–3, October 2010.

[63] C. L. Degen, F. Reinhard, and P. Cappellaro. Quantum sensing. *Rev. Mod. Phys.*, 89:035002, July 2017.

[64] Juan P Dehollain, Juha T Muhonen, Robin Blume-Kohout, Kenneth M Rudinger, John King Gamble, Erik Nielsen, Arne Laucht, Stephanie Simmons, Rachpon Kalra, Andrew S Dzurak, and Andrea Morello. Optimization of a solid-state electron spin qubit using gate set tomography. *New Journal of Physics*, 18(10):103018, oct 2016.

[65] M. H. Devoret and R. J. Schoelkopf. Superconducting circuits for quantum information: An outlook. *Science*, 339(6124):1169–1174, 2013.

[66] Michel H Devoret and Christian Glattli. Single-electron transistors. *Physics World*, 11(9):29–34, sep 1998.

[67] Hossein T. Dinani, Dominic W. Berry, Raul Gonzalez, Jeronimo R. Maze, and Cristian Bonato. Bayesian estimation for quantum sensing in the absence of single-shot detection. *Phys. Rev. B*, 99:125413, Mar 2019.

[68] D. P. DiVincenzo. The physical implementation of quantum computation. *Fortschr. Phys.*, 48:771–793, 2000.

[69] Marcus W. Doherty, Neil B. Manson, Paul Delaney, Fedor Jelezko, Joerg Wrachtrup, and Lloyd C.L. Hollenberg. The nitrogen-vacancy colour centre in diamond. *Physics Reports*, 528(1):1 – 45, 2013.

[70] F. Dolde, H. Fedder, M. W. Doherty, T. Nobauer, F. Rempp, G. Balasubramanian, T. Wolf, F. Reinhard, L. C. L. Hollenberg, F. Jelezko, and J. Wrachtrup. Electric-field sensing using single diamond spins. *Nat. Phys.*, 7(6):459–463, June 2011.

[71] F. Dolde, I. Jakobi, B. Naydenov, N. Zhao, S. Pezzagna, C. Trautmann, J. Meijer, P. Neumann, F. Jelezko, and J. Wrachtrup. Room-temperature entanglement between single defect spins in diamond. *Nat Phys*, 9(3):139–143, March 2013.

[72] Florian Dolde, Ville Bergholm, Ya Wang, Ingmar Jakobi, Boris Naydenov, Sebastien Pezzagna, Jan Meijer, Fedor Jelezko, Philipp Neumann, Thomas Schulte-Herbruggen, Jacob Biamonte, and Joerg Wrachtrup. High-fidelity spin entanglement using optimal control. *Nat Commun*, 5:–, February 2014.

[73] A. Dréau, J.-R. Maze, M. Lesik, J.-F. Roch, and V. Jacques. High-resolution spectroscopy of single nv defects coupled with nearby ^{13}C nuclear spins in diamond. *prb*, 85:134107, 2012.

[74] A. Dréau, P. Spinicelli, J. R. Maze, J.-F. Roch, and V. Jacques. Single-shot readout of multiple nuclear spin qubits in diamond under ambient conditions. *Phys. Rev. Lett.*, 110:060502, Feb 2013.

[75] L.-M. Duan, M. D. Lukin, J. I. Cirac, and P. Zoller. Long-distance quantum communication with atomic ensembles and linear optics. *Nature*, 414:413, 2001.

[76] J. M. Elzerman, R. Hanson, L. H. Willems van Beveren, B. Witkamp, L. M. K. Vandersypen, and L. P. Kouwenhoven. Single-shot read-out of an individual electron spin in a quantum dot. *Nature*, 430(6998):431–435, 2004.

[77] Manuel Endres, Hannes Bernien, Alexander Keesling, Harry Levine, Eric R. Anschuetz, Alexandre Krajenbrink, Crystal Senko, Vladan Vuletic, Markus Greiner, and Mikhail D. Lukin. Atom-by-atom assembly of defect-free one-dimensional cold atom arrays. *Science*, 354(6315):1024–1027, 2016.

[78] Abram L. Falk, Paul V. Klimov, Viktor Ivády, Krisztián Szász, David J. Christle, William F. Koehl, Ádám Gali, and David D. Awschalom. Optical polarization of nuclear spins in silicon carbide. *Phys. Rev. Lett.*, 114:247603, Jun 2015.

[79] S. Felton, A. M. Edmonds, M. E. Newton, P. M. Martineau, D. Fisher, D. J. Twitchen, and J. M. Baker. Hyperfine interaction in the ground state of the negatively charged nitrogen vacancy center in diamond. *Phys. Rev. B*, 79:075203, Feb 2009.

[80] J E Field, editor. *The Properties of Natural and Synthetic Diamond.* Academic Press, London, 1992.

[81] Andrew S. Fletcher, Peter W. Shor, and Moe Z. Win. Optimum quantum error recovery using semidefinite programming. *Phys. Rev. A*, 75:012338, Jan 2007.

[82] G. D. Fuchs, G. Burkard, P. V. Klimov, and D. D. Awschalom. A quantum memory intrinsic to single nitrogen-vacancy centres in diamond. *Nat. Phys.*, 7(10):789–793, 2011.

[83] G. D. Fuchs, V. V. Dobrovitski, D. M. Toyli, F. J. Heremans, and D. D. Awschalom. Gigahertz dynamics of a strongly driven single quantum spin. *Science*, 326(5959):1520–1522, 2009.

[84] Adam Gali. Theory of the neutral nitrogen-vacancy center in diamond and its application to the realization of a qubit. *Phys. Rev. B*, 79:235210, Jun 2009.

[85] Jay Gambetta, Alexandre Blais, D. I. Schuster, A. Wallraff, L. Frunzio, J. Majer, M. H. Devoret, S. M. Girvin, and R. J. Schoelkopf. Qubit-photon interactions in a cavity: Measurement-induced dephasing and number splitting. *Phys. Rev. A*, 74:042318, Oct 2006.

[86] Jun Gao, Lu-Feng Qiao, Zhi-Qiang Jiao, Yue-Chi Ma, Cheng-Qiu Hu, Ruo-Jing Ren, Ai-Lin Yang, Hao Tang, Man-Hong Yung, and Xian-Min Jin. Experimental machine learning of quantum states. *Phys. Rev. Lett.*, 120:240501, Jun 2018.

[87] Yvonne Y. Gao, Brian J. Lester, Kevin S. Chou, Luigi Frunzio, Michel H. Devoret, Liang Jiang, S. M. Girvin, and Robert J. Schoelkopf. Entanglement of bosonic modes through an engineered exchange interaction. *Nature*, 566(7745):509–512, 2019.

[88] Richard E. George, Lucio M. Robledo, Owen J. E. Maroney, Machiel S. Blok, Hannes Bernien, Matthew L. Markham, Daniel J. Twitchen, John J. L. Morton, G. Andrew D. Briggs, and Ronald Hanson. Opening up three quantum boxes causes classically undetectable wavefunction collapse. *Proc. Nat. Acad. Sc.*, 110(10):3777–3781, 2013.

[89] Daniel Gottesman. Stabilizer codes and quantum error correction. *arXiv:9705052*, 1997.

[90] Daniel Gottesman, Alexei Kitaev, and John Preskill. Encoding a qubit in an oscillator. *Phys. Rev. A*, 64:012310, Jun 2001.

[91] A. Gruber, A. Drabenstedt, C. Tietz, L. Fleury, J. Wrachtrup, and C. von Borczyskowski. Scanning confocal optical microscopy and magnetic resonance on single defect centers. *Science*, 276(5321):2012–2014, 1997.

[92] Terry Gullion, David B Baker, and Mark S Conradi. New, compensated Carr-Purcell sequences. *J. Mag. Res.*, 89(3):479 - 484, 1990.

[93] A. Gupta, L. Hacquebard, and L. Childress. Efficient signal processing for time-resolved fluorescence detection of nitrogen-vacancy spins in diamond. *J. Opt. Soc. Am. B*, 33(3):B28–B34, 2016.

[94] Luke Hacquebard and Lilian Childress. Charge-state dynamics during excitation and depletion of the nitrogen-vacancy center in diamond. *Phys. Rev. A*, 97:063408, Jun 2018.

[95] E. L. Hahn. Spin echoes. *Phys. Rev.*, 80(4):580–594, 1950.

[96] R. Hanson, L. H. Willems van Beveren, I. T. Vink, J. M. Elzerman, W. J. M. Naber, F. H. L. Koppens, L. P. Kouwenhoven, and L. M. K. Vandersypen. Single-shot readout of electron spin states in a quantum dot using spin-dependent tunnel rates. *Phys. Rev. Lett.*, 94(19):196802, 2005.

[97] Kevin Hartnett. A new "law" suggests quantum supremacy could happen this year. *Quanta Magazine.*

[98] Birgit J. M. Hausmann, Brendan Shields, Qimin Quan, Patrick Maletinsky, Murray McCutcheon, Jennifer T. Choy, Tom M. Babinec, Alexander Kubanek, Amir Yacoby, Mikhail D. Lukin, and Marko Loncar. Integrated diamond networks for quantum nanophotonics. *Nano Letters*, 12(3):1578–1582, 2012.

[99] Xing-Fei He, Neil B. Manson, and Peter T. H. Fisk. Paramagnetic resonance of photoexcited n-v defects in diamond. ii. hyperfine interaction with the ^{14}n nucleus. *Phys. Rev. B*, 47(14):8816–8822, 1993.

[100] Masashi Hirose. *Quantum Control of Spin Systems in diamond.* PhD thesis, Massachusetts Institute of Technology, 2015.

[101] Masashi Hirose and Paola Cappellaro. Coherent feedback control of a single qubit in diamond. *Nature*, 532(7597):77–80, April 2016.

[102] L. Hu, Y. Ma, W. Cai, X. Mu, Y. Xu, W. Wang, Y. Wu, H. Wang, Y. P. Song, C.-L. Zou, S. M. Girvin, L.-M. Duan, and L. Sun. Quantum error correction and universal gate set operation on a binomial bosonic logical qubit. *Nature Physics*, 15(5):503–508, 2019.

[103] Pu Huang, Xi Kong, Nan Zhao, Fazhan Shi, Pengfei Wang, Xing Rong, Ren-Bao Liu, and Jiangfeng Du. Observation of an anomalous decoherence effect in a quantum bath at room temperature. *Nature Communications*, 2(1):570, 2011.

[104] D. B. Hume, T. Rosenband, and D. J. Wineland. High-fidelity adaptive qubit detection through repetitive quantum nondemolition measurements. *Phys. Rev. Lett.*, 99(12):120502, 2007.

[105] J.H J. H. Shim, B. Nowak, I. Niemeyer, J. Zhang, F. D. Brandao, and D. Suter. Characterization of hyperfine interaction between single electron and single nuclear spins in diamond assisted by quantum beat from the nuclear spin. *arXiv:1307.0257*, 2013.

[106] V. Jacques, P. Neumann, J. Beck, M. Markham, D. Twitchen, J. Meijer, F. Kaiser, G. Balasubramanian, F. Jelezko, and J. Wrachtrup. Dynamic polarization of single nuclear spins by optical pumping of nitrogen-vacancy color centers in diamond at room temperature. *Phys. Rev. Lett.*, 102(5):057403, 2009.

[107] Jean-Christophe Jaskula, Kasturi Saha, Ashok Ajoy, Daniel J. Twitchen, Matthew Markham, and Paola Cappellaro. Cross-sensor feedback stabilization of an emulated quantum spin gyroscope. *Phys. Rev. App.*, 11:054010, August 2019.

[108] Evan Jeffrey, Daniel Sank, J. Y. Mutus, T. C. White, J. Kelly, R. Barends, Y. Chen, Z. Chen, B. Chiaro, A. Dunsworth, A. Megrant, P. J. J. O'Malley, C. Neill, P. Roushan, A. Vainsencher, J. Wenner, A. N. Cleland, and John M. Martinis. Fast accurate state measurement with superconducting qubits. *Phys. Rev. Lett.*, 112:190504, May 2014.

[109] L. Jiang, M. V. Gurudev Dutt, E. Togan, L. Childress, P. Cappellaro, J. M. Taylor, and M. D. Lukin. Coherence of an optically illuminated single nuclear spin qubit. *Phys. Rev. Lett.*, 100(7):073001, 2008.

[110] L. Jiang, J. S. Hodges, J. R. Maze, P. Maurer, J. M. Taylor, D. G. Cory, P. R. Hemmer, R. L. Walsworth, A. Yacoby, A. S. Zibrov, and M. D. Lukin. Repetitive readout of a single electronic spin via quantum logic with nuclear spin ancillae. *Science*, 326(5950):267–272, 2009.

[111] Peter D. Johnson, Jonathan Romero, Jonathan Olson, Yudong Cao, and AlÃąn Aspuru-Guzik. Qvector: an algorithm for device-tailored quantum error correction. *arXiv:1711.02249*, November 2017.

[112] J. Kelly, R. Barends, A. G. Fowler, A. Megrant, E. Jeffrey, T. C. White, D. Sank, J. Y. Mutus, B. Campbell, Yu Chen, Z. Chen, B. Chiaro, A. Dunsworth, I.-C. Hoi, C. Neill, P. J. J. Oâ??Malley, C. Quintana, P. Roushan, A. Vainsencher, J. Wenner, A. N. Cleland, and John M. Martinis. State preservation by repetitive error detection in a superconducting quantum circuit. *Nature*, 519:66 EP –, Mar 2015.

[113] James G. Kempf and Daniel P. Weitekamp. Method for atomic-layer-resolved measurement of polarization fields by nuclear magnetic resonance. *Journal of Vacuum Science & Technology B*, 18(4):2255–2262, 2000.

[114] E. M. Kessler, I. Lovchinsky, A. O. Sushkov, and M. D. Lukin. Quantum error correction for metrology. *Phys. Rev. Lett.*, 112:150802, Apr 2014.

[115] N. Khaneja, T. Reiss, C. Kehlet, T. Schulte-Herbuggen, and S. Glaser. Optimal control of coupled spin dynamics: design of nmr pulse sequences by gradient ascent algorithms. *J. Mag. Res.*, 172:296–305, 2005.

[116] Kaveh Khodjasteh and Lorenza Viola. Dynamically error-corrected gates for universal quantum computation. *Phys. Rev. Lett.*, 102:080501, Feb 2009.

[117] H. J. Kimble. The quantum internet. *Nature*, 453:1023–1030, 2008.

[118] E. Knill, R. Laflamme, R. Martinez, and C. Negrevergne. Benchmarking quantum computers: The five-qubit error correcting code. *Phys. Rev. Lett.*, 86:5811–5814, Jun 2001.

[119] Emanuel Knill and Raymond Laflamme. Theory of quantum error-correcting codes. *Phys. Rev. A*, 55:900–911, Feb 1997.

[120] Robert L. Kosut, Alireza Shabani, and Daniel A. Lidar. Robust quantum error correction via convex optimization. *Phys. Rev. Lett.*, 100:020502, Jan 2008.

[121] Alex Krizhevsky, Ilya Sutskever, and Geoffrey E. Hinton. Imagenet classification with deep convolutional neural networks. *Commun. ACM*, 60(6):84–90, May 2017.

[122] David Layden and Paola Cappellaro. Spatial noise filtering through error correction for quantum sensing. *npj Quantum Information*, 4(1):30, July 2018.

[123] David Layden, Mo Chen, and Paola Cappellaro. Efficient quantum error correction of dephasing induced by a common fluctuator. *arXiv:1903.01046*, March 2019.

[124] David Layden, Sisi Zhou, Paola Cappellaro, and Liang Jiang. Ancilla-free quantum error correction codes for quantum metrology. *Phys. Rev. Lett.*, 122:040502, Jan 2019.

[125] M. P. Ledbetter, K. Jensen, R. Fischer, A. Jarmola, and D. Budker. Gyroscopes based on nitrogen-vacancy centers in diamond. *Phys. Rev. A*, 86(5):052116, November 2012.

[126] Debbie W. Leung, M. A. Nielsen, Isaac L. Chuang, and Yoshihisa Yamamoto. Approximate quantum error correction can lead to better codes. *Phys. Rev. A*, 56:2567–2573, Oct 1997.

[127] Wenqian Lian, Sheng-Tao Wang, Sirui Lu, Yuanyuan Huang, Fei Wang, Xinxing Yuan, Wengang Zhang, Xiaolong Ouyang, Xin Wang, Xianzhi Huang, Li He, Xiuying Chang, Dong-Ling Deng, and Luming Duan. Machine learning topological phases with a solid-state quantum simulator. *Phys. Rev. Lett.*, 122:210503, May 2019.

[128] D.A. Lidar and T.A. Brun. *Quantum Error Correction.* Cambridge University Press, 2013.

[129] Norbert M. Linke, Mauricio Gutierrez, Kevin A. Landsman, Caroline Figgatt, Shantanu Debnath, Kenneth R. Brown, and Christopher Monroe. Fault-tolerant quantum error detection. *Science Advances*, 3(10), 2017.

[130] Gang-Qin Liu, Jian Xing, Wen-Long Ma, Ping Wang, Chang-Hao Li, Hoi Chun Po, Yu-Ran Zhang, Heng Fan, Ren-Bao Liu, and Xin-Yu Pan. Single-shot readout of a nuclear spin weakly coupled to a nitrogen-vacancy center at room temperature. *Phys. Rev. Lett.*, 118:150504, Apr 2017.

[131] Genyue Liu, Mo Chen, Yi-Xiang Liu, David Layden, and Paola Cappellaro. Repetitive readout enhanced by machine learning, 2019.

[132] Seth Lloyd and Lorenza Viola. Engineering quantum dynamics. *Phys. Rev. A*, 65(1):010101, 2001.

[133] I. Lovchinsky, A. O. Sushkov, E. Urbach, N. P. de Leon, S. Choi, K. De Greve, R. Evans, R. Gertner, E. Bersin, C. Müller, L. McGuinness, F. Jelezko, R. L. Walsworth, H. Park, and M. D. Lukin. Nuclear magnetic resonance detection and spectroscopy of single proteins using quantum logic. *Science*, 351(6275):836–841, 2016.

[134] Sirui Lu, Shilin Huang, Keren Li, Jun Li, Jianxin Chen, Dawei Lu, Zhengfeng Ji, Yi Shen, Duanlu Zhou, and Bei Zeng. A separability-entanglement classifier via machine learning. *Phys. Rev. A*, 98:012315, Jul 2018.

[135] Yue-Chi Ma and Man-Hong Yung. Transforming bell's inequalities into state classifiers with machine learning. *npj Quantum Information*, 4(1):34, 2018.

[136] Stefan Machlup. Noise in semiconductors: Spectrum of a twoâĂŘparameter random signal. *Journal of Applied Physics*, 25(3):341–343, 1954.

[137] Easwar Magesan, Jay M. Gambetta, A. D. Córcoles, and Jerry M. Chow. Machine learning for discriminating quantum measurement trajectories and improving readout. *Phys. Rev. Lett.*, 114:200501, May 2015.

[138] J Majer, JM Chow, JM Gambetta, Jens Koch, BR Johnson, JA Schreier, L Frunzio, DI Schuster, AA Houck, Andreas Wallraff, et al. Coupling superconducting qubits via a cavity bus. *Nature*, 449(7161):443, 2007.

[139] H. J. Mamin, M. H. Sherwood, M. Kim, C. T. Rettner, K. Ohno, D. D. Awschalom, and D. Rugar. Multipulse double-quantum magnetometry with near-surface nitrogen-vacancy centers. *Phys. Rev. Lett.*, 113:030803, Jul 2014.

[140] N. B. Manson, J. P. Harrison, and M. J. Sellars. Nitrogen-vacancy center in diamond: Model of the electronic structure and associated dynamics. *Phys. Rev. B*, 74(10):104303, 2006.

[141] L. Marseglia, J. P. Hadden, A. C. Stanley-Clarke, J. P. Harrison, B. Patton, Y-L D. Ho, B. Naydenov, F. Jelezko, J. Meijer, P.R. Dolan, J.M. Smith, J.G. Rarity, and J.L. O'Brien. Nanofabricated solid immersion lenses registered to single emitters in diamond. *App. Phys. Lett*, 98(13):133107–133107–3, 2011.

[142] P. C. Maurer, G. Kucsko, C. Latta, L. Jiang, N. Y. Yao, S. D. Bennett, F. Pastawski, D. Hunger, N. Chisholm, M. Markham, D. J. Twitchen, J. I. Cirac, and M. D. Lukin. Room-temperature quantum bit memory exceeding one second. *Science*, 336(6086):1283–1286, 2012.

[143] David C. McKay, Christopher J. Wood, Sarah Sheldon, Jerry M. Chow, and Jay M. Gambetta. Efficient z gates for quantum computing. *Phys. Rev. A*, 96:022330, Aug 2017.

[144] S. Meiboom and D. Gill. Modified spin-echo method for measuring nuclear relaxation times. *Rev. Sc. Instr.*, 29(8):688–691, 1958.

[145] Alexey A. Melnikov, Leonid E. Fedichkin, and Alexander Alodjants. Detecting quantum speedup by quantum walk with convolutional neural networks, 2019.

[146] Seth T. Merkel, Jay M. Gambetta, John A. Smolin, Stefano Poletto, Antonio D. Córcoles, Blake R. Johnson, Colm A. Ryan, and Matthias Steffen. Self-consistent quantum process tomography. *Phys. Rev. A*, 87:062119, Jun 2013.

[147] Marios H. Michael, Matti Silveri, R. T. Brierley, Victor V. Albert, Juha Salmilehto, Liang Jiang, and S. M. Girvin. New class of quantum error-correcting codes for a bosonic mode. *Phys. Rev. X*, 6:031006, Jul 2016.

[148] Andrea Morello, Jarryd J. Pla, Floris A. Zwanenburg, Kok W. Chan, Kuan Y. Tan, Hans Huebl, Mikko Mottonen, Christopher D. Nugroho, Changyi Yang, Jessica A. van Donkelaar, Andrew D. C. Alves, David N. Jamieson, Christopher C. Escott, Lloyd C. L. Hollenberg, Robert G. Clark, and Andrew S. Dzurak. Single-shot readout of an electron spin in silicon. *Nature*, 467(7316):687–691, 2010.

[149] John J. L. Morton, Alexei M. Tyryshkin, Richard M. Brown, Shyam Shankar, Brendon W. Lovett, Arzhang Ardavan, Thomas Schenkel, Eugene E. Haller, Joel W. Ager, and S. A. Lyon. Solid-state quantum memory using the 31p nuclear spin. *Nature*, 455(7216):1085–1088, 2008.

[150] Osama Moussa, Jonathan Baugh, Colm A. Ryan, and Raymond Laflamme. Demonstration of sufficient control for two rounds of quantum error correction in a solid state ensemble quantum information processor. *Phys. Rev. Lett.*, 107:160501, Oct 2011.

[151] Osama Moussa, Ian Hincks, and David G. Cory. Preparing and preserving the double quantum coherence in nvâĹŠ centers in diamond at low fields. *Journal of Magnetic Resonance*, 249:24 – 31, 2014.

[152] A. H. Myerson, D. J. Szwer, S. C. Webster, D. T. C. Allcock, M. J. Curtis, G. Imreh, J. A. Sherman, D. N. Stacey, A. M. Steane, and D. M. Lucas. High-fidelity readout of trapped-ion qubits. *Phys. Rev. Lett.*, 100:200502, May 2008.

[153] Clemens Neuenhahn, B. Kubala, B. Abel, and Florian Marquardt. Recent progress in open quantum systems: Non-gaussian noise and decoherence in fermionic systems. *physica status solidi (b)*, 246(5):1018–1023, 2009.

[154] P. Neumann, R. Kolesov, V Jacques, J Beck, J Tisler, A Batalov, L Rogers, N B Manson, G Balasubramanian, F Jelezko, and J. Wrachtrup. Excited-state spectroscopy of single nv defects in diamond using optically detected magnetic resonance. *New J. Phys.*, 11(1):013017, 2009.

[155] Philipp Neumann. *Towards a room temperature solid state quantum processor—The nitrogen-vacancy center in diamond.* PhD thesis, University of Stuttgart, 2012.

[156] Philipp Neumann, Johannes Beck, Matthias Steiner, Florian Rempp, Helmut Fedder, Philip R. Hemmer, Jorg Wrachtrup, and Fedor Jelezko. Single-shot readout of a single nuclear spin. *Science*, 5991:542–544, 2010.

[157] M.A. Nielsen and I.L. Chuang. *Quantum Computation and Quantum Information: 10th Anniversary Edition.* Cambridge University Press, Cambridge, UK, 2010.

[158] D. Nigg, M. Müller, E. A. Martinez, P. Schindler, M. Hennrich, T. Monz, M. A. Martin-Delgado, and R. Blatt. Quantum computations on a topologically encoded qubit. *Science*, 345(6194):302–305, 2014.

[159] Kyungjoo Noh, Victor V Albert, and Liang Jiang. Quantum capacity bounds of gaussian thermal loss channels and achievable rates with gottesman-kitaev-preskill codes. *IEEE Transactions on Information Theory*, 2018.

[160] N. Ofek, A. Petrenko, R. Heeres, P. Reinhold, Z. Leghtas, B. Vlastakis, Y. Liu, L. Frunzio, S. M. Girvin, L. Jiang, M. Mirrahimi, M. H. Devoret, and R. J. Schoelkopf. Extending the lifetime of a quantum bit with error correction in superconducting circuits. *Nature*, 536:441–445, August 2016.

[161] E. Paladino, Y. M. Galperin, G. Falci, and B. L. Altshuler. 1/f noise: Implications for solid-state quantum information. *Rev. Mod. Phys.*, 86:361–418, Apr 2014.

[162] Adriano Macarone Palmieri, Egor Kovlakov, Federico Bianchi, Dmitry Yudin, Stanislav Straupe, Jacob Biamonte, and Sergei Kulik. Experimental neural network enhanced quantum tomography, 2019.

[163] Gerardo A Paz-Silva and D A Lidar. Optimally combining dynamical decoupling and quantum error correction. *Scientific Reports*, 3:1530, apr 2013.

[164] Matthias Pfender, Ping Wang, Hitoshi Sumiya, Shinobu Onoda, Wen Yang, Durga Bhaktavatsala Rao Dasari, Philipp Neumann, Xin-Yu Pan, Junichi Isoya, Ren-Bao Liu, and Joerg Wrachtrup. High-resolution spectroscopy of single nuclear spins via sequential weak measurements. *Nat. Commun.*, 10(1):594–, 2019.

[165] F. Poggiali, P. Cappellaro, and N. Fabbri. Measurement of the excited-state transverse hyperfine coupling in nv centers via dynamic nuclear polarization. *Phys. Rev. B*, 95(19):195308, May 2017.

[166] John Preskill. Quantum computing and the entanglement frontier. March 2012.

[167] John Preskill. Quantum Computing in the NISQ era and beyond. *Quantum*, 2:79, August 2018.

[168] K. Rama Koteswara Rao and Dieter Suter. Characterization of hyperfine interaction between an nv electron spin and a first-shell ^{13}C nuclear spin in diamond. *Phys. Rev. B*, 94(6):060101, aug 2016.

[169] Robert Raussendorf, Daniel E. Browne, and Hans J. Briegel. Measurement-based quantum computation on cluster states. *Phys. Rev. A*, 68(2):022312, 2003.

[170] M. D. Reed, L. DiCarlo, S. E. Nigg, L. Sun, L. Frunzio, S. M. Girvin, and R. J. Schoelkopf. Realization of three-qubit quantum error correction with superconducting circuits. *Nature*, 482:382–, February 2012.

[171] M. Reimpell and R. F. Werner. Iterative optimization of quantum error correcting codes. *Phys. Rev. Lett.*, 94:080501, Mar 2005.

[172] Andreas Reiserer, Norbert Kalb, Machiel S. Blok, Koen J. M. van Bemmelen, Tim H. Taminiau, Ronald Hanson, Daniel J. Twitchen, and Matthew Markham. Robust quantum-network memory using decoherence-protected subspaces of nuclear spins. *Phys. Rev. X*, 6:021040, Jun 2016.

[173] Alan Robertson, Christopher Granade, Stephen D. Bartlett, and Steven T. Flammia. Tailored codes for small quantum memories. *Phys. Rev. Applied*, 8:064004, Dec 2017.

[174] Lucio Robledo, Hannes Bernien, Toeno van der Sar, and Ronald Hanson. Spin dynamics in the optical cycle of single nitrogen-vacancy centres in diamond. *New J. Phys.*, 13(2):025013, 2011.

[175] Lucio Robledo, Lilian Childress, Hannes Bernien, Bas Hensen, Paul F. A. Alkemade, and Ronald Hanson. High-fidelity projective read-out of a solid-state spin quantum register. *Nature*, 477(7366):574–578, 2011.

[176] S. Rosenblum, Y. Y. Gao, P. Reinhold, C. Wang, C. J. Axline, L. Frunzio, S. M. Girvin, Liang Jiang, M. Mirrahimi, M. H. Devoret, and R. J. Schoelkopf. A cnot gate between multiphoton qubits encoded in two cavities. *Nature Communications*, 9(1):652, 2018.

[177] S. Rosenblum, P. Reinhold, M. Mirrahimi, Liang Jiang, L. Frunzio, and R. J. Schoelkopf. Fault-tolerant detection of a quantum error. *Science*, 361(6399):266–270, 2018.

[178] S. Sangtawesin, C. A. McLellan, B. A. Myers, A. C. Bleszynski Jayich, D. D. Awschalom, and J. R. Petta. Hyperfine-enhanced gyromagnetic ratio of a nuclear spin in diamond. *New Journal of Physics*, 18(8):083016, August 2016.

[179] S. Sangtawesin and J. R. Petta. Hyperfine-enhanced gyromagnetic ratio of a nuclear spin in diamond. *ArXiv:1503.07464*, 2015.

[180] R. Santagati, A. A. Gentile, S. Knauer, S. Schmitt, S. Paesani, C. Granade, N. Wiebe, C. Osterkamp, L. P. McGuinness, J. Wang, M. G. Thompson, J. G. Rarity, F. Jelezko, and A. Laing. Magnetic-field learning using a single electronic spin in diamond with one-photon readout at room temperature. *Phys. Rev. X*, 9:021019, Apr 2019.

[181] Jochen Scheuer, Xi Kong, Ressa S Said, Jeson Chen, Andrea Kurz, Luca Marseglia, Jiangfeng Du, Philip R Hemmer, Simone Montangero, Tommaso Calarco, Boris Naydenov, and Fedor Jelezko. Precise qubit control beyond the rotating wave approximation. *New J. Phys.*, 16(9):093022, 2014.

[182] Philipp Schindler, Julio T. Barreiro, Thomas Monz, Volckmar Nebendahl, Daniel Nigg, Michael Chwalla, Markus Hennrich, and Rainer Blatt. Experimental repetitive quantum error correction. *Science*, 332(6033):1059–1061, 2011.

[183] PO Schmidt, T. Rosenband, C. Langer, WM Itano, JC Bergquist, and DJ Wineland. Spectroscopy using quantum logic. *Science*, 309(5735):749–752, 2005.

[184] A. P. Sears, A. Petrenko, G. Catelani, L. Sun, Hanhee Paik, G. Kirchmair, L. Frunzio, L. I. Glazman, S. M. Girvin, and R. J. Schoelkopf. Photon shot noise dephasing in the strong-dispersive limit of circuit qed. *Phys. Rev. B*, 86:180504, Nov 2012.

[185] Alireza Seif, Kevin A Landsman, Norbert M Linke, Caroline Figgatt, C Monroe, and Mohammad Hafezi. Machine learning assisted readout of trapped-ion qubits. *J. Phys. B: At., Mol. Opt. Phys.*, 51(17):174006, aug 2018.

[186] Chao Shen, Kyungjoo Noh, Victor V. Albert, Stefan Krastanov, M. H. Devoret, R. J. Schoelkopf, S. M. Girvin, and Liang Jiang. Quantum channel construction with circuit quantum electrodynamics. *Phys. Rev. B*, 95:134501, Apr 2017.

[187] B. J. Shields, Q. P. Unterreithmeier, N. P. de Leon, H. Park, and M. D. Lukin. Efficient readout of a single spin state in diamond via spin-to-charge conversion. *Phys. Rev. Lett.*, 114:136402, Mar 2015.

[188] J. H. Shim, I. Niemeyer, J. Zhang, and D. Suter. Room-temperature high-speed nuclear-spin quantum memory in diamond. *Phys. Rev. A*, 87:012301, Jan 2013.

[189] Chang S. Shin, Mark C. Butler, Hai-Jing Wang, Claudia E. Avalos, Scott J. Seltzer, Ren-Bao Liu, Alexander Pines, and Vikram S. Bajaj. Optically detected nuclear quadrupolar interaction of ^{14}N in nitrogen-vacancy centers in diamond. *Phys. Rev. B*, 89:205202, May 2014.

[190] P. W. Shor. Algorithms for quantum computation: discrete logarithms and factoring. In *Proceedings 35th Annual Symposium on Foundations of Computer Science*, pages 124–134, Nov 1994.

[191] Peter W. Shor. Scheme for reducing decoherence in quantum computer memory. *Phys. Rev. A*, 52:R2493–R2496, Oct 1995.

[192] Peter W. Shor. Fault-tolerant quantum computation. In *37th Annual Symposium on Foundations of Computer Science*, pages 56–65. IEEE Comput. Soc. Press, Los Alamitos, CA, 1996.

[193] Peter W Shor. Polynomial-time algorithms for prime factorization and discrete logarithms on a quantum computer. *Siam J.Sci.Stat.Comp.*, 26:1484, 1997.

[194] R.W. Simmonds, K. M. Lang, D. A. Hite, S. Nam, D. P. Pappas, and John M. Martinis. Decoherence in josephson phase qubits from junction resonators. *Phys. Rev. Lett.*, 93:077003, 2004.

[195] Benjamin Smeltzer, Lilian Childress, and Adam Gali. 13 c hyperfine interactions in the nitrogen-vacancy centre in diamond. *New Journal of Physics*, 13(2):025021, Feb 2011.

[196] Benjamin Smeltzer, Jean McIntyre, and Lilian Childress. Robust control of individual nuclear spins in diamond. *Phys. Rev. A*, 80:050302, Nov 2009.

[197] Alexandre M. Souza, Gonzalo A. Álvarez, and Dieter Suter. Robust dynamical decoupling for quantum computing and quantum memory. *Phys. Rev. Lett.*, 106:240501, Jun 2011.

[198] Alexandre M. Souza, Gonzalo A. Álvarez, and Dieter Suter. Experimental protection of quantum gates against decoherence and control errors. *Phys. Rev. A*, 86:050301, Nov 2012.

[199] A. Steane. Multiple-particle interference and quantum error correction. *Royal Society of London Proceedings Series A*, 452:2551–2577, 1996.

[200] A. M. Steane. Error correcting codes in quantum theory. *Phys. Rev. Lett.*, 77:793, 1996.

[201] M. Steiner, P. Neumann, J. Beck, F. Jelezko, and J. Wrachtrup. Universal enhancement of the optical readout fidelity of single electron spins at nitrogen-vacancy centers in diamond. *Phys. Rev. B*, 81(3):035205, 2010.

[202] Soraya Taghavi, Robert L Kosut, and Daniel A Lidar. Channel-optimized quantum error correction. *IEEE Transactions on Information Theory*, 56(3):1461–1473, 2010.

[203] H.T. Taminiau, J. Cramer, T. van der Sar, V.V. Dobrovitski, and R. Hanson. Universal control and error correction in multi-qubit spin registers in diamond. *Nat Nano*, 9(3):171–176, March 2014.

[204] T. H. Taminiau, J. J. T. Wagenaar, T. van der Sar, F. Jelezko, V. V. Dobrovitski, and R. Hanson. Detection and control of individual nuclear spins using a weakly coupled electron spin. *Phys. Rev. Lett.*, 109(13):137602, September 2012.

[205] J. M. Taylor, P. Cappellaro, L. Childress, L. Jiang, D. Budker, P. R. Hemmer, A. Yacoby, R. Walsworth, and M. D. Lukin. High-sensitivity diamond magnetometer with nanoscale resolution. *Nat. Phys.*, 4(10):810–816, 2008.

[206] Barbara M. Terhal. Quantum error correction for quantum memories. *Rev. Mod. Phys.*, 87:307–346, Apr 2015.

[207] J-P Tetienne, L Rondin, P Spinicelli, M Chipaux, T Debuisschert, J-F Roch, and V Jacques. Magnetic-field-dependent photodynamics of single nv defects in diamond: an application to qualitative all-optical magnetic imaging. *New J. Phys.*, 14(10):103033, 2012.

[208] Giacomo Torlai, Guglielmo Mazzola, Juan Carrasquilla, Matthias Troyer, Roger Melko, and Giuseppe Carleo. Neural-network quantum state tomography. *Nat. Phys.*, 14(5):447–450, 2018.

[209] Giacomo Torlai, Brian Timar, Evert P. L. van Nieuwenburg, Harry Levine, Ahmed Omran, Alexander Keesling, Hannes Bernien, Markus Greiner, Vladan Vuletic, Mikhail D. Lukin, Roger G. Melko, and Manuel Endres. Integrating neural networks with a quantum simulator for state reconstruction, 2019.

[210] David M. Toyli, Charles F. de las Casas, David J. Christle, Viatcheslav V. Dobrovitski, and David D. Awschalom. Fluorescence thermometry enhanced by the quantum coherence of single spins in diamond. *Proc. Nat. Acad. Sc.*, 110(21):8417–8421, 2013.

[211] T van der Sar, ZH Wang, MS Blok, H Bernien, TH Taminiau, DM Toyli, DA Lidar, DD Awschalom, R Hanson, and VV Dobrovitski. Decoherence-protected

quantum gates for a hybrid solid-state spin register. *Nature*, 484(7392):82–86, 2012.

[212] Evert P.L. van Nieuwenburg, Ye-Hua Liu, and Sebastian Huber. Learning phase transitions by confusion. *Nat. Phys.*, 13:435–439, Feb 2017.

[213] L. Viola and S. Lloyd. Dynamical suppression of decoherence in two-state quantum systems. *Phys. Rev. A*, 58:2733, 1998.

[214] Lorenza Viola, Emanuel Knill, and Seth Lloyd. Dynamical decoupling of open quantum systems. *Phys. Rev. Lett.*, 82(12):2417–2421, 1999.

[215] G. Waldherr, P. Neumann, S. F. Huelga, F. Jelezko, and J. Wrachtrup. Violation of a temporal bell inequality for single spins in a diamond defect center. *Phys. Rev. Lett.*, 107:090401, 2011.

[216] G. Waldherr, Y. Wang, S. Zaiser, M. Jamali, T. Schulte-Herbruggen, H. Abe, T. Ohshima, J. Isoya, J. F. Du, P. Neumann, and J. Wrachtrup. Quantum error correction in a solid-state hybrid spin register. *Nature*, 506(7487):204–207, February 2014.

[217] Noel H. Wan, Brendan J. Shields, Donggyu Kim, Sara Mouradian, Benjamin Lienhard, Michael Walsh, Hassaram Bakhru, Tim Schroeder, and Dirk Englund. Efficient extraction of light from a nitrogen-vacancy center in a diamond parabolic reflector. *Nano Lett.*, 18(5):2787–2793, May 2018.

[218] F. Wang, Y.-Y. Huang, Z.-Y. Zhang, C. Zu, P.-Y. Hou, X.-X. Yuan, W.-B. Wang, W.-G. Zhang, L. He, X.-Y. Chang, and L.-M. Duan. Room-temperature storage of quantum entanglement using decoherence-free subspace in a solid-state spin system. *Phys. Rev. B*, 96:134314, Oct 2017.

[219] Z. Wang, S. Shankar, Z.K. Minev, P. Campagne-Ibarcq, A. Narla, and M.H. Devoret. Cavity attenuators for superconducting qubits. *Phys. Rev. Applied*, 11:014031, Jan 2019.

[220] Matthias Widmann, Sang-Yun Lee, Torsten Rendler, Nguyen Tien Son, Helmut Fedder, Seoyoung Paik, Li-Ping Yang, Nan Zhao, Sen Yang, Ian Booker, Andrej Denisenko, Mohammad Jamali, S Ali Momenzadeh, Ilja Gerhardt, Takeshi Ohshima, Adam Gali, Erik Janzén, and Jörg Wrachtrup. Coherent control of single spins in silicon carbide at room temperature. *Nature Mat.*, 14:164–168, 2015.

[221] Wikipedia contributors. Moore's law — Wikipedia, the free encyclopedia, 2019. [Online; accessed 10-October-2019].

[222] Wikipedia contributors. Robert j. schoelkopf — Wikipedia, the free encyclopedia, 2019. [Online; accessed 10-October-2019].

[223] Henry J. Wold, Håkon Brox, Yuri M. Galperin, and Joakim Bergli. Decoherence of a qubit due to either a quantum fluctuator, or classical telegraph noise. *Phys. Rev. B*, 86:205404, Nov 2012.

[224] Gary Wolfowicz, Matias Urdampilleta, Mike L.W. Thewalt, Helge Riemann, Nikolai V. Abrosimov, Peter Becker, Hans-Joachim Pohl, and John J.L. Morton. Conditional control of donor nuclear spins in silicon using stark shifts. *Phys. Rev. Lett.*, 113:157601, Oct 2014.

[225] J. Wrachtrup, S. Kilin, and A. Nizovtsev. Quantum computation using the 13c nuclear spins near the single nv defect center in diamond. *Optics and Spectroscopy*, 91(3):429–437, 2001.

[226] Fei Yan, Dan Campbell, Philip Krantz, Morten Kjaergaard, David Kim, Jonilyn L. Yoder, David Hover, Adam Sears, Andrew J. Kerman, Terry P. Orlando, Simon Gustavsson, and William D. Oliver. Distinguishing coherent and thermal photon noise in a circuit quantum electrodynamical system. *Phys. Rev. Lett.*, 120:260504, Jun 2018.

[227] Fei Yan, Simon Gustavsson, Archana Kamal, Jeffrey Birenbaum, Adam P Sears, David Hover, Ted J Gudmundsen, Danna Rosenberg, Gabriel Samach, Steven Weber, et al. The flux qubit revisited to enhance coherence and reproducibility. *Nature communications*, 7:12964, 2016.

[228] Jen-Hao Yeh, Jay LeFebvre, Shavindra Premaratne, F. C. Wellstood, and B. S. Palmer. Microwave attenuators for use with quantum devices below 100 mk. *Journal of Applied Physics*, 121(22):224501, 2017.

[229] Sebastian Zaiser, Torsten Rendler, Ingmar Jakobi, Thomas Wolf, Sang-Yun Lee, Samuel Wagner, Ville Bergholm, Thomas Schulte-Herbruggen, Philipp Neumann, and Jorg Wrachtrup. Enhancing quantum sensing sensitivity by a quantum memory. *Nat. Commun.*, 7:–, August 2016.

[230] Jingfu Zhang, Alexandre M. Souza, Frederico Dias Brandao, and Dieter Suter. Protected quantum computing: Interleaving gate operations with dynamical decoupling sequences. *Phys. Rev. Lett.*, 112:050502, Feb 2014.

[231] Nan Zhao, Zhen-Yu Wang, and Ren-Bao Liu. Anomalous decoherence effect in a quantum bath. *Phys. Rev. Lett.*, 106:217205, May 2011.

[232] J. Zopes, K. Sasaki, K. S. Cujia, J. M. Boss, K. Chang, T. F. Segawa, K. M. Itoh, and C. L. Degen. High-resolution quantum sensing with shaped control pulses. *Phys. Rev. Lett.*, 119:260501, Dec 2017.

[233] Floris A. Zwanenburg, Andrew S. Dzurak, Andrea Morello, Michelle Y. Simmons, Lloyd C. L. Hollenberg, Gerhard Klimeck, Sven Rogge, Susan N. Coppersmith, and Mark A. Eriksson. Silicon quantum electronics. *Rev. Mod. Phys.*, 85:961–1019, Jul 2013.